2014

EMULSION-TEMPLATED SILICON/CARBON ANODES WITH REDUCED GRAPHENE OXIDE

Patrick Stellfeld
University of Rhode Island, pstellfeld@my.uri.edu

EMULSION-TEMPLATED SILICON/CARBON ANODES WITH REDUCED GRAPHENE OXIDE

BY

PATRICK STELLFELD

A THESIS SUBMITTED IN PARTIAL FULFILLMENT OF THE REQUIREMENTS FOR THE DEGREE OF

MASTER OF SCIENCE

IN

CHEMICAL ENGINEERING

UNIVERSITY OF RHODE ISLAND

2014

MASTER OF SCIENCE

OF

PATRICK STELLFELD

APPROVED:

Thesis Committee:

Major Professor Arijit Bose

Brett Lucht

Richard Brown

Sigrid Berka

DEAN OF THE GRADUATE SCHOOL

UNIVERSITY OF RHODE ISLAND

2014

ABSTRACT

Silicon is an attractive material for anodes in energy storage devices[1], [2], because it has ten times the theoretical capacity of its state-of-the-art carbonaceous counterpart. Silicon anodes can be used both in traditional lithium-ion batteries and in more recent Li–O_2 and Li–S batteries as a replacement for the dendrite-forming lithium metal anodes. The main challenges associated with silicon anodes are structural degradation and instability of the solid-electrolyte interphase caused by the large volume change (~300%) during cycling, the occurrence of side reactions with the electrolyte, and the low volumetric capacity when the material size is reduced to a nanometre scale [3], [4].

The simple fabrication technique of emulsion-templated direct assembly, which was reported by Chen et al. (2014) [5] is further developed, by using reduced Graphene Oxide (r-GO) to increase the conductivity and increase the silicon-carbon ratio (Si/C ratio). In this method, Si nanoparticles are confined in the oil phase of an oil-in-water emulsion stabilized by carbon black (CB). These CB nanoparticles are both oil- and water-wettable. The hydrophilic/hydrophobic balance for the CB nanoparticles also causes them to form a network in the continuous aqueous phase. Upon drying this emulsion on a current collector, the CB particles located at the surfaces of the emulsion droplets form mesoporous cages that loosely encapsulate the Si particles that were in the oil. The CB particles that were in the aqueous phase form a conducting network connected to the CB cages. The space within the cages allows for Si particle expansion without transmitting stresses to the surrounding carbon network. Half-cell experiments using this Si/CB anode architecture show a specific

capacity of ~1000 mAh/g Si + C and a Coulombic efficiency of 99.5% after 50 cycles. This corresponds to a increase to the previous work of over 30%. Emulsion-templating is a simple, inexpensive processing strategy that directs Si and conducts CB particles to desired spatial locations for superior performance of anodes in lithium ion batteries.

ACKNOWLEDGMENTS

I cannot express enough thanks to my committee for their continued support and encouragement: Dr. Arijit Bose, my committee chair; Dr. Richard Brown; Dr. Brett Lucht; and Dr. Sigrid Berka. I offer my sincere appreciation for the learning opportunities provided by my committee.

My completion of this project could not have been accomplished without the support of my research group, Ian Calise; Hari Katepalli; Yanjing Chen; Indrani Chakraborty; Yuzi Zhang and Amitesh Saha. I am very grateful to Mengyun Nie, postdoc in the Chemical Department of the University of Rhode Island for assembling and testing my batteries.

To my family and friends – thank you for supporting me with this experience in the United States. Special thanks to my girlfriend Inga Schön for always believing in me and her encouragement.

TABLE OF CONTENTS

LIST OF TABLES

LIST OF FIGURES

CHAPTER 1 INTRODUCTION

1.1 Motivation

Still representing the highest performing secondary battery systems [1], [6], [7], the lithium-ion batteries (Li-ion batteries), based on the intercalation concept proposed by M. Whittingham [8] in the ’70s, nowadays play an essential role in modern technologies, being in particular the best battery technology now available for vehicles. In portable electronics and mobile communication devices they are already commonly used and with the growing market in electrical mobility they are now entering the markets of hybrid and electrical vehicles. Many other “green” technologies, such as the solar cells, benefit from the possibility to produce less expensive batteries with extremely reduced sizes and long cycle life. Expectations of convenience and long-living portable power urged to develop technological strategies that resulted in a net improvement of the batteries performances. These advances can be better appreciated if one considers that in the last decade the energy density has been improved two times. But obviously, a great breakthrough is needed in order to increase the energy density from the current 210 Wh kg^{-1} of Li-ion batteries to the ambitious target of 500–700 Wh kg^{-1} to satisfy application in electrical vehicles before 2030 [9]. The energy density per unit area is a critical figure of merit for power modules, whereas for other applications, such as electrical vehicles, the density per unit weight is the key parameter. To reach high energy density the anode materials must combine high specific storage capacity and Coulombic efficiency. [10], [11]

Although the good performances of the graphite materials in terms of electronic conductivity, low electrochemical potential and Coulombic efficiency

(>95%), the low specific lithiation capacity (372mAhg^{-1}) [12] limit the possibility to force up the efficiency and to meet the ever increasing requirements of our society. In order to enhance the performances of such batteries, in the place of graphite several different anode materials with higher specific capacity of lithium (Li) accommodation are thinkable. Without any doubt, the most promising element is silicon (Si), characterized by a high theoretical specific capacity that is an order of magnitude beyond that offered by conventional graphite anodes [4], [13]. In this work, a method for the production of silicon/carbon (Si/C) anodes is treated and improved.

1.2 Thesis outline

This study has two main objectives; the increase of the Si/C ratio in an anode produced by emulsion-templated direct assembly and the introduction of reduced graphene oxide (r-GO). Previous work of my research group by Chen et al. (2014) [5] has shown, that it is possible to prepare high capacity, stable Si/C Anodes for Li-ion batteries using this method. This study is about improving this approach.

A porous anode Si/C alloy material was formed using CB particles to stabilize a Pickering emulsion which is then simply dried on a current collector. The anode material was physically characterized using light microscopy (LM), field emission and cryo-scanning electron microscopy (FE-SEM and cryo-SEM), transmission electron microscopy (TEM) and energy-dispersive x-ray spectroscopy (EDS). Furthermore the assembled batteries were electrically tested as half cells to determine capacity and cycle stability. The batteries were tested under conditions designed to evaluate different aspects of their performance.

In order to provide the reader with the necessary knowledge base to utilize the content of this thesis, a review of current status of the research and development of Si anodes will be given first. Due to the broad spectrum of the main topics, this review is rather extensive, and contains two main parts; the Li-ion battery in general and the Si anode. This is followed by the theory necessary to understand the experimental work which is illustrated briefly.

The experimental section gives an account of the experiments performed during the course of this work. It includes a detailed description of the fabrication and characterization of the emulsion templated Si alloys, the electronically testing

performed and the post-cycling characterization. After this section, the results are presented. These results are then discussed in relation to the previously presented theory, and possible weaknesses of the experimental procedure are evaluated, before conclusions are drawn.

CHAPTER 2 PRINCIPLES

2.1 The Li-Ion Battery

The Li-ion battery has become an important part of energy storage technology, as one of the most effective and energy dense secondary battery chemistries, being used in various applications and scales, classicaly portable electronic devices and are now extended to applications such as power tools and electric vehicles. Emerging from research based on the Li metal primary battery, the current Li-ion battery was proposed in a patent filed in May 1985 by Akira Yoshino and a working prototype was assembled the following year [14]. A comparison of the specific power and energy of different battery technologies can be seen in Figure 2-1, showing the very good performance of two of the most common lithium-ion technologies. The difference between these lies in the use of different cathode materials, a topic that will be described in detail later.

This section will first introduce the field of Li-ion batteries, beginning with a brief explanation of the working principle of the lithium-ion battery. An overview of important characteristics of batteries will then provide, an explanation and definition of some expressions that are used later in the thesis. An important aspect of the Li-ion battery, especially with regard to anode materials; the solid electrolyte interface (SEI), will then be explained. In addition, a review of materials used for other components and purposes in Li-ion battery is also deemed while the research performed in this study mainly concerns the Si anode.

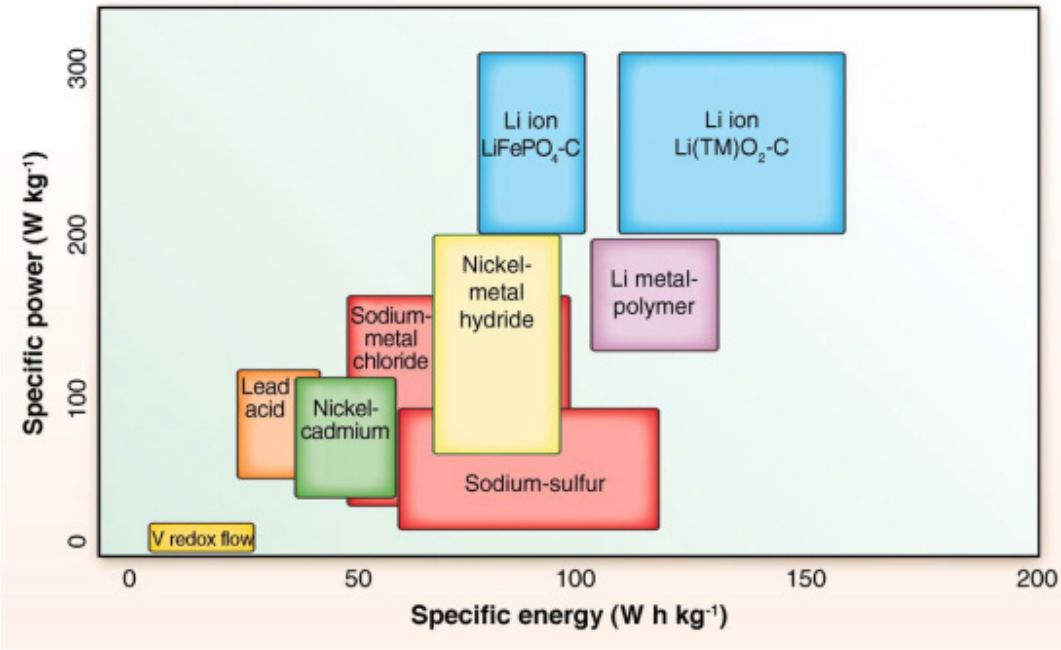

Figure 2-1. A comparison of the specific power and energy capacity of different battery technologies, showing the superior performance of different lithium-ion technologies [15].

2.1.1 Working Principle

Secondary battery systems in their simplest form consist of two electrodes immersed in an ionically conducting electrolyte and electronically connected through an external circuit. The structure of the Li-ion battery does not differ notably from this. Through a redox reaction the battery converts chemical energy to electrical energy during discharge. The reduction and oxidation reactions happen on different electrodes, and as these are separated by a non-electronically conducting electrolyte, the electrons are forced through the external circuit, where a load can be applied. During charging, by driving this redox reaction in the opposite direction chemical energy gets generated from electrical energy. The cathode and anode are by definition the electrodes where the reduction and oxidation reactions happen, respectively, and which electrode is which therefore changes depending on whether the battery is

charged or discharged. In battery science the convention is to designate the electrodes by their function during discharge. [16]

In addition to the many similarities between the Li-ion battery and other battery chemistries, there are some important differences. The most obvious being the use of lithium ions, which is one of the most reductive elements. The Li/Li + couple has a reduction potential of -3.04 volts vs. the standard hydrogen electrode [17]. Combined with a low atomic weight of only 6.94 u [18], Li meta is ideal for energy storage, yielding both a high number of electrons per mass and high energy per electron. Ideally, to obtain the highest possible capacity, the anode should be pure lithium, as is the case for the lithium metal primary battery. However, there are obvious problems when attempting to charge a Li metal battery. Not only is the high chemical reactivity of metallic lithium afflicted with inherent risk, one also encountered issues with Li being deposited on the anode in the form of sharp dendrites able to pierce the separator and cause a short circuit. These problems are severely reducing the reliability of the batteries, and also exhibit a risk for thermal runaway reactions. In cases where lithium is involved these can pose a serious safety hazard because of being most violent [14].

This was the motivation behind the research that led to the Li-ion battery, which solves these problems by using so called intercalation electrodes as both anode and cathode, meaning that Li ions can be reversibly inserted and extracted from the electrodes, rather than deposited on their surfaces. A spontaneously movement from the anode to the cathode is caused by a potential-difference between the electrodes causing Li ions to through the electrolyte. As the electrolyte is electronically isolating,

the electrons are left to travel through the external cycle, where their electrical energy can be used.

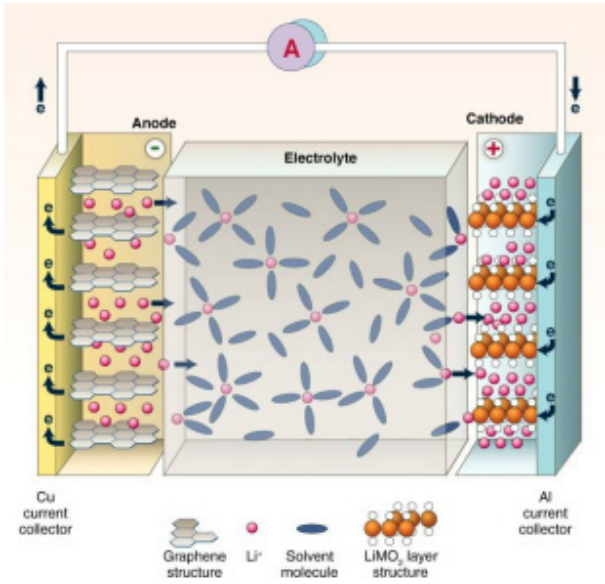

Figure 2-2. Schematic of a lithium-ion battery. In this case, graphitic carbon is used as an anode and a relevant transition metal oxide as cathode. On charging, Li ions are removed or deintercalated from the layered oxide compound and intercalated into the graphite layers. The process is reversed on discharge. [15]

An applied voltage forces the electrons and Li ions to move in the opposite direction, during charging. A Li-ion battery is represented in Figure 2-2. This battery is using a common combination of intercalation electrodes; a graphite anode and a layered transition metal oxide cathode. The schematic structures for the charged and discharged anode and cathode can be seen in Figure 2-3, along with the half-cell reactions and full cell reaction for this example. The factor x in these reactions vary depending on which transition metal oxide is used, but is usually between 0.5 and 1. At open circuit conditions the electrons are hindered from moving, establishing an electric field nullifying the potential difference between the electrodes and halting the reaction by the transport of ions. As soon as the external circuit is closed, the reaction is free to continue and hence, energy can be released.

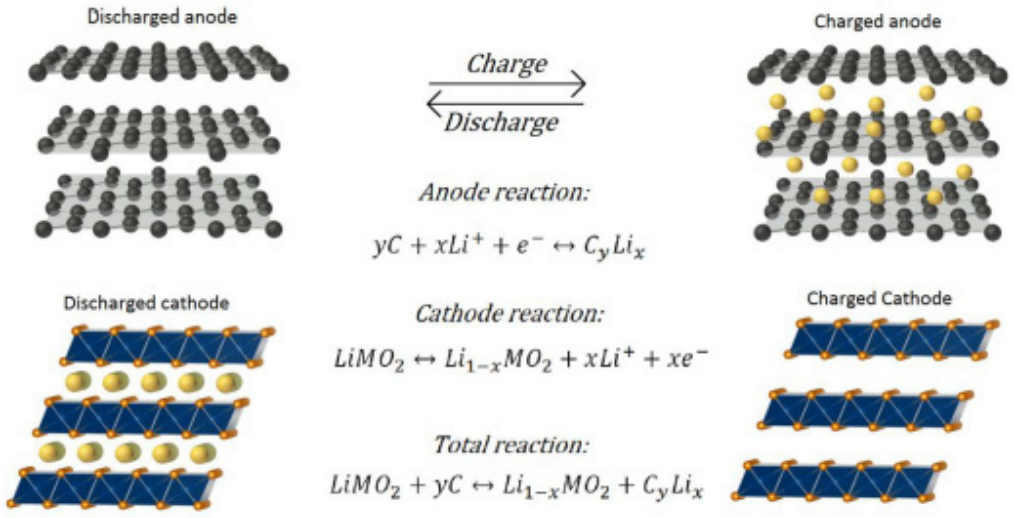

Figure 2-3. Schematic presentation of the charged and discharged structure of a graphite anode and a layered oxide. [19]

2.1.2 Important Characteristics

- *Specific capacity* is the capacity of the whole cell or the electrode capacity relative to its weight and is given in mAh/g. The relationship between the capacity of the entire cell and the capacities of its components is commonly expressed

$$\mathrm{C_{Cell}} = \frac{1}{\frac{1}{\mathrm{C_A}} + \frac{1}{\mathrm{C_C}} + \frac{1}{\mathrm{Q_M}}} \qquad (2.1\text{-}1)$$

  Where C_A is the anode capacity, C_C is the cathode capacity and $1/Q_M$ is the capacity specific mass of the remaining cell components; electrolyte, casing etc.

- *Charge density* is the capacity of the whole cell or the electrode capacity, but relative to volume rather than weight, and is usually given in mAh/cm^3 .

- *Capacity retention* is a measure of how well the battery copes with being charged and discharged. It is representing the cycle stability of a cell, and is represented by a certain percentage of its initial capacity.
- *C-rate* is a normalized charge/discharge rate that depends on the electrode or battery capacity. It is defined as the rate at which the entire capacity of the electrode is charged or discharged in one hour. Charge/discharge rate during cycling is usually given as a fraction or multiple of the C-rate. E.g. for a 4 gram electrode with specific capacity of 1000mAh/g the C-rate is 4000mA, and if cycled at for instance C/8 the current is set to 500mA.
- *Coulombic efficiency* is defined as the ratio between the amount of charge that can be extracted from the battery and the amount of charge that was put in during charging, typically given in percent.
- *Charge and discharge* in battery science, are defined as a forced or spontaneous reaction respectively in the battery. For an anode in a full cell, this means that Li intercalation would be denoted charging. However, when coupled with Li metal counter electrodes in half cells, anode materials will in fact act as cathode, hence lithiation would constitute discharging. To prevent ambiguity, in this work, lithiation of anode materials will always be denoted charging and delithiation discharging, regardless of its actual role in the cell.

2.1.3 SEI Formation

There is only a certain range of redox potentials where all compounds are stable, below this range the compound is reduced and above it is oxidized. Considering that e.g. for a standard graphite anode most of the intercalation happens <0.1 volt relative to the Li/Li + redox couple [18], intercalation of Li into the anode of the Li-ion battery happens at a very low potential, and decomposition of the electrolyte solution constituents is thus virtually inevitable and will happen to at least some degree. By using an electrolyte that, together with the electrode material and Li, decomposes into stable solid compounds and therefore form a coating around the electrode, this problem is circumvented. The coating, commonly referred to as the solid electrolyte interphase (SEI), should ideally prevent further decomposition of solvent by forming an impermeable as well as electronically isolating layer, but still be ionically conducting to allow Li ions to pass from the electrolyte to the electrode.

The SEI forms through a number of parallel and competing reactions, resulting in a coating which is complicate to characterize and to evaluate due to its inhomogeneous composition and varying thickness. Figure 2-4 shows a schematic representation of SEI of a standard carbon anode formed on a graphite particle. It stands to reason, that the composition and efficiency of the SEI is greatly influenced by the composition of the electrolyte. The complexity of the formation makes it sensitive to external influence as well, e.g. varying operating conditions in different laboratories. However, for carbon anodes, which are the most extensively researched, most groups agree that the SEI is composed of multiple layers; a layer consisting

mostly of inorganic salt reduction products closest to the electrode followed by a layer of organic reaction products from the decomposition of the solvents [20].

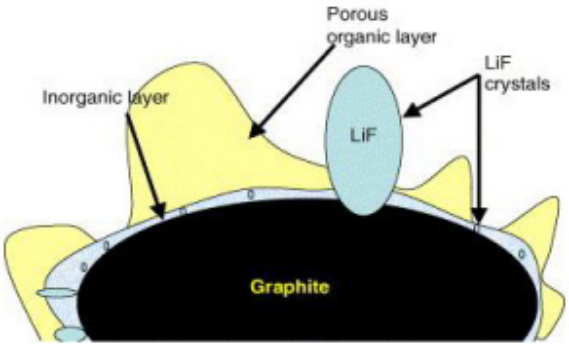

Figure 2-4. Schematic representation of SEI forming on the surface of graphite particles in an anode [20]

While being essential for the successful operation of the Li-ion battery, the SEI also has some adverse effects on the battery performance. The most notable is the capacity loss caused by lithium being irreversibly bound in compounds during the formation of the interphase, observed as a reduced Coulombic efficiency for the first few charge/discharge cycles. The magnitude of this reduction is related to the thickness and composition of the SEI, which in turn can be manipulated by tuning the composition of the electrolyte [21].

2.1.4 Components and Commonly Used Materials

2.1.4.1 Electrolyte solvents

The primary role of the electrolyte in any electrochemical cell is to conduct ions from one electrode to the other while being electronically insulating and thermodynamically stable. The last property can either be a result of the decomposition products passivating the electrode surface by formation of a SEI or intrinsic for the electrolyte. For Li-ion batteries, the former is usually the case, of reasons discussed in the previous Section 2.1.3. The choice of a proper electrolyte

therefore has a great impact on the cycle stability and Coulombic efficiency of the battery. There are three main groups; ionic liquids, polymer electrolytes and liquid electrolytes where a tremendous number of different electrolytes have been designed for use in the Li-ion battery. Only the liquid electrolytes are used in the experiments for this work, but a short introduction to the other classes seems prudent. Being based on salts, ionic liquids are in their molten state at ambient temperature, in which Li salts can be dissolved. These salts have a broad stability window and very low volatility, making them non-flammable. However, research in this area has in the past largely been based on Cl_3 , whose extremely corrosive nature has resulted in a very limited use. In later years, however, a renewed interest has been sparked by the discovery of new low melting temperature salts, mainly based on the quaternary ammonium cation [22]. Of the polymer electrolytes, gel polymers are by far the most common. Gel polymers possess both the diffusive properties of a liquid and the physical properties of a solid. The electrolyte consisting of a polymer host material soaked with an organic solvent, into which a Li salt is dissolved, result in these properties [23]. Advanteous of Li polymer batteries are cheaper and simpler construction, more rugged and resistant to short circuiting, while on the other hand generally being regarded as having a smaller charge capacity than conventional Li-ion batteries. In addition, the absence of a free liquid removes the need for a metal housing and increases flexibility when it comes to battery shape and packaging [24]. Liquid electrolytes are made by dissolution of a Li salt (e.g. $LiPF_6$) in a nonaqueous solvent. Different groups of solvents are outlined by van Schalkwijk et al. (2002) [24] and include ethers, esters, alkyl carbonates and inorganic solvents. The most commonly

used are propylene carbonate (PC), ethylene carbonate (EC), dimethyl carbonate (DMC), diethylene carbonate (DEC), 1,2-dimethoxy ethane (DME), ethyl methyl carbonate (EMC) and 1,2-diethoxy ethane (DEE) [24]. PC was used in early research, but was found to be incompatible with graphitic electrodes due to co-intercalation phenomena. That PC molecules fail to create a stable SEI and intercalate into the electrode, causing a continuous break down of the electrodes by exfoliation of graphite layers is the reason for that. EC, while having a very similar molecular structure to PC, does not cause these problems and has proven to be a more suitable solvent. A binary electrolyte of EC and one of the less viscous DEC, DMC and EMC is commonly found in commercial batteries [25].

2.1.4.2 Solutes

Two main requirements have to be satisfied in order for a Li salt to be applicable as electrolyte solute for Li-ion: 1) the salt must have a high solubility in non-aqueous solvents, to meet the primary purpose of the solute is to provide a sufficient concentration of lithium ions and 2) the anion must be stable in relation to the other components of the battery, either by being inherently so or by passivation. Examples of salts that fulfill these requirements are $LiClO_4$, $LiAsF_6$, $LiPF_6$ and $LiSO_3CF_3$. Apart from these requirements, there are numerous other properties that should be considered, e.g. toxicity ($LiAsF_6$), fire or explosion hazard ($LiClO_4$), low conductivity ($LiSO_3CF_3$) and cost, which narrows down the number of practical candidates considerably [26]. For a fact, the vast majority of Li-ion batteries both in production and research use the same salt as primary solute, namely lithium hexafluorophosphate ($LiPF_6$). This is not because it is a perfect solute, but because

$LiPF_6$ has a good compromise of properties. However, for applications where demands are more extreme, $LiPF_6$ may not fulfill all the requirements. For instance, at high temperatures, the decomposition of $LiPF_6$ into LiF and PF_5 becomes a major problem, as PF_5 readily hydrolyses to form HF, which is devastating for the electrode performance [26]. This has led to research into alternative solutes, like lithium tris(pentafluoroethyl)trifluorophosphate and lithium bis(oxalato)borate, commonly known as $LiFAP$ [27] and $LiBOB$ [28], respectively. These have shown great potential, but are not yet commercialized on a large scale.

2.1.4.3 Cathodes

Although all tested cells in this research are half cells, a short overview over common Li-ion battery cathodes is given here. A few examples out of numerous different cathodes for the Li-ion battery which have been researched through the years, are shown in Table 2-1.

Table 2-1. Examples of cathode materials, their group and the approximate capacity ranges they have been reported to exhibit. Based on material from [29]

Materials	Group/structure	Reported specific discharge capacity
$LiCoO_2$	Layered oxide	100 – 160 mAh/g
$LiMn_2O_4$	Spinel	70 – 140 mAh/g
$LiFePO_4$	Olivine	80 – 155 mAh/g

With only a few exceptions, the majority is made of compounds based on at least one of the transition metals. That transition metals are stable at a several different oxidation states is the main reason for this. When Li ions are intercalated into the

electrode, by being reduced to a lower oxidation state the transition metal atoms can accommodate the electrons arriving through the external circuit, thereby maintaining the charge neutrality of the compound [29].While this applies for a large number of compounds, other essential criteria reduces the number of candidates notably. The large changes in composition of the electrode during lithiation often lead to changes in the crystal structure of the material that may compromise the structural integrity of the electrode or otherwise have energetically unfavorable effects. Therefore, it is to use a material with a crystal structure that is stable over a wide range of compositions. In addition to this, the Li diffusivity, electronic conductivity, cost and environmental compatibility of the material must be taken into account. Since the first development of the Li-ion battery, three main groups of materials have been found to exhibit these properties; layered oxides, spinels and olivines and tavorites.

Layered chalcogenides were discovered first, starting with the sulfides and selenides like $LiTiS_2$ and $LiVSe_2$, before moving on to the oxides, e.g. $LiCoO_2$ and $LiNiO_2$. Closely packed anions provide the main structure of these materials, with the transition metal cations occupying the space between every other layer. The Li can then be freely intercalated into the remaining unoccupied ones, resulting in the layered structure that gives this group its name. The structure itself is named $\alpha - NaFeO_2$ and can be seen in Figure 2-5a [8].

Being quite similar to the first group, the second consists of materials having the spinel structure. However, rather than having the alternating layer structure that was described above, in the spinel structure both of the cation species are ordered throughout all of the atomic layers, as seen in Figure 2-5b. This ordered spinel

structure provides an interconnected matrix of interstitial positions that allows for the storage and diffusion of Li ions, again while the transition metal atoms accommodate the electrons by changing oxidation state [30].

The last group, the olivine materials, were developed with an extensive research effort into making electrodes based on iron, being the best available transition metal by far. The effords resulted in $LiFePO_4$ [8], whose structure, seen in Figure 2-5c, consists of edge sharing octahedra of oxygen coordinated iron atoms forming layers which are bound together by tetrahedra of oxygen coordinated phosphorous atoms, between which lithium atoms can reside. Made only of materials of abundant availability and having capacities comparable to that of $LiCoO_2$, as well as very good cycle life, low toxicity and being environmental compatibility, it has attracted great interest. Its defining limitation has been an extremely low electronic conductivity, for which making composites with carbon has been the most common solution [31].

Corresponding compounds of other transition metals like manganese, nickel and cobalt have also been investigated. None of these have shown any superior electrochemical performance, however, and the materials are far more costly, hence the interest in these compounds has been limited [8]. Tavorite phase materials like $LiFeSO_4$F have been found to exhibit similar properties as the olivine phases. Its structure, which can be seen in Figure 2-5d, also consists of layers of octahedra, but unlike in the olivine structure, these share corners and are coordinated by both oxygen and fluorine atoms, while the layers themselves are separated by tetrahedra of oxygen and fluorine coordinated sulfur atoms [32].

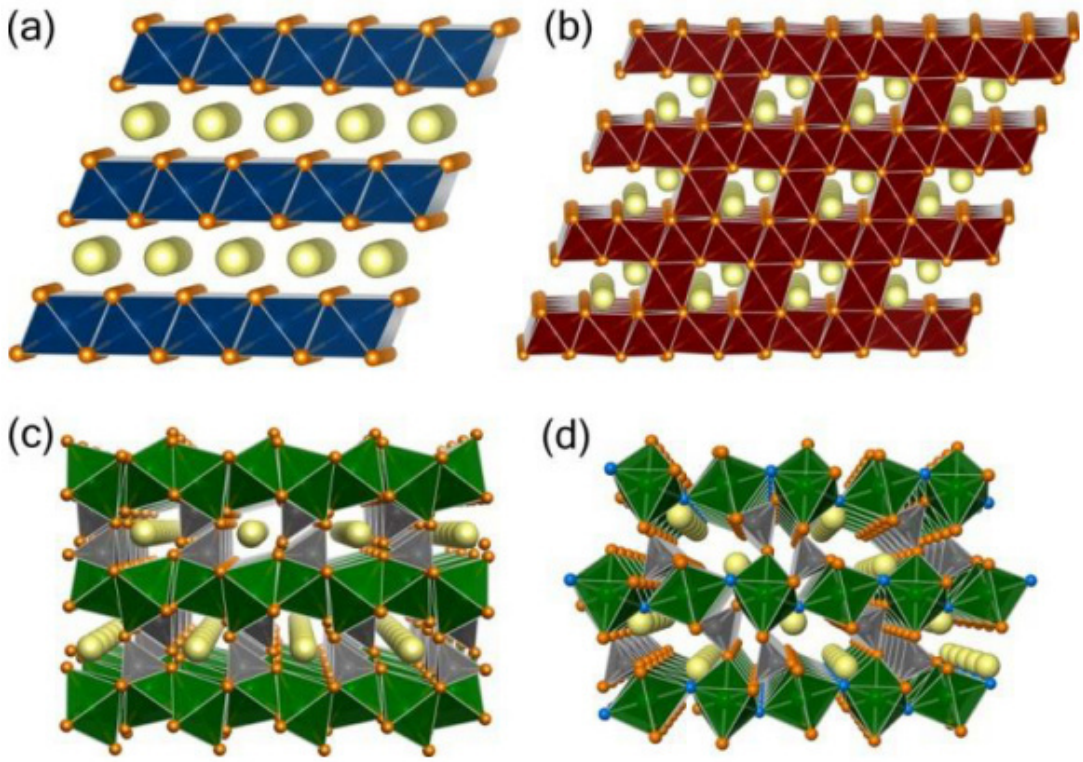

Figure 2-5. Illustration of the crystal structures of the best performing positive electrode materials: (a) O_2 , (b) $LiMn_2O_4$, (c) $LiFePO_4$, and (d) the tavorite-phase of $LiFeSO_4F$. Li atoms are shown in yellow while the transition metals polyhedra for Co, Mn, and Fe are shown in blue, red, and green, respectively. The polyhedra are coordinated by oxygen atoms in orange and fluorine in blue. [32]

2.1.4.4 Anodes

2.1.4.4.1 Carbon anodes

Carbon polymorphs have commonly been regarded as the standard material for Li-ion batterie anodes. While the use of carbonaceous materials as intercalation electrode material was proposed as early as in the patent describing the first ever lithium-ion secondary battery by Yoshino et al. (1987) [33], it has yet to be succeeded as the standard anode material. Excellent cycle life, good material availability and low cost are the attributes leading to this favored position. The vast majority of the carbonaceous electrodes are made from graphite or graphitable carbons, for which the intercalation mechanism has been widely studied and is well known [34]. However,

lithiation into graphitic electrodes is limited by the composition of the most Li rich phase in the Li-graphite system. With an upper limit of LiC_6, this results in a relatively low theoretical maximum capacity of ~372 mAh/g, above which Li metal is formed. This has prompted research into alternative anode materials, including both more advanced carbon based electrodes, alloys and composites [35], [36].

Hard carbons prepared by pyrolysis of organic material are widely seen as a promising alternative carbon material and therefore acquired some research intrest. Only a short range ordering and various surface termination groups can be attained using this process, depending on the precursor and pyrolization temperature. The process of Li intercalation into such materials is not easily determined because of the lack of long range order and varying composition, hence the theoretical capacity limit is not known. However, it has been established that that at least some of these materials exhibit far higher capacities than the limit for graphitic carbon. Yet, while the lithium insertion capacity may be very high, these materials suffer from very large irreversible capacities, severely limiting their practical applicability. There are other carbon polymorphs like kish graphites and multi-walled carbon nanotubes (MWCNTs) which are possible alternative carbon materials [35]. While strictly being a member of graphitable carbons, kish graphite have proven to have capacities reaching ~20% above the theoretical limit of perfect graphite, indicating a certain degree of disorder [37].

MWCNTs, on the other hand, are rather expensive, but have still attracted a fair share of attention due to the many potential mechanisms of lithium intercalation, namely in the graphene sheets constituting the tubes, in the space between the tubes

formed due to imperfect packing, and inside the tubes themselves. However, as with the hard carbons, the irreversible capacity is too high for this kind of electrodes to be commercially viable [35].

2.1.4.4.2 Alloying anodes

In order to replace carbonaceous anodes with anodes having a higher capacity, experimental work on anodes using chemical elements which form alloys with lithium was started in early 1960s.[38] In 1971, Dey [39] found that Li can be electrochemically alloyed with a number of metals at room temperature, including Si, Sn, Pb, Al, Au, Pt, Zn, Cd, Ag, and Mg. Before, Silicon, the theme of this thesis, will be covered in further detail in the following section, a brief summary of the common features of the alloy anode materials is given here. Because of their availability, price and environmental sustainability, Si, Sn, Sb, Al, and Mg have been most extensively examined for this purpose [36]. As following from the key electrode properties of these alloy anode materials and graphite, shown in Table 2-2, the potential capacities of alloy forming electrodes are far superior to that of the graphite anode. The specific capacities of intercalation anodes come close to that of the Li metal anode. As a matter of fact, the amount of Li some alloy electrodes can accommodate per volume exceed that of metallic Li itself, e.g. $Li_{22}Si_5$ contains 88.56 mol Li/L, while lithium metals only contain 76.36 mol Li/L [40]. This is partly caused by the fact, that Li is stored in ionic rather than atomic form in the alloy electrodes and partly because metallic Li is not in a close packed crystal structure, and therefore have a potential for densification.

In addition, from a safety-perspective, alloy anodes are also superior to carbon anodes. Lithiation of the alloys happen at potentials ranging from 0.1V to 0.9V (Table

2-2), compared to the carbon anode where lithiation typically happen around 0.05V. On the one hand, this reduces the voltage of the cell, and consequently the specific energy, on the other hand it also reduces the probability of accidental deposition of metallic Li on the electrode surface during fast charging [36]. In many industries safety benefits like this are significant, e.g. in the automotive industry [41].

Apart from excellent capacity and safety benefits, there are several other characteristics that are necessary to make a suitable anode material. Especially in cycling stability and Coulombic efficiency, these alloy anodes have been found to be seriously lacking. Due to the high electropositivity of Li, many of the intermetallic phases formed by Li and group 13-16 metals or metalloids are of highly ionic character. These are generally known as Zintl-phases and are usually brittle.

An increase in volume of the material is caused by the reduction of the otherwise neutral host atoms which results in a substantial diameter increase. In contrast, the Li-ions can occupy interstitial positions in the lattice, and hence cause only a limited volume expansion [40]. This is obvious from Table 2-2, where expansions of up to 420% are observed for the alloy materials, compared to 12% for the graphite electrode. During cycling, this volume change introduces large stresses into the electrodes. In combination with the brittleness of many of these materials, these stresses can eventually lead to cracking of the electrode [42].This is associated with partially contact loss of the electrode material or the electrode itself detaching from the current collector. The result of these effects is an irreversible capacity fade by causing electrode material to become essentially dead weight. The pulverization leads to a continuous formation of new surface area, which must be stabilized by forming an

SEI, as described in Section 2.1.3. This process involves irreversible loss of Li in anodes made with these materials, finally yielding to the observed low Coulombic efficiency.

All there effects are challenges to overcome in the research on the way to a successful alloy anode. However, as the potential benefits are of such magnitudes, these are challenges for which there has been proposed numerous solutions. Concrete examples of this will be discussed in more detail in Section 2.2.2.

Table 2-2. Comparison of various materials (all the capacity numbers are based on materials in the delithiated state except lithium metal).[13]

Materials	Li	C	Li_4Ti_5O	Si	Sn	Sb	Al	Mg
Density [g/cm^3]	0.53	2.25	3.5	2.3	7.3	6.7	2.7	1.3
Lithiated phase	Li	LiC_6	$Li_7Ti_5O_{12}$	$Li_{4.4}Si$	$Li_{4.4}Sn$	Li_3Sb	LiAl	Li_3Mg
Specific capacity mAh g^{-1}	3862	372	175	4200	994	660	993	3350
Volume change [%]	100	12	1	420	260	200	96	100
Potential vs. Li [V]	0	0.05	1.6	0.4	0.6	0.9	0.3	0.1

2.2 The Silicon Anode

The formation of Li–Si alloys in high temperature cells operating in the 400 - 500°C range was first reported by Sharma and Seefurth [43] in 1976. It was reported that the alloying process in silicon anodes results in formation of $Li_{12}Si_7$, $Li_{14}Si_6$, $Li_{13}Si_4$, and $Li_{22}Si_5$ alloys (Figure 2-7) [44]. It was indicated by studying the Li–Si binary system [39], [43]–[45] that $Li_{22}Si_5$ is the highest alloy stage, so each silicon atom can accommodate 4.4 Li atoms, i.e., a specific insertion capacity of 4200mAhg^{-1}, the highest among the alloying elements. Figure 2-7 shows the lithiation and delithiation curve at room and high temperature.

In addition to its outstanding capacity, silicon is the second most abundant element on earth. Because of these attributes, a great proportion of research has focused on using silicon as Li-ion cell anode material. However, at room temperature the alloying process of Li with Si was found to be less reversible [46]–[48]. Figure 2-6 shows an example of the charge/discharge curves of Si powder with an average size of 10μm, during the initial cycle a bulk-silicon anode showed a charge capacity above 3260mAhg^{-1} and a discharge capacity close to 1170mAhg^{-1}, corresponding to a Coulombic efficiency of only 35% [49].

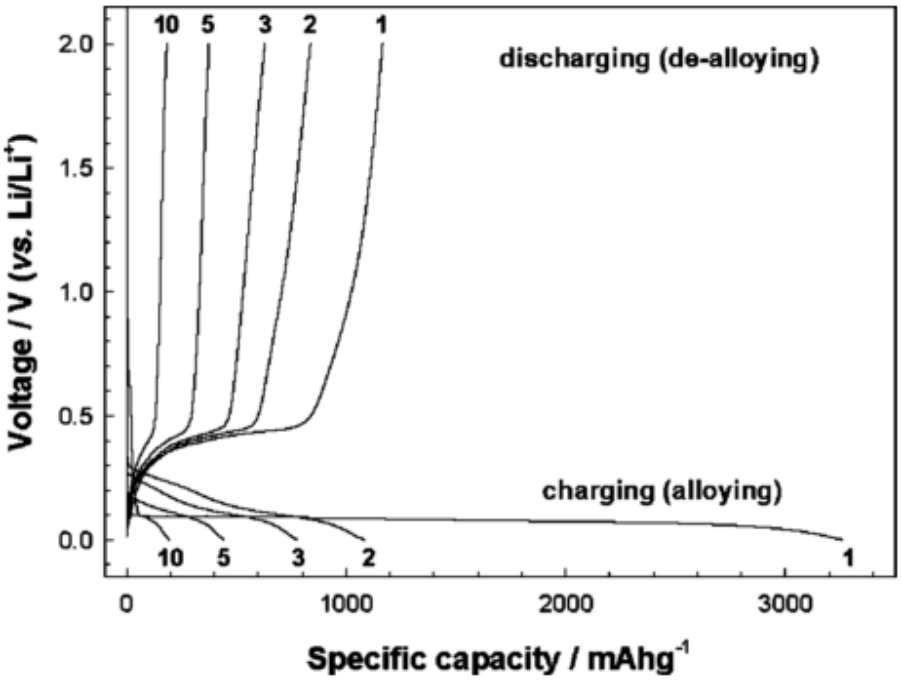

Figure 2-6. Galvanostatic charge-discharge voltage profiles obtained with a silicon powder anode. [49]

The cycling characteristics of Si are described using this example. During lithiation (charging) in the first cycle, the voltage initially dropped quickly to 0.2V versus Li/Li^+ in the liquid organic electrolyte used and then a slow decrease took place as seen in the long potential plateau in Figure 2-6. This plateau is due to formation of Li–Si alloys. During the discharge process, a rapid increase in voltage was observed, followed by a plateau between 0.3 and 0.4V. From the initial charge-discharge profile, it was evident that silicon anodes operate in a narrow potential range between 0.0 and 0.4V (Figure 2-6), which would be suitable for use in Li-ion cells. During further cycling, rapid capacity fade was observed, which resulted in a reversible capacity lower than $500mAhg^{-1}$ by the 5th cycle. Li insertion in Si results in the formation of progressive Li–Si alloys, each of which result in successively larger volume expansions of the parent lattice. Table 2-3 shows the data for crystal structure, unit cell volume, and volume per Si atom for each alloy formed during the alloying process.

Since the number of Si atoms is constant, the relative volume increase of the anode can be established by calculating the volume of electrode per Si atom in each of these phases. This can be expressed by

$$V_{\text{Si atom}} = \frac{V_C}{N_{Si}} \tag{2.2-1}$$

With V_C and N_{Si} being the unit cell volume and the number of silicon atoms in the unit cell, respectively.

Table 2-3. Crystal structure, unit cell volume and volume per Si atom for the Li-Si system [44]

Compound and crystal structure	Unit cell volume [A^3]	Volume per silicon atom[A^3]
Silicon cubic	160.2	20.0
$Li_{12}Si_7$ ($Li_{1.71}Si$) orthorhombic	243.6	58.0
$Li_{14}Si_6$ ($Li_{2,3}Si$) rhombohedral	308.9	51.5
$Li_{13}Si_4$ ($Li_{3,25}Si$) orthorhombic	538.4	67.3
$Li_{22}Si_5$ ($Li_{4,4}Si$) orthorhombic	659.2	82.4

It shows that the volume per silicon atom for $Li_{22}Si_5$ alloy is four times higher than that of the parent silicon atom, i.e., a 420% volume expansion of the silicon lattice occurs. This result in cracking and disintegration of the electrode, with active material loss via reduced electronic contact, giving severe capacity fade.

According to the equilibrium phase diagram, when lithium is inserted into Si, Si should undergo a series of phase transformations, theoretically resulting in multiple voltage plateaus in the galvanostatic voltage curve (Figure 2-7, black line). [50]

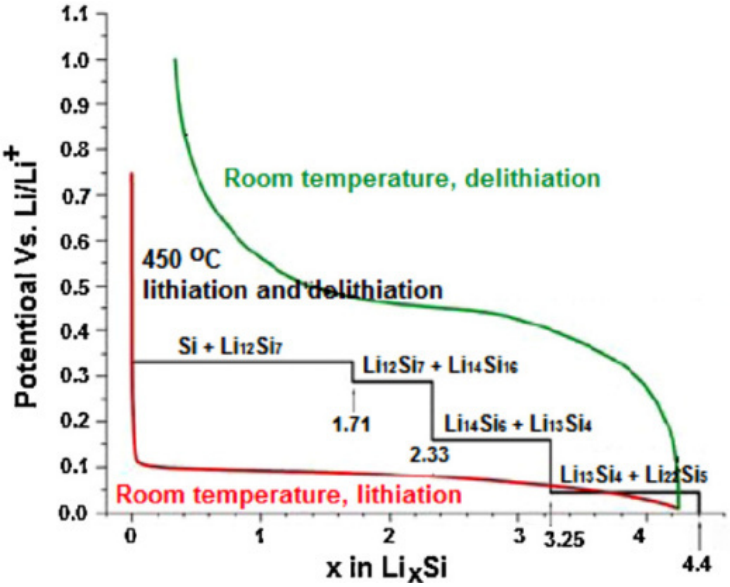

Figure 2-7. Si electrochemical lithiation and delithiation curve at room temperature and high temperature. Black line: theoret- ical voltage curve at 450 ◦C. Red and green line: lithiation and delithiation of crystalline Si at room temperature, respectively.[51]

However, this only takes place at high temperature. At room temperature, crystalline Si goes through a single crystalline-to-amorphous phase transformation during the first lithiation and remains amorphous afterwards (Figure 2-7, green and red line).

2.2.1 The Breakdown Mechanism

As you can see in Table 2-3, the volume expansion versus the concentration of Li is nearly linear. Various methods [52]–[55], including X-ray diffraction and nuclear magnetic resonance, have been used to study the amorphization process; these studies have primarily shown experimental evidence for the crystalline-to-amorphous phase transition and have also provided information on the local atomic structure of the

amorphous phase. In addition, atomic force microscopy has been used to show that volume expansion occurs during lithiation and contraction occurs during delithiation of Si thin films [56]–[60]. Based on the studies, three fundamental materials challenges to using Si as a viable battery electrode, as illustrated in Figure 2-8, can be outlined.

(1) **Material pulverization**. The large volume expansion/contraction during lithiation/delithiation induces large stresses. These stresses can cause cracking and pulverization of the Si, which leads to loss of electrical contact and eventual capacity fading (Figure 2-8a). This mechanism probably accounts for most of the capacity fade observed in early studies using bulk Si, films, and large particles of Si.

(2) **Morphology and volume change of the whole Si electrode**. The large volume changes also cause significant challenges at the level of the entire electrode. During lithiation, Si particles expand and impinge on each other. During delithiation, Si particles contract, that can result in detachment of their surrounding electrical connections (Figure 2-8b). This drastic electrode morphology change can further contribute to capacity fading. In addition, the total volume of the whole Si anode also increases and decreases upon lithiation and delithiation, leading to electrode peel-off and failure, which creates challenges for full cell design.

(3) **Solid-electrolyte interphase**. When the potential of the anode is below ~1V versus Li/Li+, the decomposition of the organic electrolyte at the electrode surface is thermodynamically favorable (see Section 2.1.3). This layer needs to be dense and stable, and it should be ionically conducting and electronically insulating in order to prevent further side chemical reactions from occurring. The formation of this passivating SEI film on the Si surface has been confirmed by HRTEM, FTIR, and XPS [20], [61]–[63]. The SEI films consist mainly of Li_2CO_3, various lithium alkylcarbonates ($ROCO_2Li$), LiF, Li_2O, and non-conductive polymers [20], [61], [62]. The SEI stability at the interface between Si and the liquid electrolyte is a critical factor for obtaining long cycle life. However, the large volume change makes it very challenging to form a stable SEI. As illustrated in Figure 2-8c, Si particles expand out towards the electrolyte upon lithiation and contract during delithiation. The stresses produced by the volume changes induce structural modifications of the Si phase and create damages in the solid-electrolyte interphase (SEI). The SEI is produced by the decomposition of the organic electrolytes on the electrode material. For a long cycle life the presence of an ionically conductive and electronically insulating stable SEI layer is critical. The Si shrinkage during the delithiation steps makes the SEI layer vulnerable to cracking and exfoliation, with breakage of electrical

contact between active material and current collector and consequent rapid failing of the electrode [9,12].

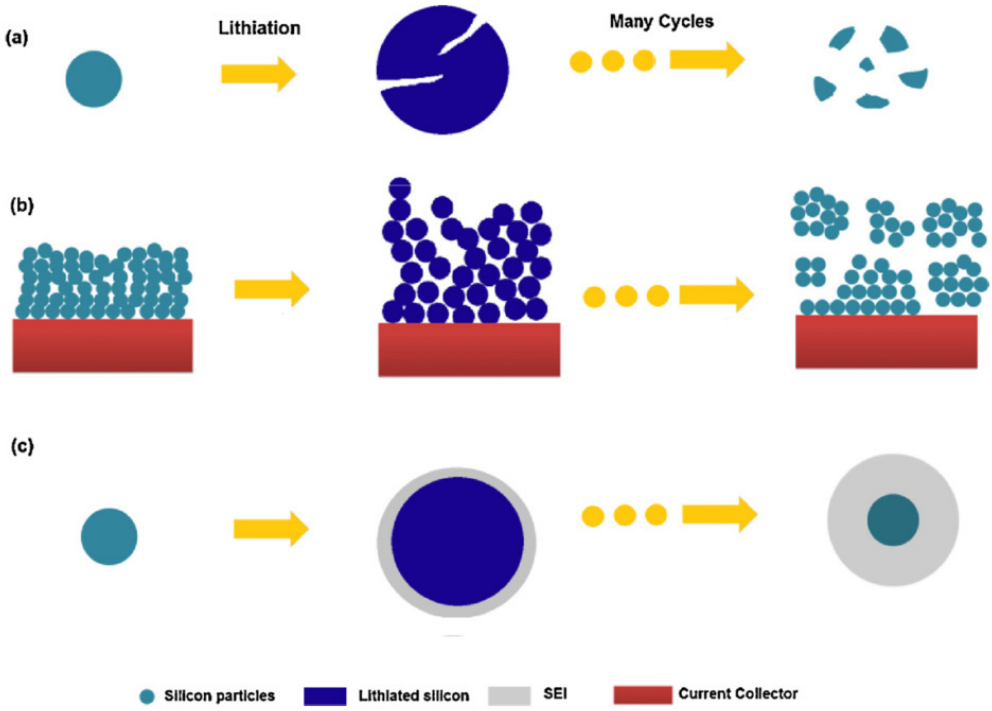

Figure 2-8. Si electrode failure mechanisms: (a) material pulverization. (b) Morphology and volume change of the entire Si electrode. (c) Continuous SEI growth.[51]

2.2.2 Previous Electrode Designs

To overcome the problems of material pulverization, detachment of the electrode material and SEI formation (see Section 2.2.1), several nanostructured Si anode designs have been studied. As shown in Figure 2-9 the cycling performance and capacity fading is strongly depending on the electrode design. The capacity of the bulk silicon anode fades over only a few cycles, while the utilization of nanocrystals and nanofilms improves the capacity retention to over 50% for the nanocrystals and over 80% for the nanofilm. This example shows already shows the great potential of different anode architectures, so through the last decades, a large number of different

electrode designs have been researched. An overview of which will be given in this section.

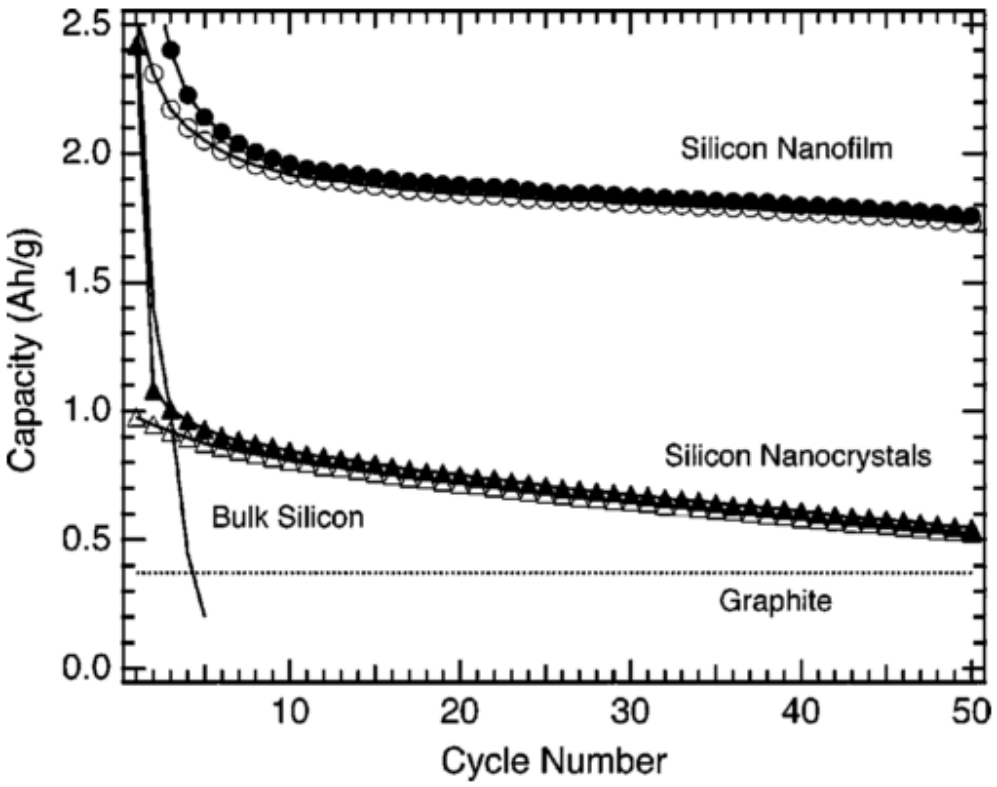

Figure 2-9. Specific capacity vs. cycle number for different silicon anode designs[64]

Table 2-4 shows several anode designs which have been evaluated over the past decade. All these investigations are done, also the work in this thesis, is done, because the initial attempts were not satisfying in capacity and cycle stability. [12], [49]

Table 2-4. Silicon anode designs and their reported performance

Design	Research Group	Reported performance
0-dimensional structures		
Conductive and elastic binder	Magasinski et al. (2010) [65]	2,500 mAh/g for 100 cycles
Porous Si nanoparticles	Ge et al. (2012)[66]	1,400 mAh/g for 200 cycles
1-dimensional structures		
Nanowires	Chan et al. [67]	3,500 mAh/g for 20 cycles
Carbon-silicon core-shell nanowires	Ruffo et al. (2009) [68]	2,000 mAh/g for 80 cycles
Nanotubes	Park et al. (2009) [69]	3,200mAh/g for 200 cycles
Double walled Si nanotubes	Wu et al. (2012) [70]	2,970 mAh/g for 6000 cycles
2-dimensinoal structures		
50 nm pure silicon film	Takamura et al. (2004) [71]	2,000 mAh/g for 3000 cycles
3-dimensional structures		
Ternary silicon nanoparticles /conducting polymer/carbon nanotubes hybrid anode	Liu et al. (2013) [72]	1,600 mAh/g for 1000 cycles
Bath lily-like graphene sheet-wrapped nano-Si composite	He et al. (2011) [73]	1,500 mAh/g for 30 cycles
Pomegranate-inspired nanoscale design	Liu et al. (2014) [74]	1,160 mAh/g for 1000 cycles

2.2.2.1 0-dimensional structures: Si nanoparticles

Silicon nanoparticles are one of the most promising candidates for LIB electrodes for the following reasons. Synthesis methods for silicon nanoparticles are rather sophisticated, and Si nanoparticles are commercially available.[75] Secondly, Li-ion battery electrodes with Si nanoparticles could be produced with the current manufacturing process. [76], [77] Finally, reducing the size of silicon particles will help to release the stress and prevent the cracking of silicon during the Li insertion, which will significantly improve the cycling performance of the electrodes. [75], [78]

However, Si anodes with nanoparticles suffer from rapid capacity changing due to the breakdown mechanisms described in Section 2.2.1. Strategies to improve the nanoparticles approach have also been investigated. These include the utilization advanced binders like PAA (2500 mAh/g for 100 cycles [65]) or porous Si nanoparticles (1400 mAh/g for 200 cycles [66]).

2.2.2.2 1-dimensional structures: nanowires and nanotubes

In 2007, Chan et al. [67] reported a Si anode design concept utilizing Si nanowires prepared by the vapor-liquid-solid synthesis method. By growing these thin wires directly on a stainless steel current collector, a significant improvement of the electrochemical performance, compared to thick films and large particles. [67] The better performance of 3500 mAh/g for 20 cycles at C/5, is due to the sufficient empty space between adjacent NWs, hence the lithiation and delithiation process does not cause damage to the anode. However the material will undergo large volume changes but these do not lead to a disconnection from the current collector. Since the NWs form a one dimensional electronic pathway to the current collector, the addition of

conductive carbon and polymer binder becomes unnecessary. The basic concept was adopted by many other research groups [51], but soon reached its limitations in terms of cycling stability.

Trying to improve the NW concept first, carbon-coated Si NWs were investigated. Having observed a rapid capacity fading of the uncoated Si NW electrode over only 10 cycles, indeed the carbon-coated Si NW electrodes exhibited a stable reversible capacity of 1326 mAh/g after 40 cycles. [79]

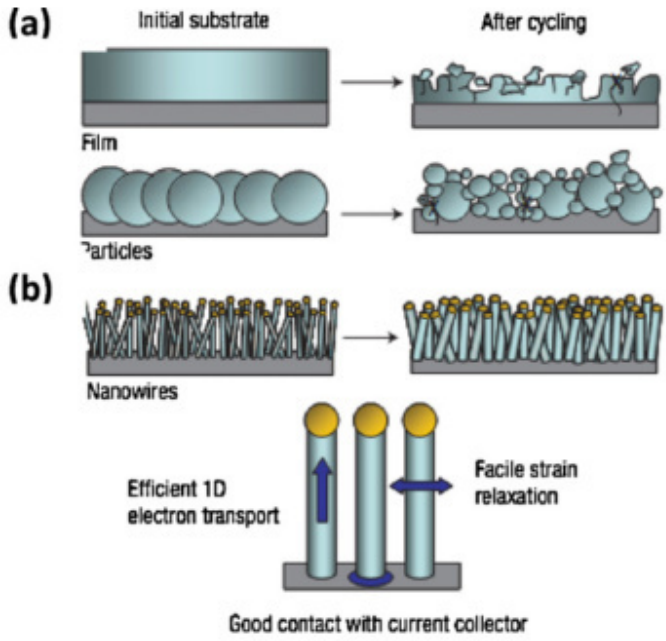

Figure 2-10. (a) Breakdown of thick films and large particles during cycling. (b) Si NW directly grown on the current collector which does not pulverize [67]

However it was shown by Ruffo et al. (2009) [68], that carbon-silicon core-shell NWs are far more effective. The core material is structurally stable carbon and the shell material is the active Si for storing the Li ions. Ruffo et al. (2009) [68] demonstrated a superior power rate and cycle life (2000 mAh/g for 80 cycles at C/5).

Apart from these solid structures, hollow Si nanotubes are another interesting concept. The increased surface area allows the Li ions to intercalate from both, the

interior and the exterior of the nanotubes. The nanotube electrodes demonstrated reversible charge capacities of ~3200mAh/g with capacity retention of 89% after 200 cycles at a rate of 1C in practical lithium ion cells with improved rate stability [69]. A further development step has been double walled Si nanotubes. These are able to form a stable SEI by forming an oxide coating layer on the outer surface. The outside SiO_x coating layer is mechanically strong and can successfully prevent the Si from expanding outward while still allowing lithium ions to pass through. along with the mechanical robustness and short diffusion length, these Si nanotubes show extremely high cyclability at high rates. Wu et al. (2012) [70] demonstrated a capacity retention of 88% after 6000 cycles with a high specific capacity of 2970 mAh/g at C/5.

2.2.2.3 2-dimensional structures: thin film

Besides the composite electrodes, another main group of electrodes; thin-films, have received a fair share of attention. The motivation for using thin-films compared to composites is that they contain no inactive components, and thus have a higher effective specific capacity [38]. Being essentially bulk silicon, the performance deteriorate quickly when film thickness approaches 1µm [12]. However, thin films have demonstrated extremely good performance even at high charge and discharge rates, e.g. 50 nm films cycled at 30C that retain a capacity of over 2000 mAh/g even after 3000 cycles [71]. However, as a 50 nm pure silicon film is equivalent to a material loading of only 13.25 µg/cm^2. (for a silicon density of 2,65 g/cm^3). The active area would have to be immense to obtain a usable capacity and the mass of the associated current collectors would be considerable. On the other hand, far thicker films have been made with acceptable results, and much effort is still being put to the

task. Approaches include making binary and ternary alloy thin films, and while not yet commercialized, they show much promise [38].

2.2.2.4 3-dimensional structures: various designs

A large potential in fabricating Si anodes lies in the formation of three-dimensional structures. These provide the possibility of high loadings, and potentially the control of SEI formation while providing enough void spaces or being elastic enough to compensate the volume changes of Si during cycling. Various designs have already been tested, and the possibilities are almost unlimited, but to give a general introduction in this topic, three examples will be further described in this section.

Ternary silicon nanoparticles/conducting polymer/carbon nanotubes hybrid anode

This anode design basically combines the results of studies of carbon nanotubes [69], [70] with more elastic and conductive binders [76], [80]. Si nanoparticles wrapped in a three-dimensional hierarchically porous nanostructured conductive polypyrrole framework with single-walled carbon nanotubes as the electronic fortifier as shown in Figure 2-11. [72]

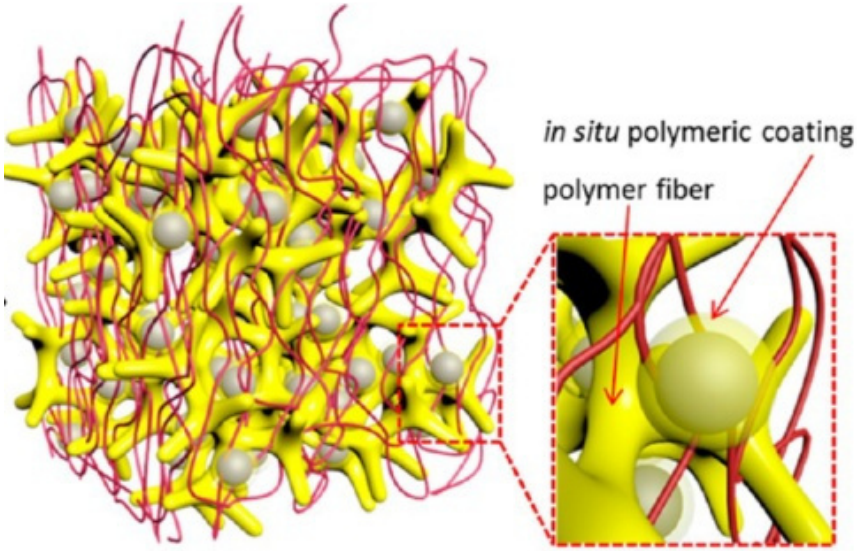

Figure 2-11. Schematic illustration of the formation of 3D Si/PPy/CNT ternary electrode. [72]

Each Si nanoparticle is encapsulated within a thin polymeric coating layer and closely incorporated within the conductive polypyrrole framework. The SWCNTs act both as the wrapping layer and conductive backbone, which further enhance the integration of Si nanoparticle/conductive polymer framework and electric conductivity of the electrode.

Using the hierarchically designed 3D ternary nanostructured electrode Liu et al. (2013) [72] achieved a reversible capacity of ~1600 mAh/g and an average Coulombic efficiency of ~99.5% over 1000 cycles. Moreover, the capacity retention sustained over 85% after 1000 deep cycles in the potential window of 0.01−1V versus Li/Li+.

Bath lily-like graphene sheet-wrapped nano-Si composite

Searching for a low-cost, safe and environmentally friendly procedure to fabricate Si anodes, He et al. (2011) [73] developed the concept of a bath lily-lile graphene sheet-wrapped nano-Si composite as a high performance anode material for

Li-ion batteries. They used commercialized Si powder and graphene sheets and spray-dried a mixture of both to obtain a composite powder. In the end the obtained graphene oxide-wrapped Si microparticles are reduced in a stream of hydrogen/argon (2:8) at 700°C for 3 h to convert to the bath lily- like graphene sheet-Si composite (see Figure 2-12)

He et al. (2011) [73] reported a capacity of more than 1500 mAh/g which is equivalent to a capacity retention of about 88% after 30 cycles.

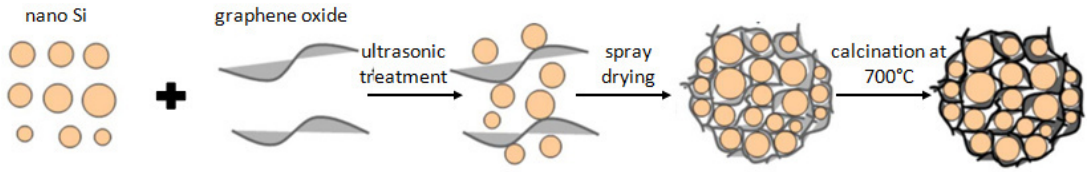

Figure 2-12. Schematic of the formation process of bath lily-like graphene sheet-wrapped nano-Si (GS-Si) composite. [73]

Pomegranate-inspired nanoscale design

Liu et al. (2014) [74] designed a Si anode with the structure of a pomegranate. They used nanosize single Si particles which are encapsulated by a conductive carbon layer that leaves a well-defined internal void space for expansion and contraction. An ensemble of these hybrid nanoparticles is then encapsulated by a thicker carbon layer in micrometre-size pouches to act as an electrolyte barrier. The carbon framework functions as an electrical highway and a mechanical backbone so that all nanoparticles are electrochemically active. It also encapsulates the entire secondary particle, limiting most SEI formation to the outer surface instead of on individual nanoparticles, which not only limits the amount of SEI, but also retains the internal void space for silicon expansion As a result of this hierarchical arrangement, the SEI remains stable and spatially confined, resulting in superior cyclability (97% capacity retention after 1,000

cycles). In addition, the microstructures lower the electrode–electrolyte contact area, resulting in high Coulombic efficiency (99.87%) and volumetric capacity (1,270 mAh/cm^3), and the cycling remains stable even when the areal capacity is increased to the level of commercial lithium-ion batteries (3.7 mAh/cm^2).

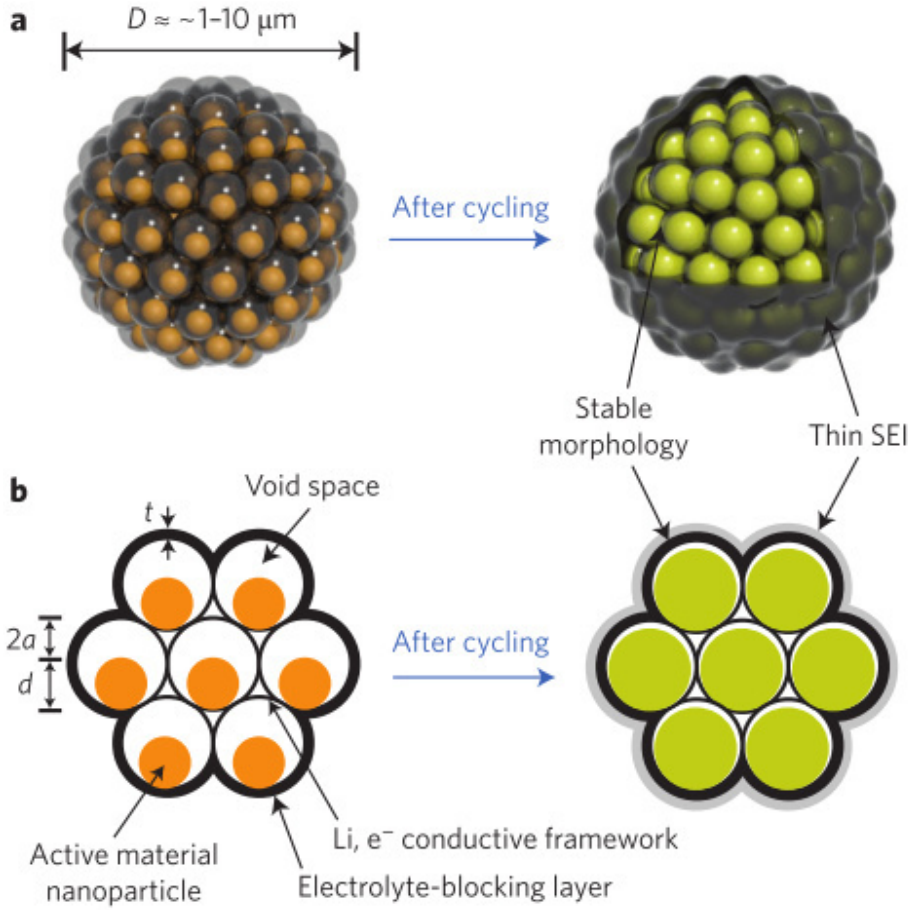

Figure 2-13. Schematic of the pomegranate-inspired design. a,b, Three- dimensional view (a) and simplified two-dimensional cross-section view (b) of one pomegranate microparticle before and after electrochemical cycling (in the lithiated state).[74]

2.3 Pickering Emulsions

An emulsion, being part of the more general colloid class, is a mixture of two or more liquids that are normally immiscible. In an emulsion, one liquid (the dispersed phase) is dispersed in the other (the continuous phase). Pickering emulsions are emulsions of any type, either oil-in-water (o/w), water-in-oil (w/o), or even multiple, stabilized by solid particles in place of surfactants [81]–[83] (Figure 2-14).

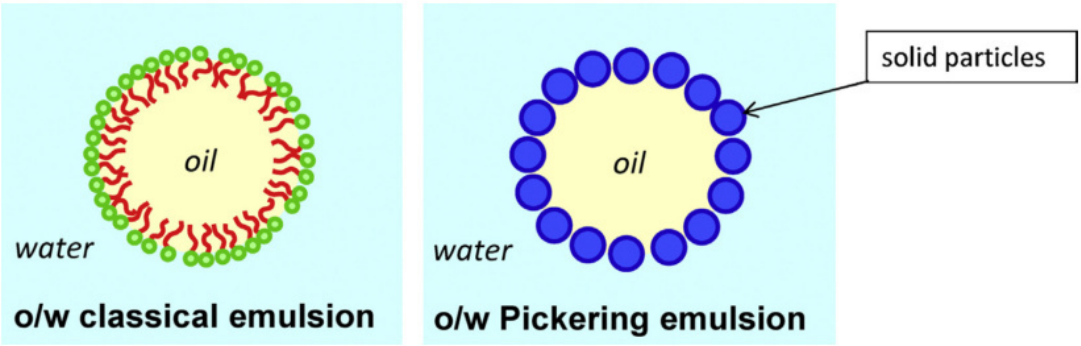

Figure 2-14. Sketch of a Pickering emulsion and a classical (surfactant-based) emulsion. The solid particles adsorbed at the oil–water interface stabilize the droplets in place of the surfactant molecules.[84]

A new class of emulsion stabilizers is represented by particles represent a different class of emulsion stabilizers. Mixing oil and water forms small droplets which are dispersed throughout the water. Driven by the thermodynamic force to reduce the total amount of energy in the system, the droplets will eventually coalesce. However, if solid particles, that are able to form Pickering emulsions, are added to the mixture, they will bind to the surface of the interface and hinder the droplets from coalescing, thus causing the emulsion to be more stable. A high stability is mainly achieved by the fact that particles can absorb almost irreversibly to liquid–liquid interfaces, allowing emulsions even extremely low concentrations of the dispersed phase. In addition, intrinsic surface, thermal, optical and electrical and magnetic

properties of particles can be exploited to produce emulsions that have greater functionalities than surfactant stabilized ones. [85]

2.3.1 Physical chemistry of Pickering emulsions

The two main criteria of an emulsion to fulfill are the feasibility of emulsification and time stability against any destabilization phenomenon (coagulation, coalescence, Ostwald ripening). In order to establish Pickering emulsions the proper adjustment of a suitable formulation and an efficient process are of particular importance. The long term stability mainly depends on the formulation; but the process also matters since the droplet size is often governed by the shear rate of the emulsification process. However, apart from the process, also the physical chemnistry of the stabilizing agent are of significant importance. These properties encompasses the phenomena of adsorption of particles, droplet stabilization by adsorbed particles, kinetics of adsorption that influence the emulsification process and rheological properties that control creaming and sedimentation. [84]

2.3.2 Adsorption of nanoparticles at interfaces

Adsorption of solid particles at the oil–water interface requires the partial wetting of the solid by water and oil. This is depending on interfacial energies of the three interfaces: solid–water, solid–oil, and oil–water, respectively γ_{s-w}, γ_{o-w} and γ_{o-w}. Partial wetting of the solid by water inside an oil medium requires that the adhesion energy of water, $E_{Adh}(w/o)$, is positive and the spreading coefficient of water, $S(w/o)$, is negative [84]:

$$E_{Adh}(\mathrm{w/o}) = \gamma_{s-o} + \gamma_{o-w} - \gamma_{\mathrm{s-w}} > 0 \qquad (2.3\text{-}1)$$

$$\mathrm{S(w/o)} = \gamma_{s-o} - \gamma_{o-w} - \gamma_{s-w} < 0 \tag{2.3-2}$$

An equivalent point is to consider the wetting of the solid by oil inside a water medium where the positive adhesion energy, $E_{Adh}(o/w)$, and the negative spreading coefficient, $S(o/w)$, of oil read [84]:

$$E_{Adh}(o/w) = -\mathrm{S(w/o)} = \gamma_{s-w} + \gamma_{o-w} - \gamma_{s-o} > 0 \tag{2.3-3}$$

$$S(o/w) = -E_{Adh}(w/o) = \gamma_{s-w} - \gamma_{o-w} - \gamma_{s-o} < 0 \tag{2.3-4}$$

Solid particles with very hydrophobic or hydrophilic surfaces do not adsorb because they would be totally wetted by the oil or water respectively. Therefore they remain in the according phase.

Under partial wetting conditions, the contact angles in water, θ_w, and in oil, θ_o, are given by the Young's law ($\theta_o = \pi - \theta_w$) (see Figure 2-15):

$$\cos(\theta_w) = \frac{\gamma_{s-o} - \gamma_{s-w}}{\gamma_{w-o}}; \quad \cos(\theta_o) = \frac{\gamma_{s-w} - \gamma_{s-o}}{\gamma_{w-o}} \tag{2.3-5}$$

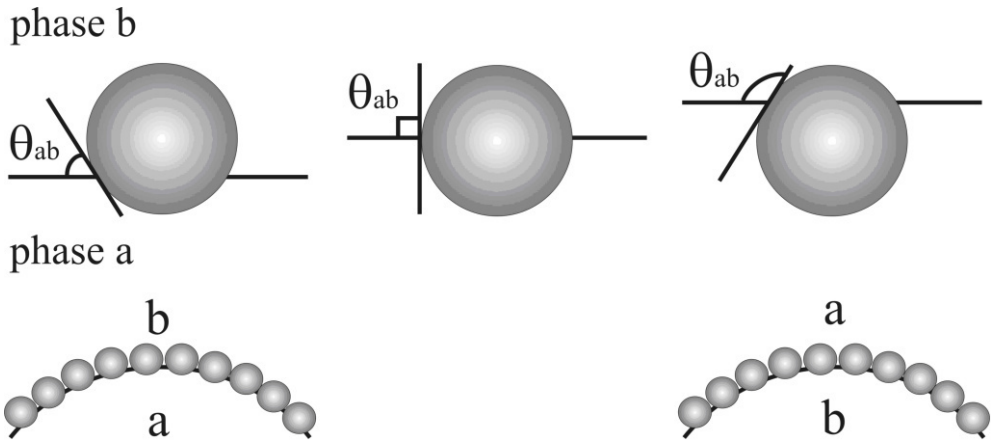

Figure 2-15. Schematic representation of a single droplet stabilized by solid particles and influence of the contact angle on the preferred emulsion state

Adsorption of solid particles under partial wetting conditions is very strong. The free energy of adsorption (the free energy input required for desorption of one particle, either into the aqueous or the oil phase) is related to the interfacial tensions

and the size of the solid particles. Since spontaneous entry of particles into liquid-fluid interfaces is slow,[86] so mixing is used to accelerate this process. The energy ΔE required to detach a spherical particle from an oil–water interface into either bulk phase is given by [84]

$$\Delta_{ads}E = -\pi R^2 \gamma_{o-w}(1 - cos(\theta_w))^2 \; for \; \theta_w < 90^{\circ} \tag{2.3-6}$$

$$\Delta_{ads}E = -\pi R^2 \gamma_{o-w}\,(1 + cos(\theta_w))^2 for \; \theta_w > 90^{\circ} \tag{2.3-7}$$

The maximum stability of the emulsion is reached at a contact angle of 90° in most cases [87]. Obviously, corresponding to the influence of the radius in Eqs. (2.3-6) and (2.3-7), large particles experience a larger adsorption free energy due to a larger area contacting oil and water. However, nanoparticles strongly adsorb to oil–water interface as well. Regarding the wetting-based theory, there is no lower limit of particle size (Eqs. (2.3-6) and (2.3-7)). Indeed, the adsorption free energy is always much larger than the thermal energy, even when the solid particles are very small. As example, the adsorption free energy of spherical solid nanoparticles of 10 nm diameter at the hydrocarbon-water interface ($\gamma_{o-w} = 50 mN m^{-1}$) having a contact angle of 90° is $\Delta_{ads}E = 1.6 \times 10^{-17}\, J$, which is much larger than kT ($4 \times 10^{-21}\, J \; at \; 293\, K$). [84]

2.3.3 Particles that stabilize Pickering Emulsions

The partial wetting condition is satisfied by many types of particles, either inorganic or organic, for most common oils. A range of particles including carbon black, silica, polystyrene, iron oxide, bentonite clay, and graphene oxide [88]–[95] have been employed for emulsion formation. Determining the final characteristics of the emulsion, the particle properties play useful roles [85]. Functional particles bring

about supplementary properties; as examples, thermosensitive poly(N-isopropylacrylamide) particles give temperature-sensitivity to the emulsions [89]–[93], and pH-sensitive emulsions have been prepared with the help of pH-responsive particles [85], [94], [95]. In this study we are using surface modified para-amino benzoic acid (PABA)-terminated CB particles in suspension to form the Pickering emulsions. These particles initially are nicely suspended in water but can meet the partial wetting condition when the pH is shifted under 3.3 by becoming more hydrophobic. [85]

2.3.4 Stabilization of emulsions by adsorbed particles

Destabilization of emulsions occurs in two successive steps: coagulation and coalescence. The surface coating by solid particles mainly acts against coalescence. The adsorbed layer of solid particles forms a rigid coating around the liquid droplets that has been compared to an egg shell. Saha et al. (2013) [85] confirmed this behavior for the CB particles used in this study. They found that with a concentration as low as 0.015% w/w CB the oil-water interface consists of closely packed particle aggregates forming multiple layers. Reorganization of surface materials required for liquid droplets to merge is prevented by mechanical barrier that prevents coalescence. The mechanical strength of the particles layer comes from aggregation of solid particles at the droplet surface. This phenomenon was also reported by Saha et al. (2013) [85]. Solid particles are held together at the oil–water interface by means of attractive interactions which are required for building up the rigid layer of solid particles. In particular capillary forces are specific to particles adsorbed at the liquid-liquid interface. All types of interactions between adsorbed particles influence the stability of

Pickering emulsions: dispersion, electrostatic… Even for interactions that are not specifically interfacial, the presence of the oil–water interface influences their contribution to the overall interactions. [84]

Solid particles may also control coagulation. As example, adsorbed charged particles give rise to obvious electrostatic repulsions between the oil droplets of an o/w emulsion in the same way as ionic emulsifiers do. A series of papers by Abend and Lagaly reports the formation of particles networks between droplets keep them apart and prevent coagulation by means of either a steric repulsion mechanism or by thickening the continuous phase of the emulsion. [96]–[100]

2.3.5 Effects of excess particles and consequences on rheology

In general the required amount for a full coverage of the oil droplets is far below 1%. Since the usual concentrations of emulsifier used in the fabrication of o/w emulsions are in the range 0.1–1%, there is always excess emulsifier remaining in the aqueous phase. This residual concentration of emulsifier is required in order to ensure equilibrium adsorption to the droplets surface. In the case of Pickering emulsions, full adsorption of the solid particles is possible because of the high affinity for the interface under partial wetting. [84]

Only a small interfacial area can be stabilized, when only a low amount of solid particles is used. This should result in very large droplets. A mild emulsification process (vortex mixing) allows the formation of stable emulsions [101], [102]. Depending on the introduced shear to the emulsion, the droplets become smaller and smaller. These droplets undergo coalescence once the mixing process is stopped. Coalescence may be terminated when the interfacial area reaches the area

corresponding to full coverage by the particles [101], [103]. Full emulsification can only be reached, if the emulsion remains stable during this process. Otherwise free oil is released and the dispersion process ends with a partial emulsification of the oil [104]. Theoretically, the higher the amount of solid particles is, the smaller droplets should be able to be prepared. However, an efficient emulsification process is required. When the emulsification process is not powerful enough for creating the full interfacial area that the solid particles can cover, only part of the solid particles is adsorbed and the remaining is left as a suspension in the dispersing phase. As a summary, the emulsification of o/w Pickering emulsions takes place under three distinct regimes depending on the solid particle to oil mass ratio, $M(particles)/M(oil)$ (Figure 2-16). [84]

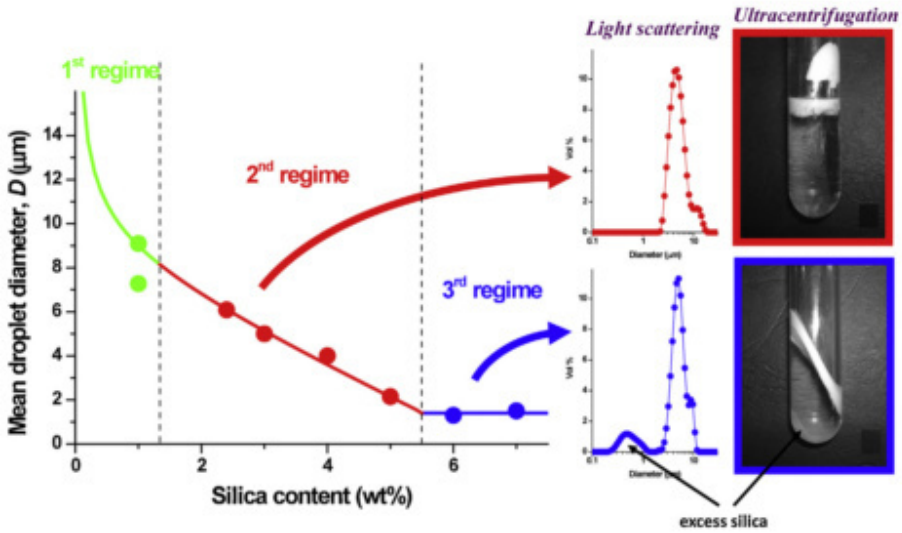

Figure 2-16. Three regimes of emulsion formation depending on the particle concentration at constant oil content.[105]

Indeed, there is no residual solid particle in the aqueous phase in the second regime where the droplet size depends on the concentration of stabilizing particles. Excess particles present in the aqueous phase in the third regime often cause

thickening of the emulsion. Indeed the solid particles that can undergo partial wetting by water and oil have a partly hydrophobic surface and consequently tend to aggregate in water. The hydrophobic fumed silica particles that are often used for the stabilization of Pickering emulsions are taken among the grades commercially supplied as thickening agents [106]. Thickening emulsions is important regarding the end use properties for practical applications. It is also advantageous because a high viscosity slows down all destabilization phenomena. Thickening contributes to the stabilization of emulsions. In the extreme case where the emulsion is gelled, the stability along a long-term storage is excellent.

Upon mixing two types of particles that undergo heterocoagulation, Abend and Lagaly built a percolating network of flocculated solid particles that were partly adsorbed to the oil droplets of an o/w Pickering emulsion [96], [97], [99], [100]. Gelation of the aqueous phase prevented the coagulation and most other events leading to de-stabilization quite efficiently. That thickening increases the stability of emulsions is a well-known fact; it holds for Pickering emulsions as well [98]. Emulsion gels can be prepared on the same grounds [107]. Interestingly, the flocculation of residual solid particles can be adjusted by physicochemical parameters in order to control the viscosity of the emulsion. As example, hydrophobic silica particles have a natural tendency to aggregation; but silica particles are stabilized by electrostatic repulsive forces coming from the negative charge of the ionized residual silanol groups. Addition of electrolytes weakens electrostatic repulsions, thus causing supplementary aggregation and increasing the viscosity [108]. Above an electrolyte concentration threshold ($2 \times 10{-}4$ mol $L{-}1$ NaCl), the flow behavior of the emulsion

dramatically changed: a strong increase of viscosity occurred, a yield stress appeared, and elasticity came up (the elastic modulus G' increased as a function of the ionic strength above the threshold). The consequence was a much slower creaming. The fluid o/w emulsion at ionic strength below the threshold contained oil droplets stabilized by adsorbed solid particles and excess solid particles dispersed in the aqueous phase. The thick emulsion at high ionic strengths no longer contain free solid particle since they are all aggregated together with oil droplets. Thickening should provide supplementary stabilization of oil droplets; this phenomenon was not observed because the emulsion was efficiently stabilized against coalescence by adsorbed solid particles, even in its fluid state. Strong thickening and appearance of elastic behavior makes the emulsion become a gel (Figure 2-17). Flow is possible however when the applied shear stress overcomes the yield stress and the network is broken by the shear. A careful choice of the ionic strength controls of the yield stress, and allows maintaining the workability of the emulsion with respect to its practical applications. However since the network of flocculated solid particle stabilizes the emulsion, breaking the gel by shearing above the yield stress may cause coalescence of the emulsion [109].

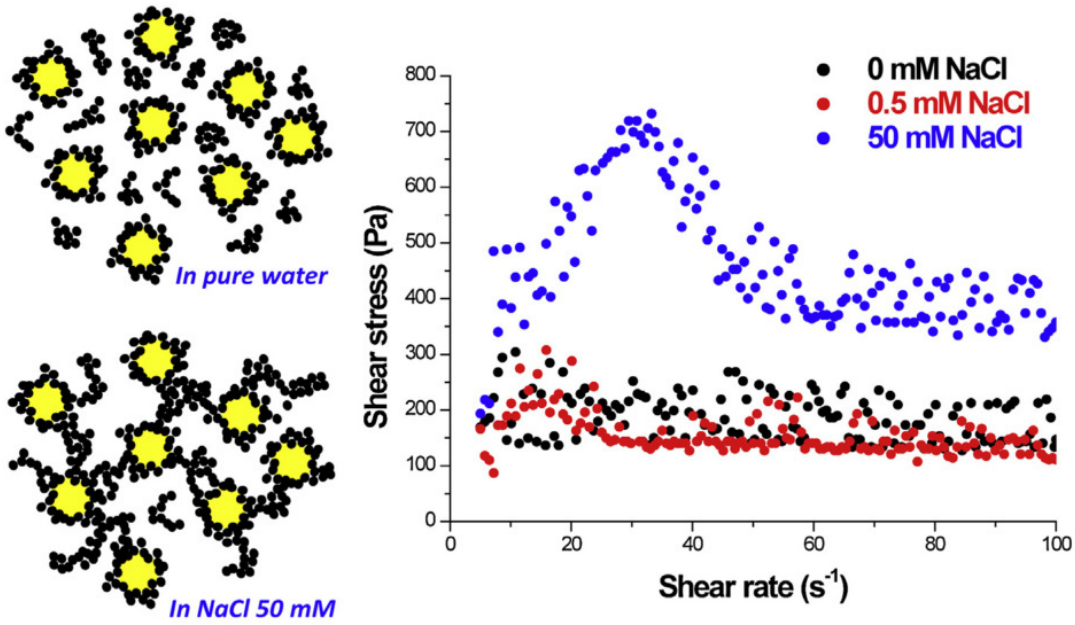

Figure 2-17. The yield stress increases as a function of the concentration of electrolyte; a stress overshoot is observed at the highest NaCl concentration (50 mM). The presumed structures of the silica particles are drawn on the left side: the yield stress comes from a percolating network of aggregated silica particles (black dots) and oil droplets (yellow circles) throughout the whole aqueous phase.

2.4 Rheology

2.4.1 Rheological Measurements and Properties

2.4.1.1 Steady-State Shear Viscosity

In each geometry, the steady shear rate imposed on the fluid depends on a driving velocity and the dimensions of the geometry. For the sliding-plate device, the shear rate $\dot{\gamma}$ is the velocity V of the moving plate (the other plate is being held stationary), divided by the gap h between the two plates; hence $\dot{\gamma} = V/h$. In the cone-and-plate geometry, $\dot{\gamma} = \Omega/\tan\alpha$, where Ω is the steady angular rotation speed of the cone or plate and α is the cone angle, which is usually less or equal to about 0.1 radians. [110]

The shear stress σ is the force that a flowing liquid exerts on a surface, per unit area of that surface, in the direction parallel to the flow. The shear viscosity η is then defined as

$$\eta = \frac{\sigma}{\dot{\gamma}} \tag{2.4-1}$$

After a steady shearing flow has been imposed on a fluid for a suitable period of time, the shear stress often comes to a steady state, $\sigma(\dot{\gamma})$, which depends on the imposed shear rate $\dot{\gamma}$. The ratio of the steady shear stress σ the shear rate $\dot{\gamma}$ is then the steady-state shear viscosity $\eta(\dot{\gamma})$.

2.4.1.2 Transient Shear Viscosity

If the stress reaches a steady value only after a transient period of steady shearing starting from a state of rest, then the instantaneous stress $\sigma(\dot{\gamma}, t)$ during the

transient start-up period, divided by the steady shear rate $\dot{\gamma}$, is the transient start-up viscosity

$$\eta^{+}(\dot{\gamma}, t) = \frac{\sigma(\dot{\gamma}, t)}{\dot{\gamma}} \tag{2.4-2}$$

The superscript '+' indicates, that the shear rate was increased from zero at time t=0. This definition is only meaningful if the fluid at time $t = 0$ is in a well-defined state, usually a stress-free state and if this starting state and the transient viscosity are reproducible from one run to the next. The superscript '+' is sometimes omitted. Measurements of $\eta^{+}(\dot{\gamma}, t)$ give information about rates of structural rearrangement within a deforming complex fluid.

The creep test is a related way of obtaining time-depending rheological information. In it, a constant shear stress is imposed on the material, and the shear rate is measured as a function of time until a steady shear rate is obtained. The creep test is especially useful for measuring the yield stress σ_y, since if the imposed stress is below σ_y the steady-state shear rate will be zero.

2.4.1.3 Storage and Loss Moduli

Another way to explore rates of structural rearrangement within a complex fluid, one that does not significantly deform the fluid's microstructure, is to impose small-amplitude oscillatory shearing. This kind of deformation can be achieved in a cone-plate geometry by rotating the cone about its axis with an angular velocity that oscillates sinusoidally, $\Omega(t) = \Omega_0 \cos(\omega t)$, where ω is the frequency of oscillation, in units of radians per second. The shear rate is then also a sinusoidal function of time, $\dot{\gamma}(t) = \Omega/\tan\alpha = \Omega_0 \cos(\omega t) / \tan\alpha$, and so is the shear strain γ, which is the time

integral of the shear rate, $\gamma = (\Omega_0/\omega)\sin(\omega t) / \tan\alpha$. The ratio (Ω_0/ω) is the amplitude of the angular deflection of the cone, and $\gamma_0 = (\Omega_0/\omega) / \tan\alpha$ is the strain amplitude of the displacement of the sliding plate, divided by the gap.

If the strain amplitude γ_0 is small enough (typically $\gamma_0 \ll 1$) that the fluid structure is not much distributed by the deformation, then the stress measured during the oscillatory deformation is controlled by the rates of spontaneous rearrangements or relaxation present in the fluid in the quiescent or equilibrium state. The shear stress $\sigma(t)$ produced by a small-amplitude deformation is proportional to the amplitude of the applied strain γ_0 and is itself sinusoidally varying in time. The maxima and minima of the sinusoidally varying stress signal are not necessarily coincident with the maxima and minima in the strain. In general, the sinusoidally varying stress can be represented as

$$\sigma(t) = \gamma_0[G'(\omega)\sin(\omega t) + G''(\omega)\cos(\omega t)] \tag{2.4-3}$$

The term proportional to $G'(\omega)$ is in phase with the strain and is called the storage modulus, while the term containing $G''(\omega)$ is in phase with the rate of strain $\dot{\gamma}$ and is called the loss modulus. The storage modulus represents storage of elastic energy, while the loss modulus represents the viscous dissipation of that energy. The ratio G''/G', which is called the loss tangent $\tan\delta$, is high ($\gg 1$) for materials that are liquid-like, but is low ($\ll 1$) for materials that are solid-like. The regime of small amplitude straining, in which the stress can be represented by Equation (2.4-3), is called the linear viscoelastic regime.

2.4.1.4 Types of Rheological Response

Differences between solid-like and liquid-like complex fluids show up in all three of the shearing measurements discussed thus far: the shear start-up viscosity $\eta^+(\dot{\gamma}, t)$, the steady-state viscosity $\eta(\dot{\gamma})$, and the linear viscoelastic moduli $G'(\omega)$ and $G''(\omega)$. The start-up stresses of $\sigma = \dot{\gamma}\eta^+(\gamma, \dot{t})$ of prototypical 'liquid-like' and 'solid-like' complex fluids are depiced in Figure 2-18. For the 'liquid-like' fluid the viscosity instantaneously reaches a steady-state value after a inception of shear, while for the 'solid-like' fluid the stress grows lineary with strain up to a critical shear strain, above which the material 'yields' or flows at constant shear stress.

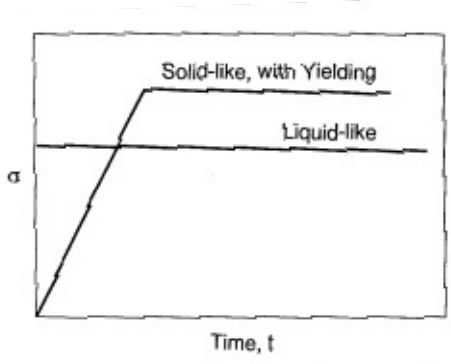

Figure 2-18. Illustration of transient shear stress $\sigma(t)$ for 'liquid-like' and 'solid-like' materials.

Figure 2-19 shows schematic curves of the steady-state shear stress and shear viscosity versus shear rate for 'solid-like' and 'liquid-like' complex fluids. For a 'solid-like' complex fluid, the steady-state shear stress is independent of shear rate (Figure 2-19a), and so the shear viscosity decreases with increasing shear rate as $\eta(\dot{\gamma}) \propto \dot{\gamma}^{-1}$. A decreasing shear viscosity with increasing shear rate is referred to as shear thinning. For the 'liquid-like' complex fluid, there is no shear thinning, the viscosity is a constant (Figure 2-19b). This means that the shear stress increases linearly with shear rate, $\sigma(\dot{\gamma}) \propto \dot{\gamma}$.

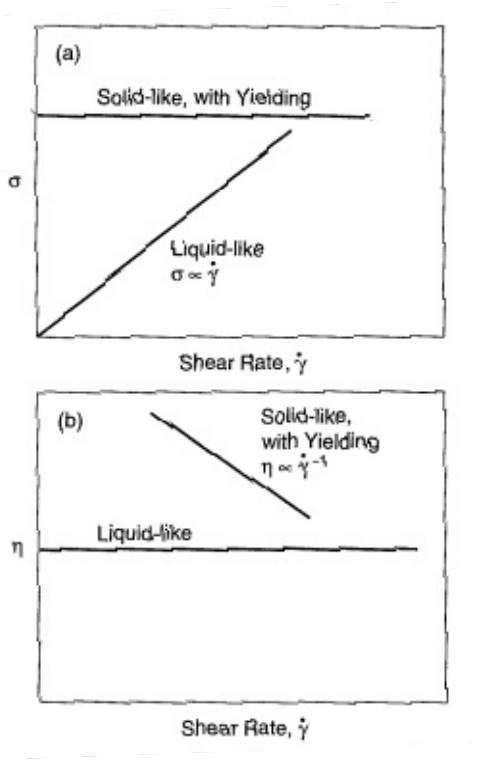

Figure 2-19. Illustrations of shear-rate-dependent (a) shear stress $\sigma(\dot{\gamma})$ and (b) shear viscosity $\eta(\dot{\gamma}) = \sigma/\dot{\gamma}$ for prototypical 'liquid-like' and 'solid-like' materials

The storage and loss moduli G' and G'' for our prototypical 'liquid-like' and 'solid-like' fluids are shown in Figure 2-20. For the 'liquid-like' fluid, the storage modulus is much lower than the loss modulus, and it scales with frequency $G' \propto \omega^2$, the loss modulus is linear in frequency, $G'' \propto \omega$. The low-frequency 'liquid-like' region in which G' and G'' obey these power laws is called terminal region. For the 'solid-like' fluid, $G' \gg G''$, and G' is nearly frequency independent.

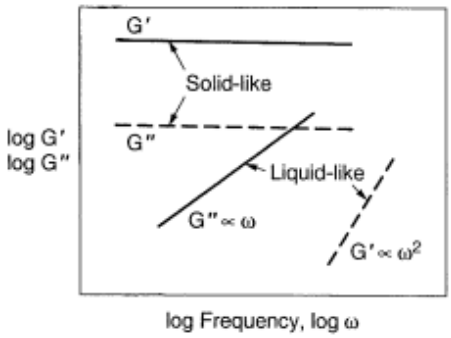

Figure 2-20. Illustrations of frequency-dependent storage and loss moduli G' and G'' for prototypical 'liquid-like' and 'solid-like' materials

2.4.2 Rheology of Particulate Gels

In 'Sol-Gel' processes a liquid suspension, or 'sol', of colloidal particles is 'gelled', or flocculated, into a quasi-solid mass by addition of a chemical agent [111]. For an initially stable sol composed of colloidal particles, the gelling agent, which is usually a pH modifier, an electrolyte, or a polymer, produces gelation by reducing repulsive particle-particle interactions, so that attractive van der Waals forces can draw particles into near contact. If the particle concentration is high enough, a sample-spanning network of such contacts forms, producing a solid-like gel phase.

A way to produce a sol phase is to use particles whose surfaces in solution are charged, resulting in electrostatic stabilization of the sol. Addition of acid or an acid former then tends to neutralize these groups, like hydroxylic or carboxylic groups, producing gelation.

Rheological measurements on concentrated, strongly flocculated gels are hampered by the following difficulties [112]–[114]:

1. Poor reproducibility
2. Sensitivity to gel preparation
3. Sensitivity to shear history
4. Extremely limited range of linear viscoelastic response
5. Slip

The first three of these difficulties arise because of the nonequilibrium structure of strongly flocculated gels. Particles bound strongly together in their primary van der Waals potential minima are unable to rearrange within laboratory time scales; hence the structures cannot relax to achieve thermodynamic equilibrium. Therefore, the gel structure depends on preparation history, including any deformation experienced by the gel prior to the rheological measurement.

2.4.2.1 The Rheology of Strongly Flocculated Gels

A strongly flocculated dispersion can be considered when the particle concentration is high enough to produce a rigid gel network. Once particle-particel contacts are formed, they are released so infrequently that particle rearrangements are strongly suppressed. Thus, the time for equilibration of the structure, given by a relaxation time τ, is too long to occur within the experimental time frame, which is usually no more than several hours. The 'Newtonian' zero-shear viscosity is only attained at shear rates $\dot{\gamma} \leq \tau^{-1}$, and these rates are too low to be accessed. Thus, strongly flocculated gels are characterized by a yield stress, rather than a zero-shear viscosity. Other rheological quantities that are important for strongly flocculated gels

include compactive strength, linear (and nonlinear) elastic moduli at high and low frequencies, and the shear-rate-dependent viscosity. The dependencies of these on particle size, particle concentration, and particle-particle interaction are important for the processing of colloidal gels.

Rheological measurements are difficult on strongly gelled colloids, and data often do not reproduce well. Multiple runs often must be averaged together to reduce data scatter. Strongly flocculated suspensions are by definition not at equilibrium, and so their properties are sensitive to preparation technique and deformation history. In addition, in large-deformation or continuous shearing, slipping of the gel against the surfaces of the rheometer tools is always a danger. [113], [115], [116]

The volume fraction dependence of the high-frequency modulus G_∞ above the minimum particle concentration is expected to behave like $G_\infty \propto \left(\phi - \phi_g\right)^n$ [117]–[119]. However, over most of the range of ϕ, G_∞ increase with ϕ roughly as [114], [120]

$$G_\infty \propto \phi^\mu \tag{2.4-4}$$

A similar result is obtained for the yield stress in shear σ_y, except the exponent is smaller, $\sigma_y \propto \Phi^m$. Such power laws have been derived from theories that model the gel as a network of interconnected fractal clusters [121]–[123].

The modulus of strongly flocculated gels tends to be highly strain-dependent, with linear behavior confined to very low strain amplitudes [121]. As flocculation becomes stronger, the strain sensitivity increases. In addition, strongly flocculated gels are likely to be more brittle than weakly flocculated ones, in that they are harder than

weakly flocculated gels, they cannot be deformed as much without fracturing [124]. This finding is if considerable importance for the processing of gel bodies.

Thus, the mechanical properties of a gel depend not only on particle radius a and concentration ϕ, but also on the flocculation strength. For gels in aqueous media, the mechanical properties therefore depend on the charge on the particle surfaces, as well as on the type of ions that might be bound to them. By adding acids or bases the pH is adjusted, which change the surface charge of the particles, presumably through surface binding of H^+ or OH^-. The yield stress σ_y is maximized at the isoelectric point.

2.4.2.2 Yield Stress and Elastic Modulus

Developing accurate theories for strongly flocculated gels is challenging, since the structures of such gels are not at thermodynamic equilibrium. It might be able to assume that such gels are in a state of static equilibrium in which the forces acting on each particle are in balance. Since the interaction potential between particles in a strongly flocculated gel has a minimum $W_{min} = W(D_0)$ that is deep compared to k_BT, gaps between neighboring particle surfaces in such gels will presumably almost be close to D_0, unless the gel is subjected to a mechanical strain. Therefore, the shape of the potential $W(D)$ near D_0 is important in determining the gel's mechanical properties.

Sensitivity to the shape of $W(D)$ differentiates weakly from strongly interacting particles. For weakly flocculated gels, the precise shape of the potential is not important. But insensitivity to the shape of the potential can only be expected when the particles are only weakly bound by that potential, so that rapid, thermally

driven changes in particle-particle separation average out the details of the shape of the potential. For strongly flocculated gels, the particle-particle separation remain trapped near the minimum in the potential well, and the shape of the well near this minimum matters much more.

In a static equilibrium one can attempt to estimate the dependence of the yield stress σ_y and the modulus G on the shape and depth of the interparticle potential. For a gel subjected to a shear strain γ that homogeneously displaces particles from their position of static equilibrium. Pairs of particles are pulled apart by this strain, and separation between particle centers of mass should increase roughly by an amount γr_0, where $r_0 \equiv 2a + D_0$ is the separation between the centers of mass in the absence of strain. Hence, the imposition of a strain γ increases the gap between particle surfaces from D_0 to

$$D \approx D_0 + \gamma(2a + D_0) \tag{2.4-5}$$

If γ is small, the increased separation of particles is already large relative to the initial gap D_0. Thus the ratio the gap between particles after the strain to that before the strain is

$$\frac{\gamma r_0 + D_0}{D_0} = \frac{[\gamma(2a + D_0) + D_0]}{D_0} \approx \frac{2\gamma a}{D_0} \tag{2.4-6}$$

Since the ratio $2a/D_0$ is usually large ($\gtrsim 100$), even a strain of only 1% multiplies the gap between neighboring particles by a factor of two or more. From this, it is obvious why strongly flocculated gels, with particle-particle gaps as low as 1nm, are so strain-sensitive [120].

A force $F = -W'(D)$ with $D = D_0 + \gamma(2a + D_0)$ is produced by this increased separation between the particles, where W' is the derivative of W with respect to D. This force would restore the original interparticle spacing if the shearing stress were removed. The macroscopic stress σ is this force times the number of interparticle bonds that cross a unit area of the sample; this latter factor should scale as ϕ^2/a^2 [125]. As long as the local applied force increases with increased strain, σ increases with increasing strain, and the gel maintains its mechanical stability. But once the strain reaches the point that the slope W' of the potential is a maximum, any further strain produces a decreasing force, and the interparticle structure breaks apart. This corresponds to the point of yield. Thus, the yield strain γ_y is given by the condition that the second derivative W'' of $W(D)$ is zero; that is $W''(D_y) = 0$, where $D_y = 2\gamma_y a + (\gamma_y + 1)D_0$ is the value of D for which $W'' = 0$. Larson (1990) [126] suggested that the maximum of W' might to be expected when separation $D = D_y$ is on the order of twice D_0, the value of D at static equilibrium.

The yield stress is proportional to $F_{max} = W'_{max} = W'(D_y)$ times the number ot interparticle bonds that cross a unit area of the sample, ϕ^2/a^2 thus

$$\sigma_y \sim \frac{\phi^2}{a^2} W'(D_y) \tag{2.4-7}$$

Larson (1990) [126] suggested that W' can be estimated as $-W_{min}/D_0$ at the yield point. Considering only van der Waals interactions and electrostatic interactions with a constant surface charge, the equation for W_{min} is the following

$$W_{min} \approx -\frac{aA_H}{12D_0} + C\zeta^2 a \tag{2.4-8}$$

where

$$C \equiv 2\pi\epsilon_0\epsilon \ln\left[\frac{1}{1-exp(-\kappa D_0)}\right] \tag{2.4-9}$$

Hence from these equations we obtain

$$\sigma_y \sim \frac{\phi^2}{a^2}\left(\frac{aA_H}{12D_0^2} + \frac{C}{D_0}\zeta^2\right) \tag{2.4-10}$$

The linear modulus G can be estimated by analogously[125]. G is defined as the stress divided by the strain γ, where γ is small enough that G is independent of γ. As argued above, the stress σ is given by roughly $(\phi^2/a^2)W'(D)$, with D given by Equation (2.4-5)). If the quantity σ/γ is to be independent of strain, then γ must be small enough that W' can be linearized in D.

$$W'(D) \approx W''(D_0)(D - D_0) \approx W''(D_0)2a\gamma \tag{2.4-11}$$

Since $G \sim (\phi^2/a^2)W'/\gamma$

$$G \sim \frac{2\phi^2}{a}W''(D_0) \tag{2.4-12}$$

Thus, the linear modulus is controlled by the curvature of the particle-particle potential W at its minimum. This local curvature is extremely sensitive to the details of the particle-particle interactions at close separations [127]. Larson (1990) [126] estimates $W''(D_0) \approx -W_{min}(D_0)/D_0^2$, so Equation (2.4-8) combined with Equation (2.4-11) and (2.4-12), gives

$$G \sim \frac{2\phi^2}{D_0^2}\left(\frac{A_H}{12D_0} - C\zeta^2\right) \tag{2.4-13}$$

The above arguments imply, that $G/\sigma_y \approx 2a/D_0$, which means, that the modulus is a couple of orders of magnitude larger than the yield stress. [120]

2.5 Gel Processing

Gels are three-dimensional networks made up of molecules, polymers, particles, colloids, etc., that are connected with each other by the specific parts on them such as functional groups and associative groups. The connected parts are called cross-links. Gels usually contain many solvent molecules inside their networks, and hence they are close to liquid in composition, but show solid-like mechanical properties due to the existence of the cross-links. [128]–[130]

The process of drying of a porous material can be divided into several stages. At first the body shrinks by an amount equal to the volume of liquid that evaporates, and the liquid-vapor interface remains at the exterior surface of the body. The second stage begins when the body becomes too stiff to shrink and the liquid recedes into the interior, leaving air-filled pores near the surface. Even as air invades the pores, a continuous liquid film supports flow to the exterior, so evaporation continues to occur from the surface of the body. Later the liquid becomes isolated into pockets and drying can proceed only by evaporation of the liquid within the body and diffusion of the vapor to the outside. To summarize, the drying stages are the following:

1. Period of constant rate drying
2. Critical Point
3. First period of falling drying rate
4. Second period of falling drying rate

As you can see in Figure 2-21 capillary tension develops as liquid flows to prevent exposure of the solid phase by evaporation, and the network is drawn back

into liquid. The network is initially so compliant that little stress is needed to keep it submerged, so the tension in the liquid is low and the radius of the meniscus r is large Figure 2-21b. As the network stiffens, the tension rises and r decreases. At the critical point, the radius of the meniscus becomes equal to the pore radius, then the constant rate period ends and the liquid recedes into the gel. [111]

In this section an overview about occurring drying stresses and appearing fractures and how to avoid them will be given.

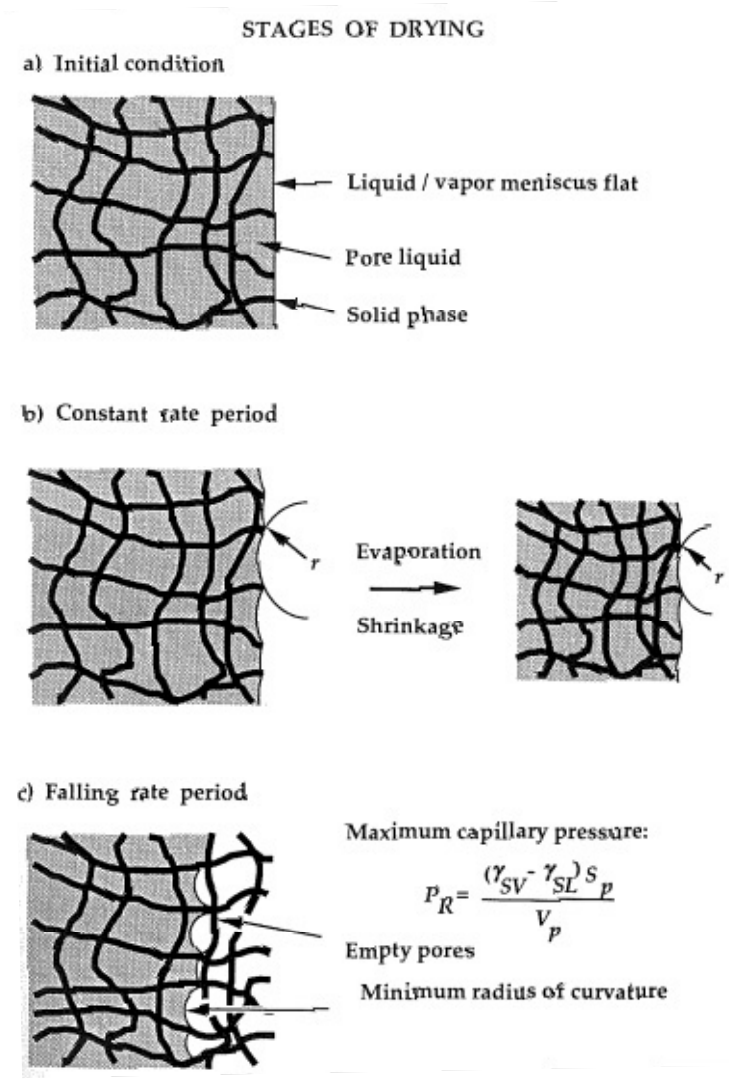

Figure 2-21. Schematic illustration of the drying process.[111]

2.5.1 Drying Stress

The reasons for drying stress to occur in the studied emulsion are a non-uniform pressure distribution and stress induced by the liquid.

2.5.1.1 Pressure distribution

The course of drying during the constant rate period is illustrated schematically in Figure 2-21. Liquid flows toward the outside to prevent exposure of the solid network. As the liquid stretches to cover the solid phase it goes into tension (concave menisci form). The tension is balanced by compressive stresses on the solid phase that tend to such the network under the surface of the liquid. The more compliant the network, the less effort has to be expended to keep it submerged, the tension in the liquid, P, rises only as high as necessary to achieve that. The radius of curvature of the meniscus is initially much larger than the pore radius. The faster the evaporation and the stiffer the network, the greater the tension in the liquid must be to pull the network under. As long as the network is sufficiently compliant, the liquid-vapor interface remains at the exterior surface of the body. However, the maximum pressure that the liquid can exert is related to the pore size of the network. The critical point is reached, when that negative pressure (P_R) cannot compress the network fast enough for the volumetric contraction rate to equal the rate of evaporation.

During the constant rate period the tension in the liquid does two things: it compresses the network and induces flow from the interior. For the meniscus to remain at the surface of the network, the rate of evaporation ($\dot{V}_E$) must equal the flux of liquid (J) to the surface, which is given by Darcy's law:

$$J_{Surface} = \frac{D}{\eta_L} \nabla P|_{Surface} = \dot{V}_E \tag{2.5-1}$$

where D is the permeability of the network and η_L is the viscosity of the liquid. The lower the permeability, the greater the pressure gradient must be to support a given evaporation rate. The reason that gels are more difficult to dry than ordinary ceramics is that the permeability of gels is very low (because of the small pore size), so modest drying rates produce very steep pressure gradients. The higher tension in the liquid near the outer surface make that portion of the network shrink faster than the body as a whole, so it tends to crack. The steeper ∇P, the greater the difference in shrinkage rate between the exterior and interior, and the more likely the gel is to fracture.

As the gel shrinks, the viscosity of the network increases and this causes an increase in P. The syneresis pressure is negligible compared to the capillary stress near the end of the constant rate period, so the tension in the liquid at the surface of the plate is

$$P(L) = \frac{K_G \dot{V}_E}{L}\left[\frac{3\alpha}{\tanh(\alpha)} - 2\right] \tag{2.5-2}$$

where K_G is the bulk viscosity of the network. The constant rate phase ends when the increasing viscosity causes $P(L)$ to rise to P_R, the maximum value of tension, when the radius of the meniscus becomes equal to that of the pore, and the liquid-vapor interface recedes into the gel.

2.5.1.2 Stress

If the pressure in the liquid were uniform, the network would be uniformly compressed and there would be no tendency to crack. However, the low permeability

of the gel gives rise to a pressure gradient, so the tension in the liquid is greater near the drying surface, and the contraction of the network is consequently greater. The difference in shrinkage rate between the inside and outside of the body is the cause of drying stress.

2.5.2 Avoiding Fracture

Drying produces a pressure gradient in the liquid phase of a gel, which leads to differential shrinkage of the network. When the exterior of the gel tries to shrink faster than the interior, tensile stresses arise that tend to fracture the network at the exterior. As shown in Figure 2-22 the material on either side of the crack can contract more freely, so it is favorable for the crack to grow into the drying surface. If the pressure in the liquid were uniform, the whole network would be isotropically compressed and the gel would shrink without risk of cracking. However the higher tension in the liquid at the exterior causes greater contraction of the network in that region. Since that contraction is inhibited by the slower-contracting interior, the network at the exterior is effectively stretched, and this promotes cracking. Thus, it is the differential contraction that produces macroscopic tension in the network and causes cracking.[111]

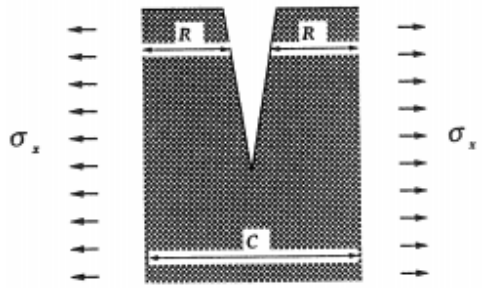

Figure 2-22. Schematic illustration of stress relief at the drying surface of a gel.

Cracking occurs when the stress in the network exceeds its strength. Fracture of brittle materials depends on the presence of flaws that amplify the stress applied to the body. [131] That is, if a uniform stress σ_x is applied to a body containing a crack with a length of c, the stress exceeds the strength of the material. The theory of linear elastic fracture mechanics (LEFM), indicates that catastrophic crack propagation when

$$\sigma_x\sqrt{\pi c} \geq K_{IC} \tag{2.5-3}$$

where K_{IC} is a material property called the critical stress intensity factor and σ_x represents the applied stress. Crack growth is called 'catastrophic', because the stress intensity increases with the size of the crack, so the bigger the crack gets, the faster it goes until it reaches the speed of sound.

The theory of LEFM applies for brittle elastic materials, whereas gels are viscoelastic, so the theory would be expected to apply only when the strain rate is too fast for significant relaxation to occur. It can be shown [132] that there is an elastic region near the tip of a moving crack whose dimension, d, is given by

$$d \sim v_c \tau_{VE} \tag{2.5-4}$$

where v_c is the velocity of the crack and τ_{VE} is the viscoelastic relaxation time. There is a zone of plastic deformation near the crack tip with a characteristic dimension of

$$d_p \sim \left(K_{IC}/\sigma_y\right)^2 \tag{2.5-5}$$

where σ_y is the yield stress. The concept of critical stress intensity is meaningful as long as $d_p \ll d$ [132]

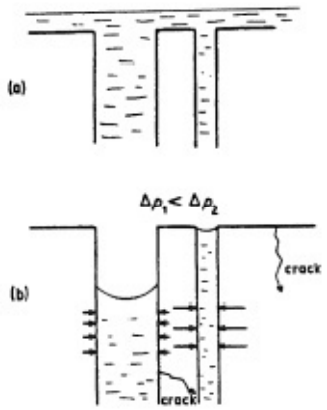

Figure 2-23. Schematic illustration of cracking resultin from draining nonuniform pores. (a) Liquid covers surface before drying starts; (b) larger pores empty first, after critical point. The higher tension in the smaller pores creates stress that cracks the 'wall' between the pores. [133]

Cracking is sometimes attributed to the existence of a pore size distribution in the gel [133], [134]. As indicated in Figure 2-23, when larger pores are emptied by evaporation, the wall between adjoining pores is subjected to uneven stress that can cause cracking. This provides a simple explanation for the observation that cracking often occurs at the critical point, as the pores begin to empty. However this does not explain, why cracking is prevented by slower evaporation. Slower drying makes the drying front more irregular on the scale of the pore size [49], so fracture would seem to be more probable at slower drying rates if uneven draining were the problem. Another difficulty with the model is that the resulting flaw would be a 'point defect' similar in size to the pore diameter, which is too small to produce a catastrophic failure. However, one could argue that these small cracks could link together as the drying front advanced until a critical flaw size was produced. That flaw would propagate catastrophically if Equation (2.5-3) were satisfied. The portion of the flaw under tension would be equal to the width of the drying front, so c in Equation (2.5-3) should be replaced with w. $\sigma_x\sqrt{w}$ increases as $(drying\ rate)^{3/4}$, so this version of the model accounts for the success of slow drying. However, it suggests that the

slowly dried body could be full of subcritical cracks. If cracks actually open up during nominally successful drying, they must heal when drying is complete.[111]

Thus there are two models for the origin of drying cracks. According to the first theory the stress rises continually until the ritical point (time t_R). If drying is slow enough that $t_R > \tau/3$, the purely viscous solution applies near the end of the period of continuous drying rate. It is unlikely that the parameter α is large at t_R, so the stress is probably given by, $\sigma_x \approx P_R L^2 \eta_L / D H_G$. The tension in the network is macroscopic and will cause catastrophic growth of pre-existing flaws of size c if Equation (2.5-3) is satisfied. The magnitude of the stress on the network is proportional to the maximum capillary stress, P_R. If this theory is correct, cracking will be reduced by slower drying, larger pores (which increases D and reduce P_R), and less viscous pore liquid (lower η_L). The other model of fracture depends on macroscopic processes. If the microcracks percolate into a macroscopic flaw, catastrophic failure will occur. The formation of microcracks results from the application of the pressure P_R across the pore wall and is not influences by drying rate. If this model is correct, successful drying requires minimizing the capillary stress and increasing the strength of the gel.

CHAPTER 3 PRELIMINARY WORK

This work is based on the preliminary work of Chen et al. (2014) [5], who studied high capacity Si/C anodes prepared using emulsion-templated direct assembly. This simple, inexpensive processing strategy is designed to overcome many of the limitations (see Section 2.2.1) that deter more widespread adoption of Si based anodes. Si nanoparticles are encased in the oil phase of an oil-in-water emulsion stabilized by carbon black (CB). These CB nanoparticles are both oil- and water-wettable. The hydrophilic/hydrophobic balance for the CB nanoparticles also causes them to form a network in the continuous aqueous phase. Upon drying this emulsion on a current collector, the CB particles located at the surface of the emulsion droplets form mesoporous cages that loosely encapsulate the Si particles that were in the oil. The CB particles that were in the aqueous phase form a conducting network connected to the CB cages. The space within the cages allows for Si particles expansion without transmitting stress to the surrounding carbon network. The increased anode conductivity provided by carbon reduces capacity fading. For this reason the anodes maintain good electrical contact with the current collect over multiple charge/discharge cycles. Good conductivity and low contact resistance also promote efficient lithiation and delithiation.[11]

3.1 Preparation of the Si/CB Anode and Cell Fabrication

Chen et al. (2014) [5] used para-aminobenzoic acid-terminated carbon black suspension in water at pH 7.5 for their study. The technique used to prepare the Si/CB anode is shown in Figure 3-1.

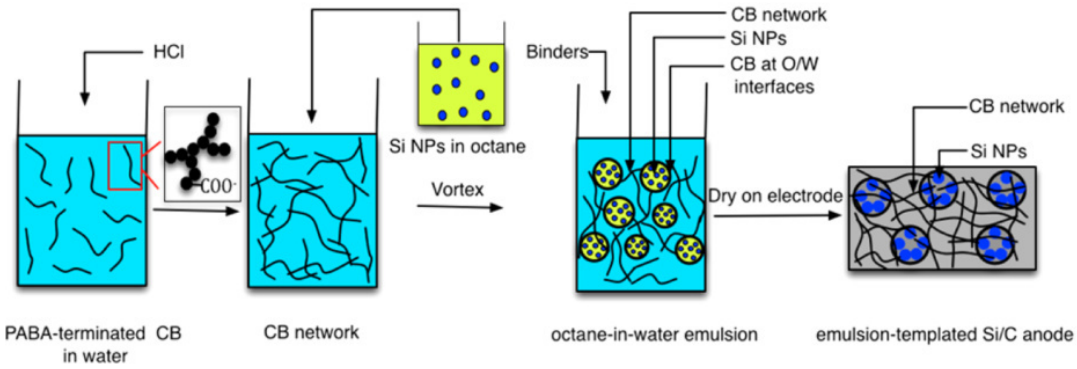

Figure 3-1. Schematic illustration of the emulsion-templated directed assembly method to prepare Si/CB anodes.[5]

1 N hydrochloric acid is added to a 1.5% w/w CB suspension to a final concentration of 0.01 N. Addition of the acid protonates some of the surface carboxylate groups on the CB and increases the hydrophobicity of the initially highly hydrophilic particles. This hydrophilic/hydrophobic balance allows CB particles to reside at the oil−water interfaces during the subsequent emulsification step. It also causes the CB to form a connected network in the aqueous phase.[85]

A 2.5% w/w suspension of Si nanoparticles in octane is mixed with the CB suspension at a ratio of 3:5 by volume. The ratio of the weights of Si nanoparticles to CB is 1:1. An aqueous solution of the binders carboxymethyl cellulose (CMC) and polyvinyl alcohol (PVA) [65], [135] at a mass ratio of 1:1 is then added to the emulsion. The volume of the CMC/PVA solution is adjusted so that the final weight of binder after drying is 10% of the total anode mass (Si + CB + binder). After another 10 min of vortexing, 0.5 mL of the emulsion is placed on a stainless steel coin cell and dried overnight in an oven at 50 °C. This gentle and uniform drying process, the elastic modulus of the CB network and the presence of the binder, minimizes cracking caused by differential or rapid shrinkage of emulsion.[136]

CR2032 type coin cells were assembled with specially designed current collector anodes and a lithium metal counter electrode. The anode loading was maintained at ~0.6 mg/cm2, for all samples, and the coated layer thickness was ~100 μm. The electrolyte was 1.2 M LiPF6 in a mixture of fluoroethylene carbonate (FEC)/ ethylmethyl carbonate (EMC) at a ratio of 3:7 v/v.

3.2 Physical Characterization

Figure 3-2A is an optical microscope image showing O/W emulsions, with an average oil droplet size, measured using image J software of 100 drops, of ~20 μm.[137] We confirmed that this was an oil-in-water emulsion by adding a drop of water and a drop of octane to the emulsion. The water spread immediately, while the octane remained as a Si on the surface. A cryo-SEM image of a droplet is shown in Figure 3-2B. The porous CB cage surrounding the drop and the SI nanoparticles in the oil are shown in the magnified images.

As a rough estimate, each 20 μm octane droplet contains on average 5×10^4 NP. Thus nearly 99% of the volume inside the emulsion drop is unoccupied. The dimensions of the region occupied by the Si NP drops change by roughly a factor of 3 after drying, still leaving adequate space for Si expansion during lithiation. We note that this method of forming emulsions cannot guarantee that each oil droplet will have the same size or contain the same number of nanoparticles. This is a stochastic process that depends upon the mixing conditions. After drying at 50 °C in an oven and examining this sample using FE-SEM, the droplet morphology is visible (Figure 3-2C). Elemental mapping using EDS, shown in Figure 3-2D, confirms that the Si

nanoparticles are confined to the 'oil' regions, and the CB particles surround these patches of Si nanoparticles.

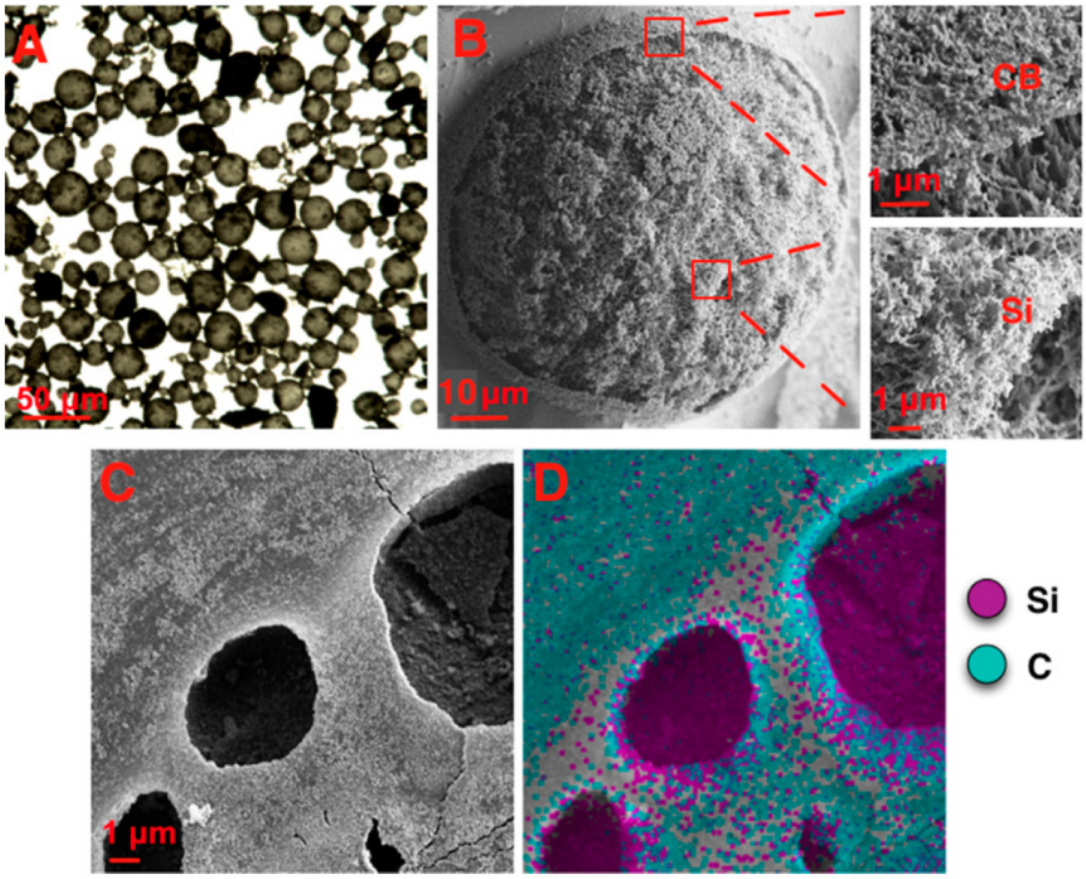

Figure 3-2. (A) A light microscope image of the Si/CB emulsion (diluted 10X with water). (B) A cryo-SEM image of the Si/CB emulsion. The magnified areas shown in the panels show CB and Si, respectively. (C) A FE-SEM image of the Si/CB electrode after drying the emulsion. (D) An EDS based elemental map of Si and C in (C). Most of the Si nanoparticles are in the regions previously occupied by octane, while the carbon is mostly confined to outside the Si-rich regions.[5]

The surfaces of the anodes before and after cycling are shown in Figure 3-3. Both the fresh Si/Super P physically mixed anode and the fresh emulsion-templated Si/CB anode look smooth with no obvious cracks (Figure 3-3A and Figure 3-3C). After 50 cycles, many cracks formed on the surface of Si/Super P physically mixed anode (Figure 3-3B) indicating that the Si particles underwent extensive volume expansion and contraction, and these stresses were transmitted to the anode. The diameter of the Si NPs measured from the SEM images is ~100 nm, twice the original

size, confirming the irreversible expansion of these particles at the end of 50 cycles. These volume changes lead to breaks of the SEI formed during the first lithiation, with concomitant exposure of fresh Si surfaces to the electrolyte, and additional SEI formation. Loss of active material, loss of electronic contact with the electrode, and persistent formation of new SEI are partly responsible for the capacity fade in the Si/ Super P anode. No surface cracks and no pulverization of the Si nanoparticles were observed in the emulsion-templated Si/CB anode after 50 cycles (Figure 3-3D). This result is consistent with the electrochemical performance. Two important advantages of the Si/CB emulsion method improved the electrochemical performance and reduced the pulverization. Since many of the silicon NPs are encapsulated by a CB 'shell', they are more protected from the electrolyte, and much of the SEI was formed on the CB. This SEI remains stable during the cycling. Additionally, the protective CB cage around the Si NP allows expansion of the Si without significant breakage of electronic contact with the current collector. We suggest that these features are responsible for the slower capacity fade in the emulsion template anode.

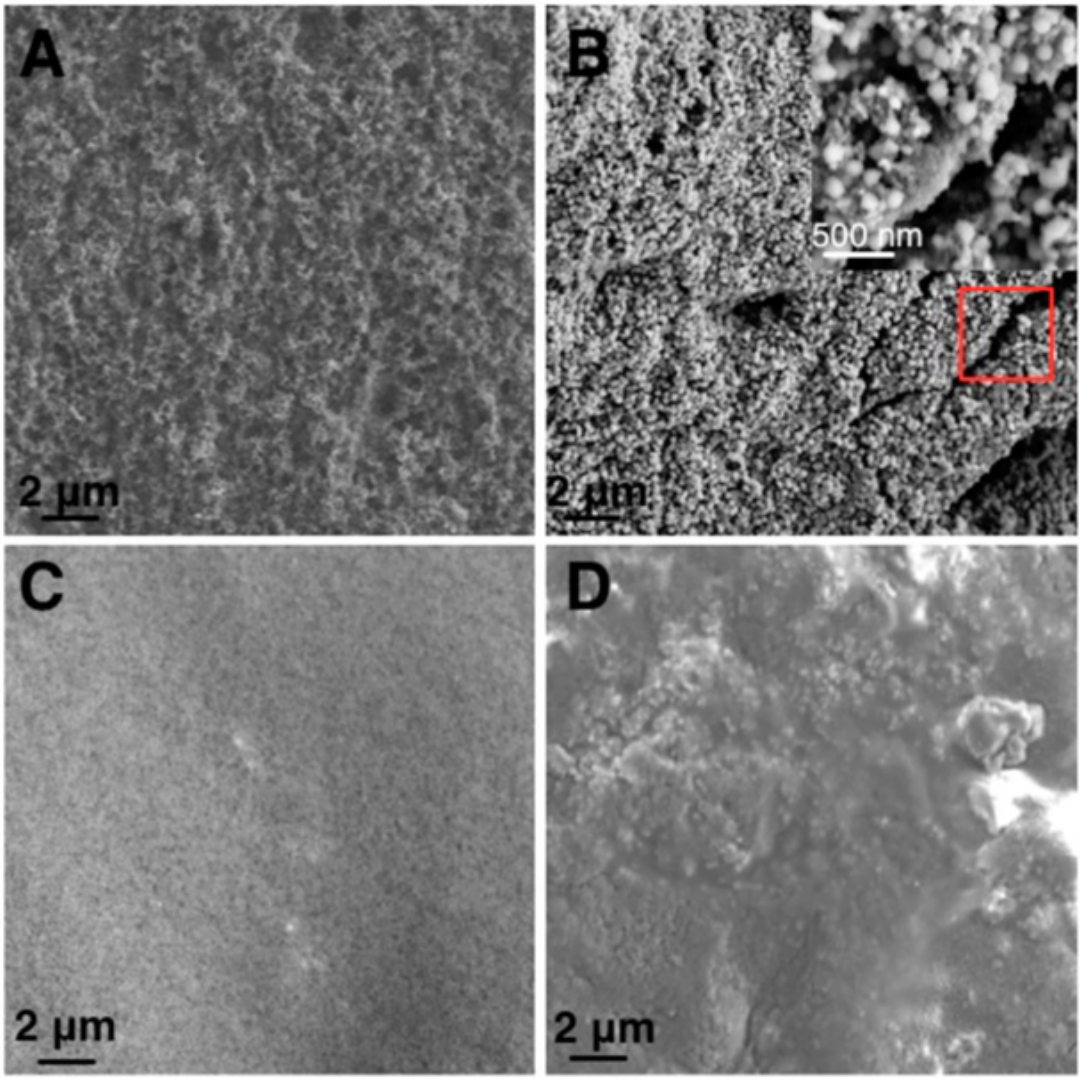

Figure 3-3. FE-SEM image of (A) fresh physically mixed Si/Super P anode. (B) The surface of the anode A after 50 cycles. The inset shows a magnified image of the region outlined. The Si NP are of the order of 100 nm, considerably expanded from their original size of 50 nm. (C) Fresh emulsion-templated Si/CB anode. (D) Emulsion-templated anode after 50 cycles. [5]

Figure 5 shows the morphology of Si NPs after cycling. As shown in Figure 3-4A, the Si NP in the Si/Super P anodes suffered severe pulverization, and lost their distinctive spherical morphology. EDS data showed a significant amount of elemental Si in the SEI layer, comparable to the Si content away from it, suggesting that some small pieces of Si broke away and remained in the SEI when Si NPs shrank during delithiation. For the emulsion-templated Si/CB anodes, the spherical shape of Si NPs

was retained, as shown in Figure 3-4B. Compared to the center of Si NP, very little Si was detected around the particles, implying that Si NPs did not suffer severe pulverization.

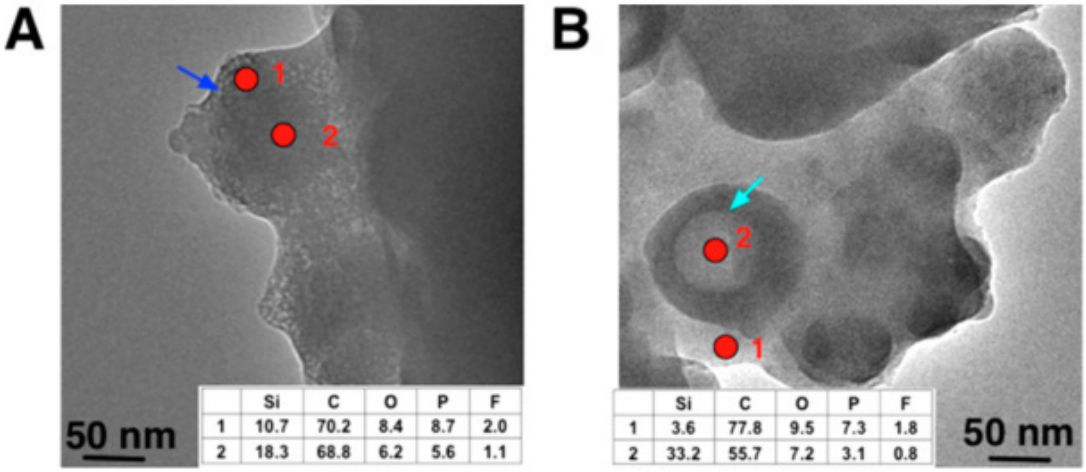

	Si	C	O	P	F
1	10.7	70.2	8.4	8.7	2.0
2	18.3	68.8	6.2	5.6	1.1

	Si	C	O	P	F
1	3.6	77.8	9.5	7.3	1.8
2	33.2	55.7	7.2	3.1	0.8

Figure 3-4. TEM images of (A) physically mixed Si/Super P anode. (B) Emulsion-templated Si/CB anode. The insets show the elemental compositions from selected areas. The dark blue arrow indicates a small piece of Si and a light blue arrow indicates the whole Si NPs.[5]

3.3 Electrical Characterization

The electrochemical cycling performance of the cells isshown in Figure 3-5. Figure 3-5A shows voltage versus capacity (all capacities are calculated based on the combined mass of Si and CB) for the Si/CB half cells at the first, fifth, 10th, and 50th cycle in the range 0.05 V to 1.5 V vs Li/Li+. The plateau in the first cycle occurs at 0.18 V, indicative of lithiation of crystalline Si. The fifth and 10th cycles display higher capacity and good charge/discharge reversibility, showing that Si lithiation is more complete, and a stable SEI had formed, by the fifth cycle. Figure 3-5B shows that the Coulombic efficiency and delithiation capacity during the first cycle are low, about 55% and ~1540 mAh/g, respectively. The low first cycle efficiency is associated with SEI formation around the CB particles, promoted by their high specific surface area, as well as SEI formation around the Si NP.31 The delithiation

capacity increased to a maximum 1940 mAh/g after five cycles, indicating that most of the Si NPs have been activated by the fifth cycle. The delithiation capacity is ~1300 mAh/g after 50 cycles. The Coulombic efficiency varied between 95% and 99% and was at 97.4% at the end of the 50th cycle. We note that at lower cycle rates, Si lithiation can be much more complete at the end of the first charging cycle. The capacity will then show a drop over the following cycles. Figure 3-5C shows capacity retention, normalized by the maximum capacity, for anodes prepared using different techniques. The emulsion-templated Si/CB anode has only slight fading after 50 cycles. The void spaces in the conductive carbon cages permit Si NP expansion and contraction without transmitting excessive stresses on the surrounding CB network, allowing the electrically conducting pathway to the current collector to be maintained. However, the bare Si anode without conductive carbon and the physically mixed Si/Super P anode show rapid fading due to attenuated electrical contact between the anode material and the current collector as the Si NPs undergo volume changes during cycling.

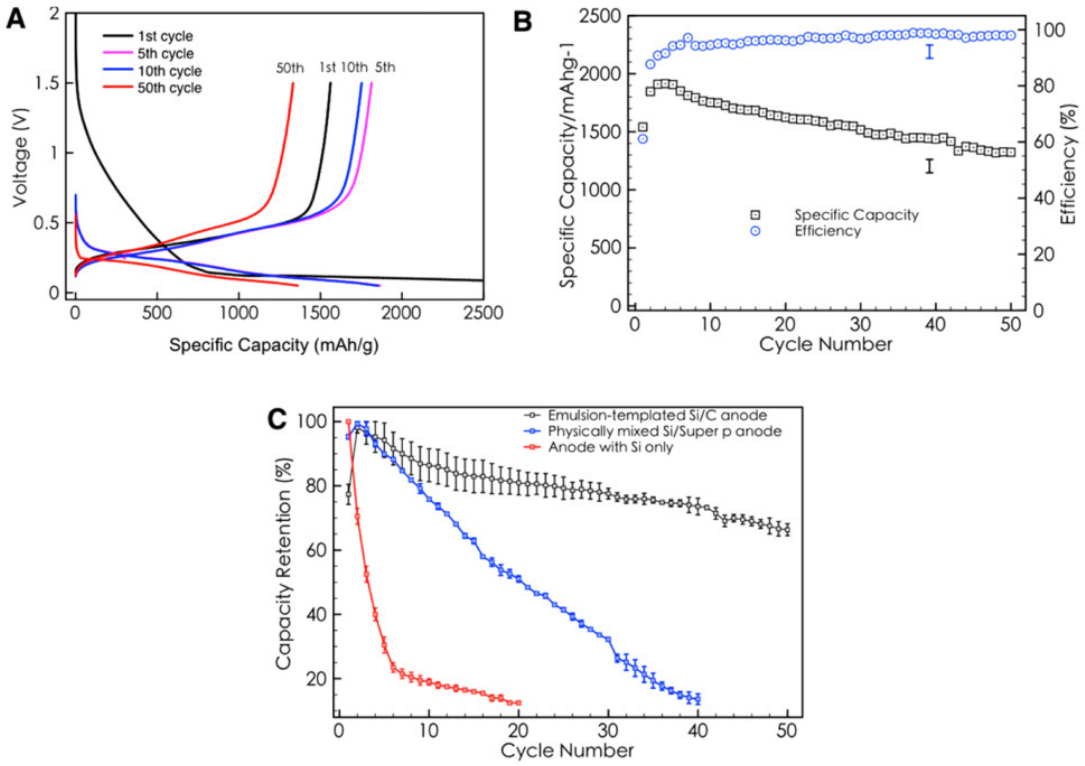

Figure 3-5. Electrochemical characterization of anodes. (A) Voltage profile for the emulsion-templated Si/CB anode during lithiation and delitiation. (B) Delithiation capacity and Coulombic efficiency of emulsion-templated Si/CB anode at a rate of C/10 (current of 1 mA/cm2). The plots represent the average from three emulsion templated anodes; the two error bars indicate the maximum spread in the data. (C) Comparison of the delithiation capacity retention of different anodes, normalized by the maximum capacity. The plots are average values, and the error bars indicate the data spread, from three samples for each type of anode. The difference in performance between these anodes is statistically significant. [5]

CHAPTER 4 MATERIALS

4.1 Silicon

Silicon nanoparticles with an average 50nm diameter (purchased by Alfa Aesar) are used as active material in the anodes. Silicon nanoparticles possess high purity, smaller particle size distribution, larger specific surface area, and lower bulk density which makes it to be a very active surfactant. Si nanoparticles are non-toxic, odorless, and with active features. The main function of the Si is to provide capacity to the anode material. As mentioned in Section 2.2 due to its high specific capacity of 4200 mAh/g in this work Si is seen as the most promising material to achive high capacity Li-ion batteries. Nanoparticles are used, because it was already shown in previous studies [64] that already the transition from micro- to nano-size particles leads to superior electrical behavior (see Section 2.2.2).

4.2 Carbon Black

Driven by their easy availability, range of surface chemistry, biocompatibility, high specific surface area, their ability to absorb organics, their classification as GRAS (generally regarded as safe) materials, and their fractal nature, the carbon particles used in this study are a commercially available grade of surface modified para-aminobenzoic acid- terminated carbon black (CB) particles suspended in water at pH 7.5. These are able to create particle-stabilized octane-in-water emulsions (see Pickering Emulsions, Section 2.3). The presence of the emulsifier particles in the aqueous phase promotes the formation of oil-in-water emulsions. The CB particles are aggregates of [107], [138] “primary” particles, each of diameter ~20 nm, fused together in a flame process. The resulting fractal particle is about 100 nm-200 nm in

nominal size and has a specific surface area of approximately 200m²/g. In this work, we take advantage of covalently linked surface groups that can be used to tune the CB hydrophilicity, to consistently form oil-in-water emulsions. The pKa of the acid is ~6.5. Thus, the carboxyl groups are deprotonated at pH 7.5

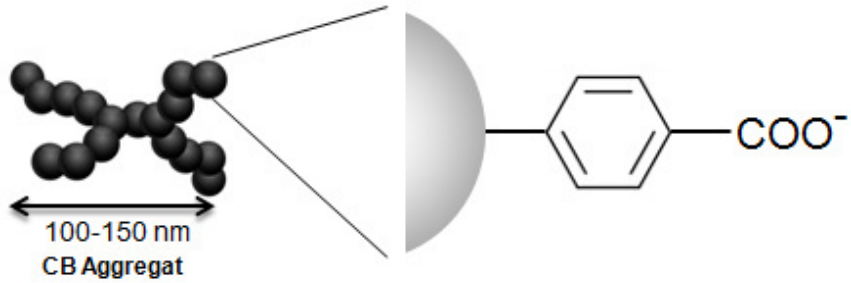

Figure 4-1. Surface modification of the used CB particles

Saha et al. (2013) [85] found that these particles can form multiple layers of CB consisting of closely packed particle aggregates at the interface. Furthermore the formed emulsions were found to be stable, as coalescence is surpressed by an increased interfacial shear viscosity produced by the presence of a connected network of particles at the surface. [85]

All these properties are beneficial for the production of the anodes. They function as the conductive backbone by forming a cross-linking network, this network gives a certain mechanical stability and due to the multiple layers of around the oil droplets, the Si gets partially protected. This should lead to a more stable SEI.

4.3 Reduced Graphene Oxide

Reduction of graphene oxide (GO) is a promising low-cost synthetic approach to bulk graphene, which offers an accessible route to transparent conducting films and flexible electronics.[139] The graphene oxide used in this study has already been reduced and was purchased from Graphene Supermarked. The specific surface area of these sheets is ~833 m^2/g and the Oxigen/Carbon ratio is 10.5. The average flake thickness is supposed to be 1 monolayer and the average size 3-5µm, however SEM pictures of the sample showed significantly larger sheets and also multiple layers (see Figure 4-2).

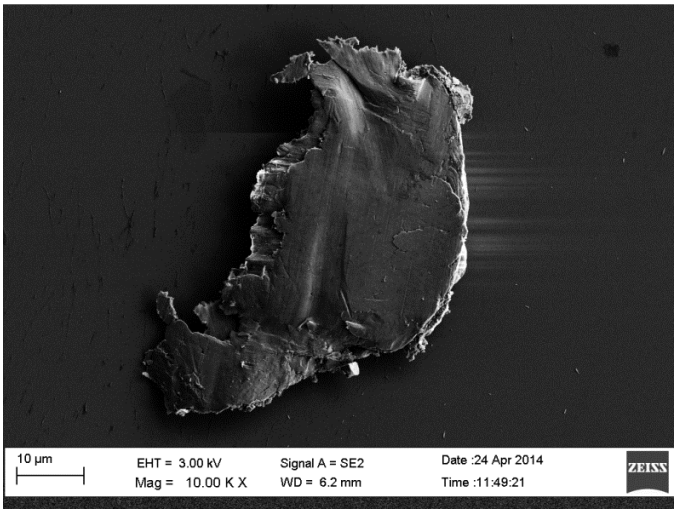

Figure 4-2. SEM image of the used reduced Graphene Oxide sheets

The conductivity of monolayer graphene mainly relies on carrier transport within the carbon plane, as a result, functional groups attached to the plane are the main influencing factor on its conductivity, while functional groups attached to the edge have less influence. Consequently, the reduction of GO must be mainly aimed at eliminating epoxy and hydroxyl groups on the plane, while other groups, e.g.

carboxyl, carbonyl and ester groups, present at the edges or defective areas only have a limited influence on the conductivity of an r-GO sheet. [140]

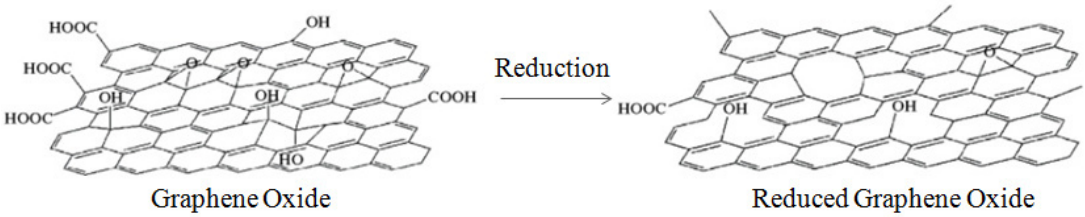

Figure 4-3. Schematic change of functional groups during the reduction of graphene oxide [139]

In this study, r-GO is used, because it can eventually further increase the conductivity of the anode material. This could lead to higher capacities and better capacity retention due to the availability of better conductive pathways.

4.4 Binder

The expansion and contraction during the charge/discharge processes of Si-based Li-ion batteries causes significant challenges in selecting the binder. Adhesion strength between active materials and current collector is a critical issue for high capacity active materials. The most conventional binder (poly(vinylidene fluoride), PVDF) used for the batteries is attached to Si particles via weak van der Waals forces only and fails to accommodate large changes in spacing between the particles. It rapidly becomes inefficient in holding the particles together and maintaining electrical conductivity within the anode, which is required for battery operation [141]–[143]. Compared with PVDF, the CMC binder shows smaller moduli, a larger maximum elongation, a stronger adhesion strength on the current collector, and much smaller solvent-absorption in organic carbonate.[144]

Mazouzi et al. (2009) [145] observed grafting esterification reaction between SiOH groups present on the surface of Si nanoparticles and C(O)OH groups of CMC when a pH 3 buffer solution is used for the electrode preparation. We propose that the protonated groups of the CMC can also interact with the CB in order to form a network. With this approach Mazouzi et al. (2009) [145] were able to produce a battery where a very remarkable cycle life (more than 700 cycles at 960 mAh/g of electrode at the C-rate) is observed. The control of the pH is necessary, because the IEP of the Si particles was found to be approximately 3.5, in agreement with Xueman et al. (2008) [146], and CMC pKa was 3.5 [147].

In this work a 1:1 mixture of CMC and PVA is used to improve the adhesion between the particles and to the current collector while also providing some elasticity

to overcome the volume changes of the silicon. By dropping the pH initially to a value of 2, we provide an acidic environment, where the carboxylic groups are getting protonated and can crosslink with the CB.

CHAPTER 5 METHODS

5.1 Processing

The samples were made by using the approach of Chen et al. (2014) [148]. 0.1 N hydrochloric acid is added to a 1.5% w/w CB suspension to a final concentration of 0.01 N. In order to achieve the goal of reducing the amount of used CB other samples made with a 0.75% w/w CB suspension and less were tested.

A 3.6% w/w suspension of Si nanoparticles in octane is mixed with the CB suspension at a ratio of 3:5 by volume for 5 min. The ratio of the weights of Si nanoparticles to CB is 1:1 and 2:1 and more with the more dilute suspension of CB. An aqueous solution of the binders CMC and PVA [65], [135] at a mass ratio of 1:1 is then added to the emulsion. The volume of the CMC/PVA solution is adjusted so that the final weight of binder after drying is 10% of the total anode mass (Si + CB + binder). After another 5 min of vortexing, 0.33 mL and accordingly 0.5 mL for the less concentrated emulsoin is placed on a stainless steel coin cell and dried in a circulating air oven. In order to study the effect of reduced Graphene Oxide, 3% and 5% of the carbon in the suspension were replaced by the r-GO.

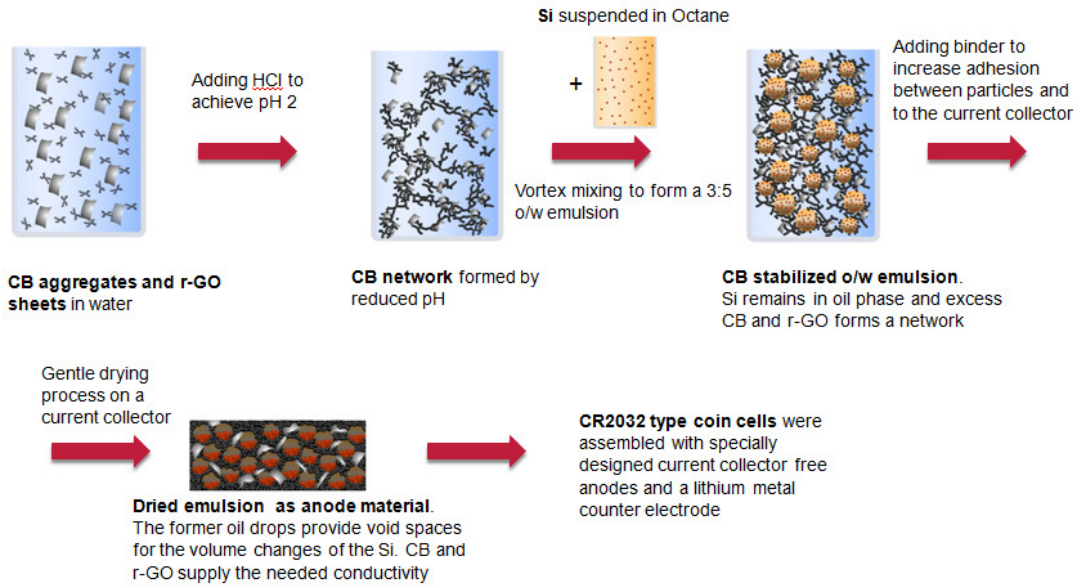

Figure 5-1. Schematic procedure of the emulsion templated anode production

Because the reduction of concentration showed significant limitations, the oil-water ratio was also changed. Without any silicon, the ability of a 1.5% w/w CB suspension to emulsify higher amounts of oil was evaluated at pH 2. Emulsions with a ratio oil-water-ratio of 1:1, 2:1, 3:1, 4:1, 5:1, 6:1 and 7:1 by volume were made by vortexmixing for 1 min. The results were evaluated using optical microscopy and the type was identified by trying to dissolve the emulsion in water and oil.

After evaluating the results, emulsions with a higher Si/C ratio were formed by using less CB suspension with the former concentration of 1.5% relative to the oil where the Si concentration was even slightly reduced.

Emulsions with a 4:1, 5:1 and 6:1 oil-water ratio by volume were produced with a 2.1% w/w Si concentration in the oil phase. This corresponds to a final weight of Si in the final anode of 72%, 75%, and 78% of the total mass (Si + CB + binder). However the procedure remained the same. 0.1 N hydrochloric acid is added to a 1.5% w/w CB suspension to a final concentration of 0.01 N. The 2.1% w/w suspension of Si

nanoparticles in octane is mixed with the CB suspension at the different ratios for 5 min. An aqueous solution of the binders CMC and PVA [65], [135] at a mass ratio of 1:1 is then added to the emulsion. The volume of the CMC/PVA solution is adjusted so that the final weight of binder after drying is 10% of the total anode mass (Si + CB + binder). In addition the PAA binder was used in the same way as the CMC/PVA binder to evaluate the expected better adhesion to the current collector.

5.2 Rheological measurements of CB suspensions

For the rheological measurements an AR 2000ex Rheometer (TA Instruments) is used. The AR2000ex design includes a unique ultra-low inertia drag cup motor and porous carbon air bearings for outstanding controlled stress, direct strain and controlled rate performance. The device is suitable for testing of viscous fluids, melts, reactive materials and solids. The porous carbon bearing results in low residual torque which allows torque control from 0.0003 µN.m to 200 mN.m with a resolution of 0.1 nN.m. The drag cup motor further reduces system friction and delivers a fast transient response and an angular velocity control range up to 300 rad/s and a displacement resolution of 40 nrad. The dynamic frequency range is between 7.5 10^{-7} and 628 rad/s. All measurements are done with a 60mm stainless steel cone-plate with a 1° cone angle. In addition a solvent trap is used to prevent evaporation.

Strain sweeps are done to define the linear viscoelastic region of the CB suspensions. After the fluid's linear viscoelastic region has been defined by a strain sweep, its structure can be further characterized using a frequency sweep at a strain below the critical strain γ_c. This provides more information about the effect of

colloidal forces, the interactions among particles. Furthermore a creep tests are used to determine the yield stress of the suspension.

The rheological measurements are all done for CB concentrations of 3%, 6%, , 9% and 12% after the addition of acid to an initial pH of 1, to make the CB particles hydrophobic and form a network.

5.3 Physical Characterization

5.3.1 Light Microscopy

The Si/CB emulsion was observed by bright-field optical microscopy in a Nikon Eclipse E 600 microscope (the sample for optical microscopy was diluted to allow adequate transmittance)

5.3.2 Scanning Electron Microscopy

An uncycled emulsion-templated Si/CB anode was observed with the Zeiss Sigma FE-SEM microscope.

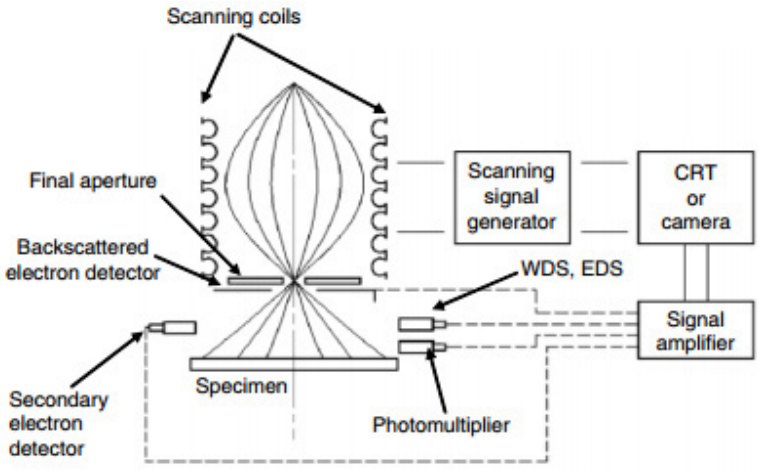

Figure 5-2. Image formation system in a typical scanning electron microscope [149]

5.3.3 Cryogenic Scanning Electron Microscopy (cryo-SEM).

Approximately 5 μL of the emulsion is placed on a cylindrical sample holder. Both are then plunged into liquid nitrogen, rapidly solidifying the emulsion. The sample is fractured with a flat-edge cold knife at −130 °C, then warmed to −95 °C for a few minutes to sublime some of the residual octane and water in a Gatan Alto 2500 cryo station attached to a Zeiss Sigma FE-SEM. Sublimation enhances surface topological details. The sample is then cooled back to −130 °C, sputtered with a gold−palladium composite, then moved from the preparation chamber to the imaging stage. The SEM is operated at 3 kV and 20 μA for imaging. The sample is maintained at −130 °C during imaging. All of the processes starting from the fracturing to the imaging take place under a high vacuum.

5.3.4 Transmission Electron Microscopy

Delithiated electrodes after 50 cycles were also characterized using a JEOL 2100 transmission electron microscope. For observation using the TEM, a small piece was taken of the electrode and dispersed it in dimethyl carbonate. A drop of the dispersion was then placed on a TEM grid and dried in a vacuum oven. The grid was stored in an argon-filled vial until it was observed. Samples were loaded rapidly into the TEM to minimize ambient exposure.

5.3.5 Energy-dispersive X-ray Spectroscopy

An uncycled emulsion-templated Si/CB anode was observed with the Zeiss Sigma FE-SEM microscope and selected area energy dispersive spectroscopy (EDS) in order to examine the spatial distribution of Si and C.

5.4 Cell Fabrication and Anode Electrochemical Characterization

CR2032 type coin cells were assembled with specially designed current collector anodes and a lithium metal working electrode (see Figure 5-3). The electrolyte was 1.2 M LiPF6 in a mixture of fluoroethylene carbonate (FEC)/ ethylmethyl carbonate (EMC) at a ratio of 3:7 v/v.

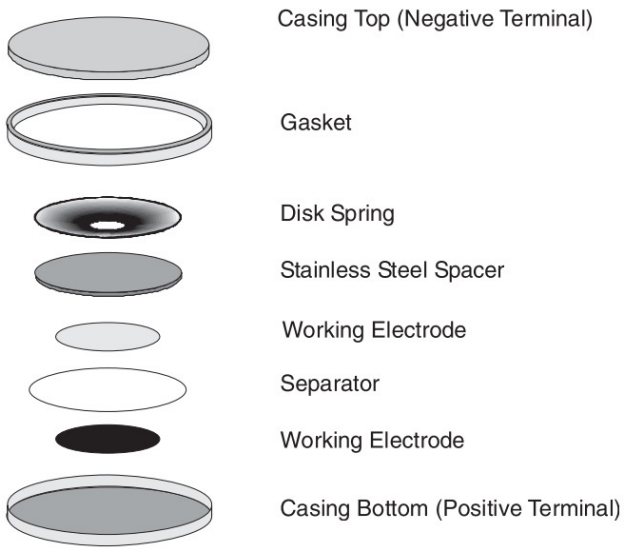

Figure 5-3. An illustration of the coin-type cell parts and assembly. [150]

An Arbin BT2000 is used for the cycling test. All half cells are subjected to galvanostatic (constant current) charge/discharge cycles with a cycling time of 10 h (C/10, current density of 1 mA/cm^2) from 0.05 V to 1.5 V versus Li/Li+ at ~25 °C, starting with the fourth cycle. The first tree cycles are used to gently establish the SEI at a cycling rate of C/25. All channels can be run completely independent allowing to test multiple independent tests simultaneously. An accuracy of up to 0.02% for low power and 0.05% for high power applications allows precise measurements of the electrical properties. After a total number of 58 cycles, the testing is stopped and the specific discharge capacity, Coulombic efficiency, and capacity retention is calculated.

CHAPTER 6 RESULTS

6.1 Processing

The formation of the emulsions was possible for concentrations of the CB suspension from 1.5% w/w down to 0.1% w/w for a 3:5 oil-water ratio without any problems to report. However a brightening of color could be observed. Being initially dominated by the black CB particles, the color becomes more and more similar to the ochre of the Si. The explanation for this are Si particles, which are no longer in the oil phase. It is likely, that some Si transverses the oil-water interface and is present in the continuous phase. Because of the large excess of black CB particles at high concentrations, the color still remains very dark. The lighter color when using less CB does not necessarily mean, that more Si leaves the oil phase, but that less CB is present as excess in the continuous phase. Using optical microscopy, the droplet diameter and the presence of excess particles could be observed.

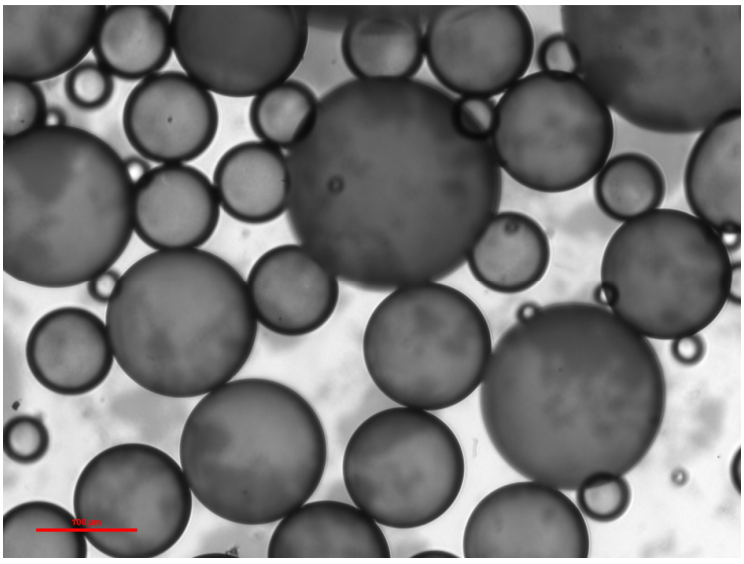

Figure 6-1. Light microscopy image of 3:5oil-water emulsion formed with a 0.1% w/w C suspension that contained 5% r-GO

The average droplet diameter was evaluated using the image processing software ImageJ analyzing more than 200 drops, and found to be ~40µm[137]. This diameter does not change for higher CB concentrations, leading to the conclusion, that the formation of the emulsion is done in the third regime (see Figure 2-16 in Section 2.3.5). That means that the oil-water interface is completely covered with CB particles and any increase in concentration only leads to more excess particles in the continuous phase. These excess particles were observed under the microscope. In Figure 6-2 agglomerates of CB and r-GO can be seen.

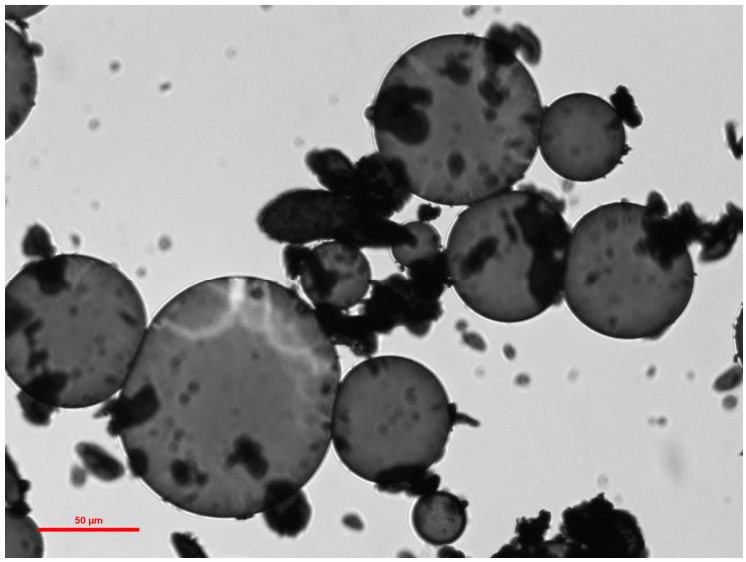

Figure 6-2. Light microscopy image of 3:5oil-water emulsion formed with a 1.5% w/w C suspension that contained 5% r-GO

So far there was no evidence that this really is an oil-water emulsion. A few drops of water disperse immediately when added to this emulsion, while drops of octane “bead” up. In addition, EDS in combination with cryo-SEM was used, where the inside of the droplets clearly showed the presence of the carbon from the octane and the continuous phase showed the oxygen of the water. These experiments confirm that we have produced octane-in-water emulsions

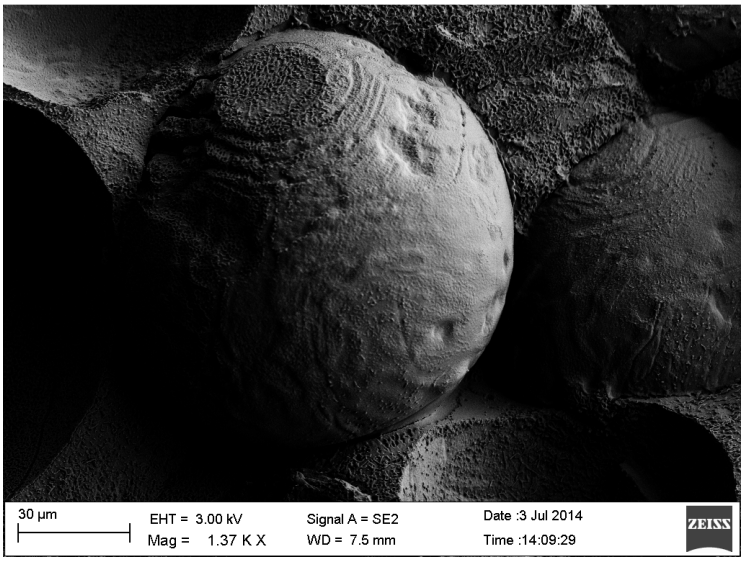

Figure 6-3. Cryo-SEM image of the emulsion

Despite the fact, that lower amounts of CB can emulsify the octane, it was only possible to dry emulsions with an initial CB concentration of at least 0.75% w/w. All other batteries showed cracking on the surface. Different drying temperatures were tried to prevent this phenomena, and as suggested in Section 2.5.2, lower temperature increased the quality of the results significantly. Finally 35°C were found to be optimal for drying, providing a slow enough evaporation speed. Nevertheless, 0.75% w/w of CB was found to be the lower limit. Figure 6-4 and Figure 6-5 show SEM images of the cracked surface of an anode. As you can see in Figure 6-4 various non-catastrophic cracks occur that do penetrate trough the whole material to the current collector. Some of these cracks were seen in all the anodes, but are not supposed to be affecting the electrical performance since the conducting network is still maintained.

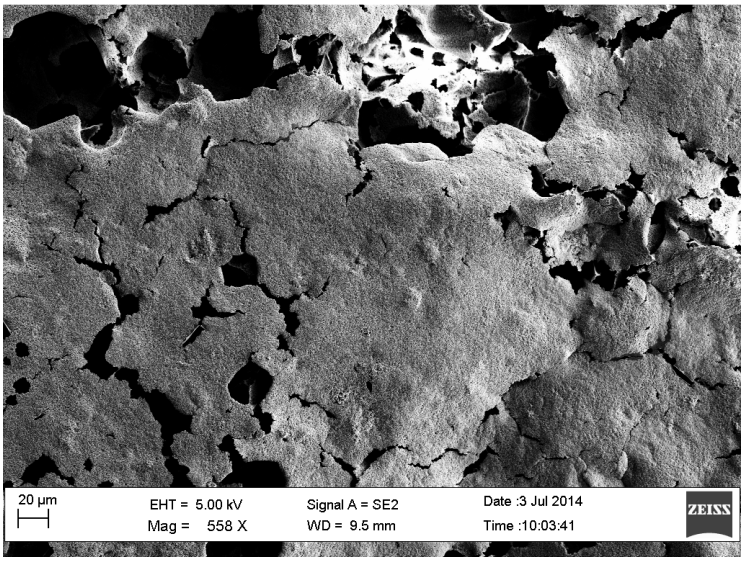

Figure 6-4. SEM image of a cracked anode surface

In Figure 6-5 a catastrophic crack cut through the anode material. This is undesired because the electrical pathway is broken, and electrolyte can penetrate into the material and might soak it. The catastrophic cracks occur when the stress in the network exceeds its strength. Being strong enough to withstand the drying stresses at concentrations of 1.5% w/w and 0.75% w/w of the CB suspension, the strength of the network becomes too weak at concentrations below. The strong dependence of the network strength and the CB concentration will be shown in Section 6.2.

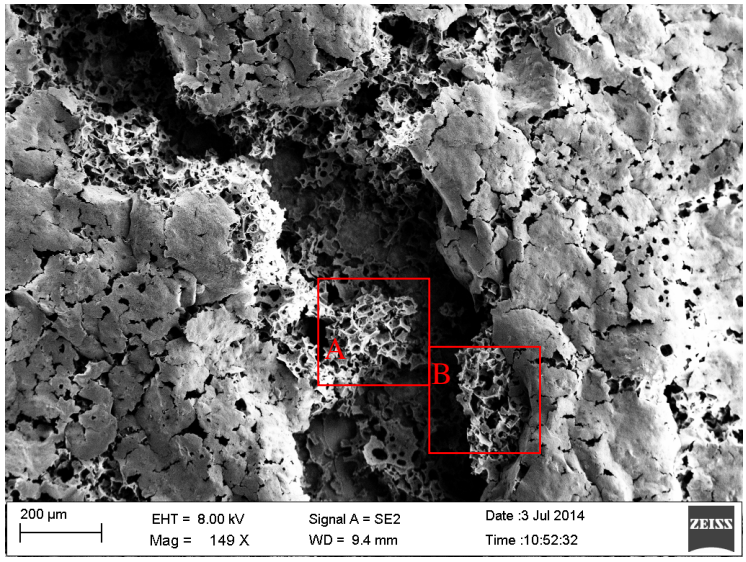

Figure 6-5. SEM image of a catastrophic crack

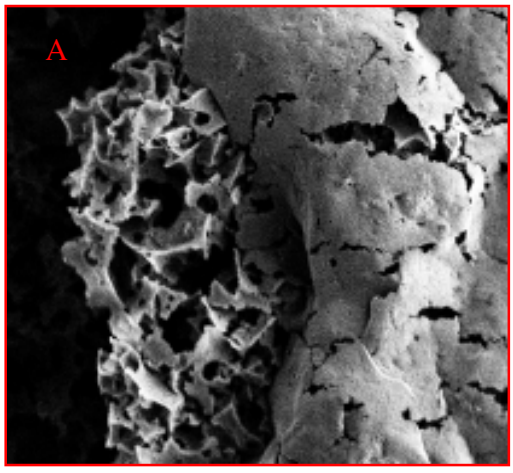

Figure 6-6.Enlarged part A of Figure 6-5

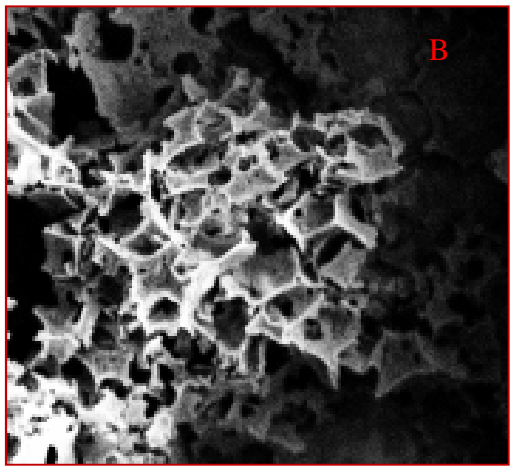

Figure 6-7. Enlarged part B of Figure 6-5

On Figure 6-6 and Figure 6-7 enlarged parts of Figure 6-5 can be seen. The remaining structure inside the catastrophic crack is shown. It shows the high porosity of the material and that the former droplets are now about 10 µm in size. This is the same size as the various round holes which can be seen on Figure 6-4 and Figure 6-5.

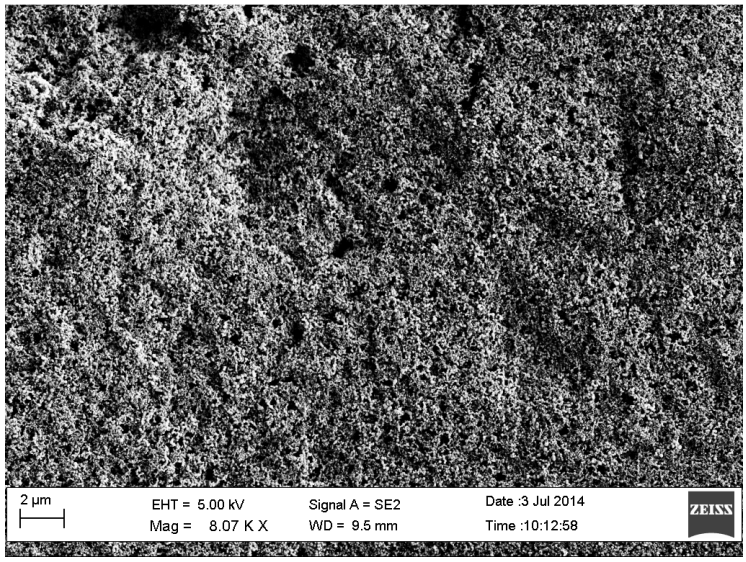

Figure 6-8. SEM picture of the rough but uniform surface of the anode

The surface of an intact anode can be descriped as rough but uniform (see Figure 6-8). The porous structure of the of the CB network is visible, however no cracks can be identified.

A closer look is giving more information about the CB particles which formed the network. Figure 6-9 shows the individual fractal CB particles, which actually seem to form bigger round aggregates of about 100 µm in diameter. These aggregates must have been originated when the pH of the CB suspension was lowered. The particles become partially hydrophobic and start to attract each other. Because at 1.5% w/w CB in the suspension, there might not be enough particles to form a network which can occupy the whole space in the water phase. As a consequence, aggregates are formed, that are able to stabilize the emulsion in the end.

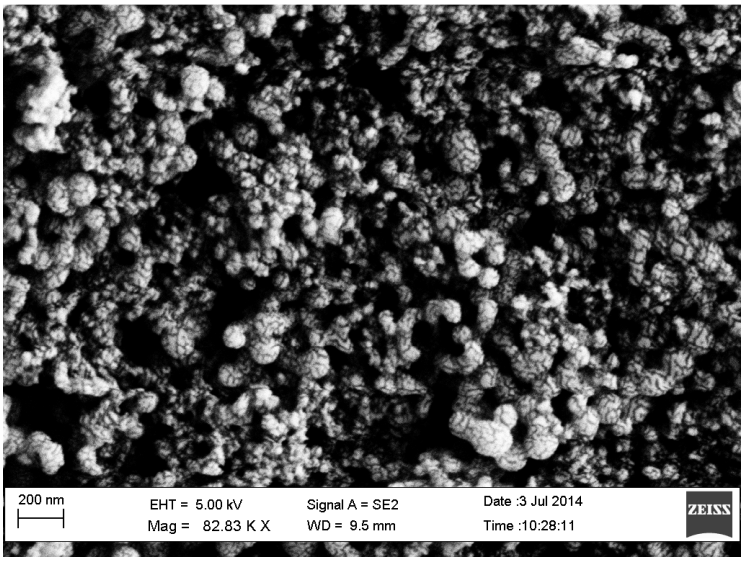

Figure 6-9. CB aggregates forming the network

Another information that can be estimated from Figure 6-9 is the pore size of the network. It is obvious, that it is in the lower nanometer range (about 1-5 nm) which is an explanation for the sensitivity of the material for cracking. Both, the water in the continuous phase but also the octane have to evaporate through those pores (see Section 2.5). Consequently the CB concentration (corresponding to the network strength) in the continuous phase is a key parameter for the processing of the Si/C anodes.

Replacing larger amounts of C by r-GO turned out to be very difficult. Still the formation of the emulsions was not causing any difficulties, but the drying performance seemed to be reduced. This lead to a maximal replacement of only 5% w/w of C. As a result, the battery with a 3% w/w replacement of C with r-GO finally consist of 1.35% r-GO by total weight, and a 5% w/w replacement of C leads to 2.25% of r-GO in the total battery mass. Cracking during the drying process prohibited the further increase of the r-GO concentration. The explanation for this might be a weaker network structure due to the lower amount of functional surface

groups on the r-GO sheets. As described in Section 4.3, in order to achieve good carrier transport within the carbon plane, functional epoxy and hydroxyl groups on the plane have to be eliminated. The r-GO used in this study has already been reduced. As a consequence, the CB particles cannot interact with the r-GO sheets in the same way they interact with each other. The attractive forces between the r-GO sheets and the CB particles are lower, and as a result the network is weakened, which leads to more cracking.

With the goal to increase the Si/C ratio more than the 2:1 that was achieved by reducing the CB concentration in the suspension, the ability of CB so stabilize emulsions with an inverse oil water ratio was evaluated. It was found that an oil-water ratio of up to 6:1, could be achieved without any excess oil or phase inversion. The absence of phase inversion was confirmed by adding a few drops of water to the emulsion, that dispersed immediately. The ratios of 4:1, 5:1 and 6:1 correspond to an 80%, 83% and 85% of oil in the emulsion. The fact, that water is still the continuous phase and oil droplets are dispersed is remarkable. An interesting observation has been, that the viscosity of these emulsions increased significantly. The gaps between the single droplets is now extremely small. The excess CB particles in the continuous phase now have to crosslink only these short distances, so there are less loose ends and similar to Figure 2-17 in Section 2.3.5 a percolating network of aggregated CB particles and oil droplets throughout the whole aqueous phase exists.

Evaluating these emulsions with light microscopy does not show any differences in the droplet size. On the other hand, the excess CB particles could not be identified either, leading to the assumption, that because of the high oil-water ratio,

most CB particles are at the oil-water interface. When forming the emulsions with Si, the coloring, described earlier in this section, was darker compared to the samples with the 3:5 o/w ratio. The reason for this might be that a less concentrated Si oil suspension, 2.1% w/w Si compared to 3.6% w/w Si, was used. I assume that this leads to less excess Si in the aqueous phase.

Drying these emulsions caused less cracking than, even with a replacement of CB by r-GO by 20%. The placement of the emulsion on the current collector was done very gently, so the formed structure could be preserved. Form this it follows that the CB network is already present instead of being formed during the drying process during the former process.

A total of 10 different batteries were prepared for cycling. four with an oil-water ratio of 3:5, splitted in two with a Si/C ratio of 1:1 and 3% w/w and 5% w/w r-GO for comparison with the result of Chen et al. (2014) [5] and two with a Si/C ratio of 2:1. For the 2:1 Si/C ratio, one battery was prepared without any r-GO and in the other 5% w/w of CB were replaced by r-GO. Furthermore, six batteries, divided in respectively two with a 4:1, 5:1, and 6:1 Si/C ratio were produced. In one of those 20% w/w CB was replaced by r-GO. Unfortunately, it was impossible to test these batteries because of the low adhesion to the current collector. The material peeled of when the electrolyte was added. To overcome this also the PAA binder was evaluated because of the superior adhesion strength reported by Magasinski et al. (2010) [76], but when adding the electrolyte the dried emulsion always came off.

6.2 Rheology

It is assumed that the CB suspension, which forms the aqueous, continuous phase in the emulsion haves like a complex fluid. Rheological measurements of the viscosity, the yield stress, the yield strain and the modulus are performed to further identify the behavior of this fluid.

Performing a flow ramp with CB suspensions of 3% w/w, 6% w/w and 12% w/w, the rheological response showed shear-thinning behavior. A zero-shear viscosity could not be attained within the measurable boundaries of the instrument. this means that the relaxation time τ of the CB network is too long because measuring the zero-shear viscosity is possible for $\dot{\gamma} \leq \tau^{-1}$. Since the lowest shear rate was 10^{-3} s^{-1} the relaxation time must be higher than 1000 s. As you can see in Figure 2-19 in Section 2.4.1.4, the behavior of the suspension is typical solid-like, since $\eta \propto \dot{\gamma}^{-1}$. However, the response of the 3% w/w CB suspension shows an slight increase of shear stress with an increasing shear rate. On the other hand this increase is not constant and seems to fluctuate. One assumption would be that the 3% w/w CB suspenstion is just below the gel point, so neither solid-like nor liquid-like behavior is fully developed. For a solid-like complex fluid, the steady-state shear stress is constant, which is the case for the 6% w/w and 12% w/w suspension for shear rates below 2 s^{-1}. From the results , shown in Figure 6-10, it can be concluded that the particle concentration that forms a sample-spanning network, and produces a solid-like gel phase is between 3% w/w and 6% w/w.

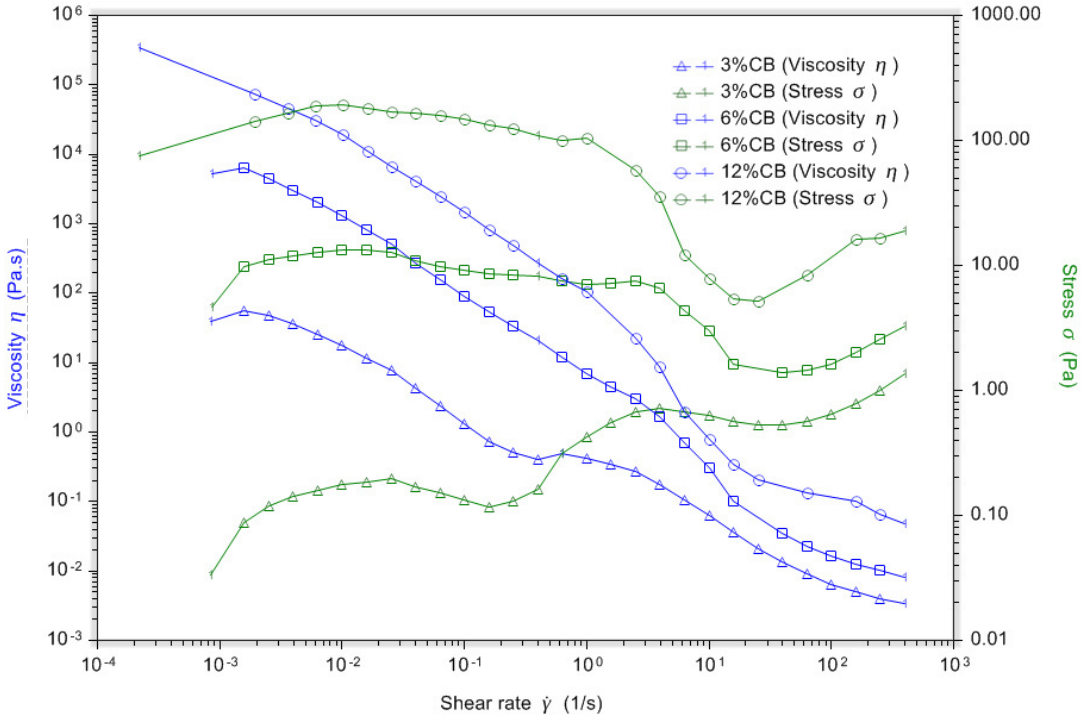

Figure 6-10. Shear rate dependent shear stress and shear viscosity for 3% w/w, 6% w/w and 12% w/w CB suspensions

CB suspensions above the gelling concentration behave like strongly flocculating gels (see Section 2.4.2). Figure 6-11 shows the dependence of the viscosity to the shear stress, which is constant until a certain yield stress in reached. Since a zero-shear viscosity cannot be measured, the CB network can be characterized by the yield stress. Performing creep tests, Figure 6-11 was developed. A yield stress of 47 Pa was measured for the 6% w/w CB suspension, and the twofold, 95 Pa, for the 9% w/w suspension.

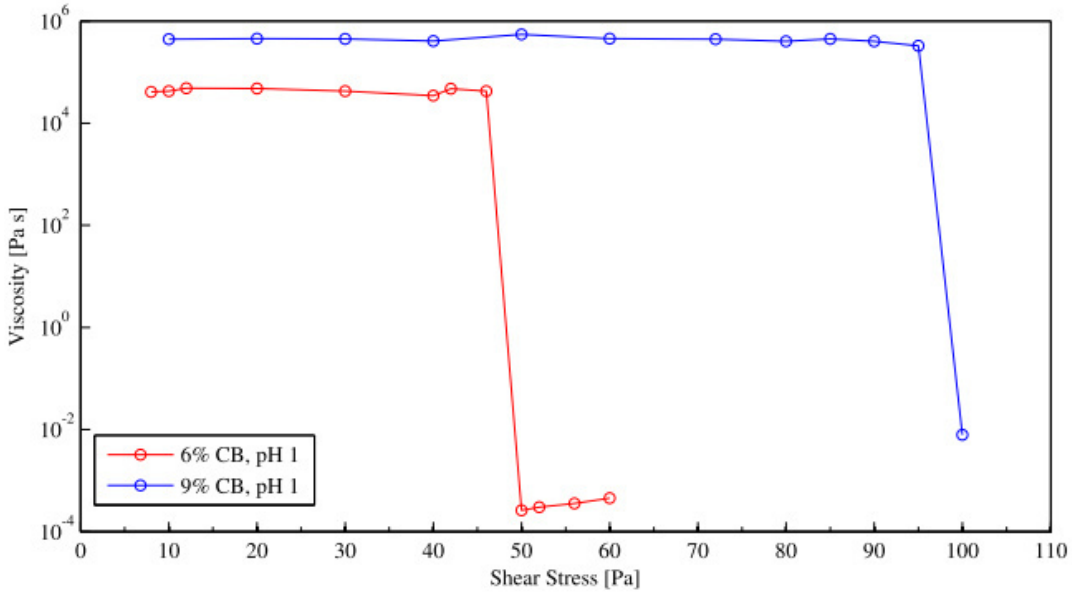

Figure 6-11. Yield stress of 6% w/w and 9% w/w CB suspensions

Performing amplitude sweeps, where the strain is successively increased, and the moduli are measured, the linear viscoelastic region was identified. The modulus of the CB gel is highly strain-dependent, with a linear behavior confined to very low strain amplitudes, as seen in Figure 6-12. All amplitude sweeps are performed with a frequency of 1 Hz. The critical strain was identified to be 0.07%. This is typical for a electrostatically stabilized system [151]. Because a linear response of the system is necessary for the frequency sweeps, the strain for these is set to 0.04% for the following tests.

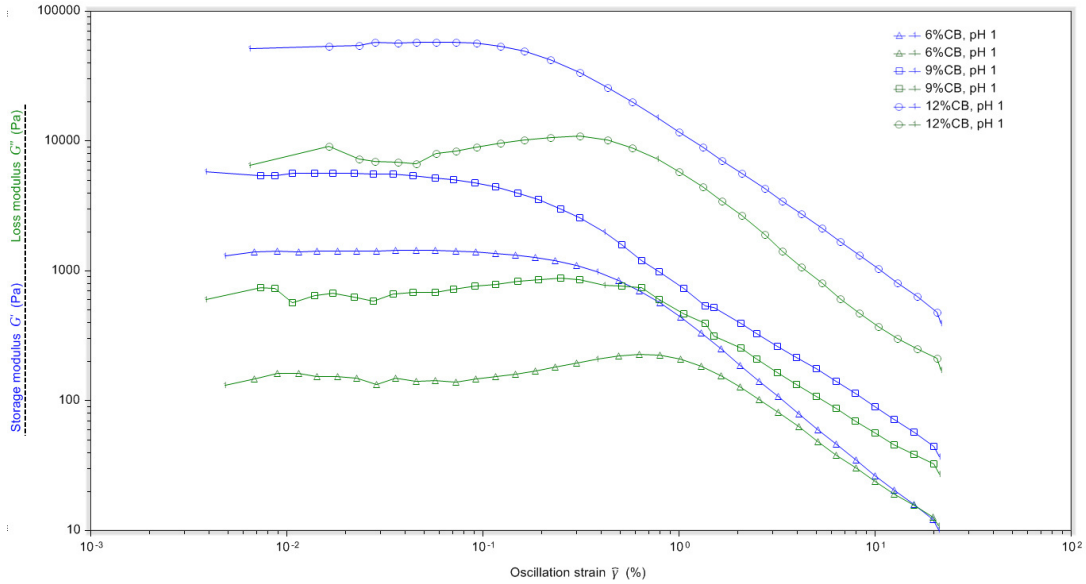

Figure 6-12. Amplitude sweep at a frequency of 1 Hz for a 6% w/w, 9% w/w and 12% w/w CB suspension

After the fluid's linear viscoelastic region has been defined by a strain sweep, its structure can be further characterized using a frequency sweep at a strain below the critical strain. This provides more information about the effect of colloidal forces, the interactions among particles. The storage and loss moduli G' and G'' for the CB suspensions are shown in Figure 2-20. For these 'solid-like' fluids, $G' \gg G''$, and G' and G'' are nearly frequency independent.

As explained in Section 2.4.2.1 the modulus G' is frequency dependent and follows the power law $G' \propto \left(\Phi - \Phi_g\right)^n$. These are volume fractions of the CB particles. With the density of 1.8 mg/cm^3 the volume fractions can easily be calculated to 0.88 % v/v, 4.5% v/v and 4.16% v/v CB for the three tested concentrations. Because the gelling point is between 3% w/w and 6% w/w, it is assumed to be in between at 4.5% w/w CB. This corresponds to a volume fraction of Φ_g=2.5% v/v CB. Using the values of G' of the first two curves, the power exponent n is found to be 2.2. With a

proportionality factor of 2650, the modulus of the 9% w/w CB suspension is predicted to be 61000 Pa which is very close to the real value of 65268 Pa.

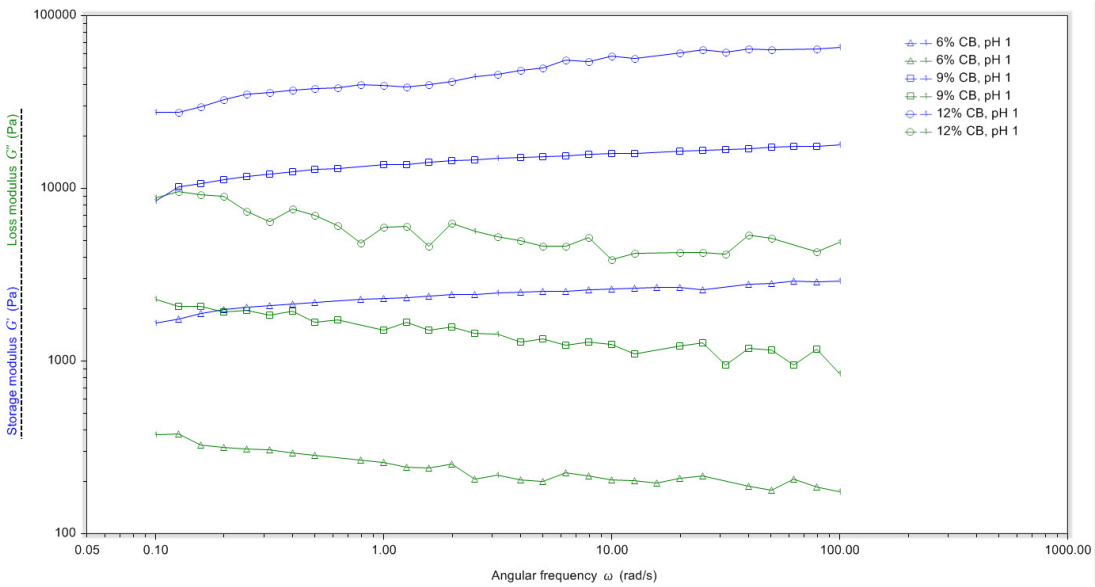

Figure 6-13. Frequency sweep at a amplitude of 0.04 % for a 6% w/w, 9% w/w and 12% w/w CB suspension

Because of their characteristics, strongly flocculated gels are likely to be more brittle than weakly flocculated ones, in that they are harder than weakly flocculated gels, they cannot be deformed as much without fracturing. [124] This could be the reason for the cracking which was observed during the drying process.

6.3 Electrical Characterization

The measured performance of the emulsion templated Si/C composite anodes with a 1:1 Si/C ratio are shown in Figure 6-14. Starting with a discharge capacity of 1827 mAh/g for the anode with 3% w/w of C replaced by r-GO and 1887 mAh/g for the one with 5% w/w. The first three cycles were used to build up the SEI very gently at a cycling rate of C/25. After the third cycle the cycling rate is change to C/10 and the capacity is much lower. It is still higher than the theoretical capacity, which might explain the rapid capacity fading till the 10^{th} cycle. There the capacity reaches a value of about ~ 1200 mAh/g and remains very stable. During the whole cycling period, this battery shows a high Coulombic efficiency above 97% with a final value of 99.5%. The only exception are the first three cycles where the SEI is build up, the Coulombic efficiency increases from 92% to 98%. The high values show evidence, that a stable SEI is formed. This is because the CB particles partially protect the Si. The former multiple layers of CB around the oil droplets are preserved over the drying process and do now cover the Si particles. After 58 cycles, the capacity is still at ~1000 mAh/g which corresponds to a capacity retention of 75% after the fourth cycle. What is remarkable about the performance is, that after the 10^{th} cycle, the capacity fading is only 85 mAh to the 58^{th} cycle. That means for these 48 cycles over 90% of the capacity is conserved. The 5% w/w r-GO anode performed slightly worse. Part of the reason might have been, that this is an average value of two cycled batteries. One of those performed worse, the other was almost identical to the 3% r-GO ones. However the characteristic is the same. The Coulombic efficiency is high, above 97% after the third cycle, and 98.5% after the 58^{th} cycle. In addition the capacity retention is almost

identical. After 58 cycles 74.6% of the capacity is maintained from the fourth cycle. Comparing the final capacity to those of the 10th cycle the retention is 84.8%. The usage of r-GO improved the performance of the batteries significantly compared to the precious work of Chen et al. (2014) [5]. They reported a delithiation capacity of ~1300 mAh/g after 50 Cycles. In this approach after 50 cycles the capacity is ~1000 mAh/g which is a decrease by more than 20%.

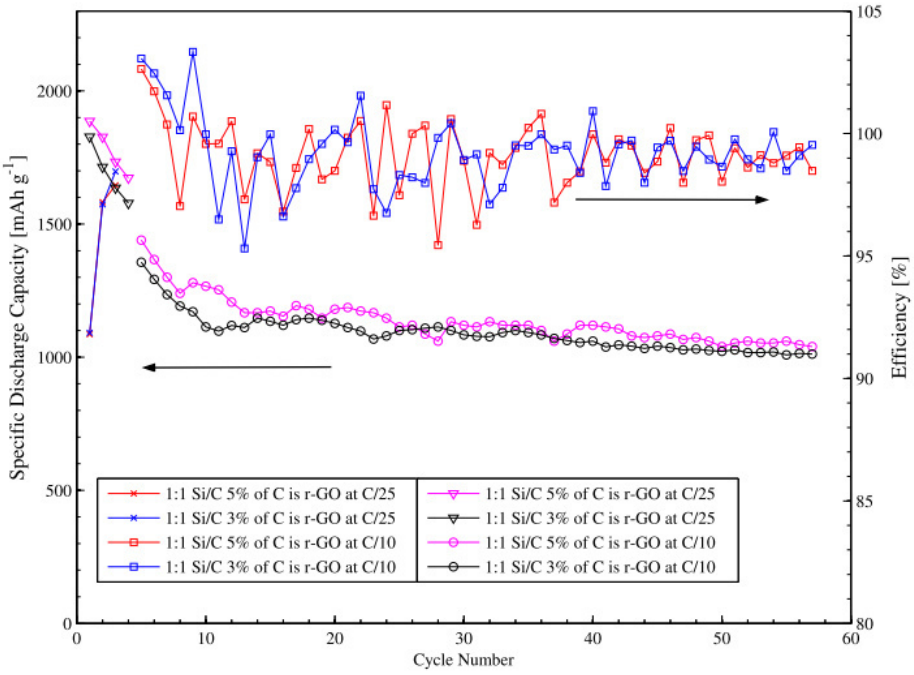

Figure 6-14. Specific discharge capacity and Coulombic efficiency of anodes with a 1:1 Si/C ratio, where 3% w/w of CB and 5% w/w have been replaced by r-GO

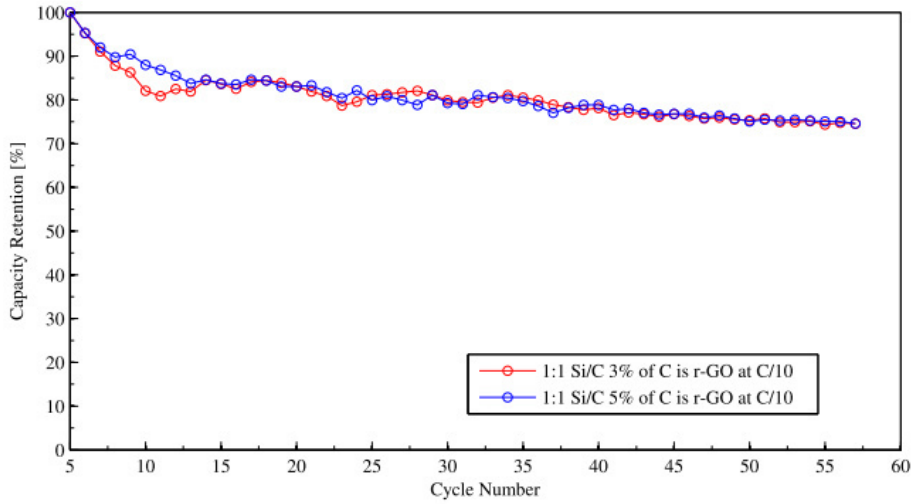

Figure 6-15. Capacity retention of anodes with a 1:1 Si/C ratio, where 3% w/w of CB and 5% w/w have been replaced by r-GO

Increasing the Si/C ration to 2:1 lead to the cycling behavior shown in Figure 6-16. One battery with r-GO and one without was cycled and compared. The gentle cycling of these anodes exhibit a really high delithiation capacity of 2252 mAh/g for the battery with r-GO, which is slightly lower than the theoretical of 2630 mAh/g. Without the r-GO the capacity was worse, only 1600 mAh/g were obtained. The Coulombic efficiency for both is almost identical, after the initial thee cycles the values only vary between 99% and 100%. As a consequence the SEI seems to be very stable, even with the reduced amount of CB. Changing the cycling rate to C/10 resulted in 1505 mAh/g for the battery with r-GO and 1150 mAh/g for the one without. After 58 cycles the capacity of the battery without r-GO is as low as 737 mAh/g, the other maintained 915 mAh/g. The capacity retention after the fourth cycle is consequently 64.1% and 60.8%.

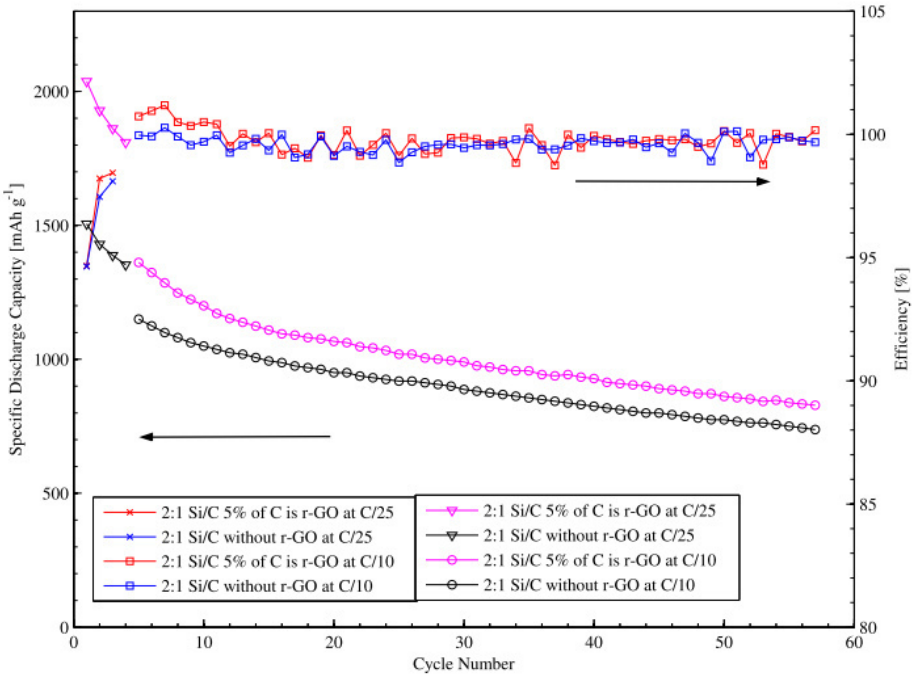

Figure 6-16. Specific discharge capacity and Coulombic efficiency of anodes with a 2:1 Si/C ratio, with a 5% w/w replacement of C with r-GO and without

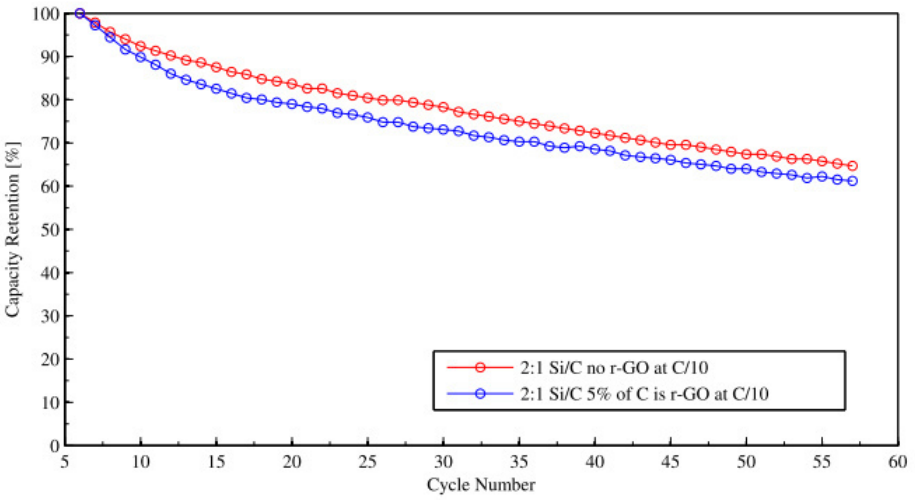

Figure 6-17. Capacity retention of anodes with a 2:1 Si/C ratio, with a 5% w/w replacement of C with r-GO and without

A comparison of the obtained results for a 1:1 Si/C and a 2:1 Si/C ration to each other, the can be seen on Figure 6-18 and Figure 6-19. The amount of r-GO is approximately the same in both anodes (5% of carbon was replaced). It is obvious, that the anode with the higher Si loading initially exhibit a much higher capacity. However, the

surperior cycling stability of the anode with a 1:1 Si/C ratio leads to a crossing point. After about 35 cycles, the capacities become equal, and after this point the capacity of the 1:1 Si/C anode exceeds those of the 2:1 Si/C anode. The capacity retention of the 1:1 Si/C battery with r-GO is much better than those of the 2:1 Si/C battery. Nonetheless, both batteries performed worse than the ones from the previous work of Chen et al. (2014)[5].

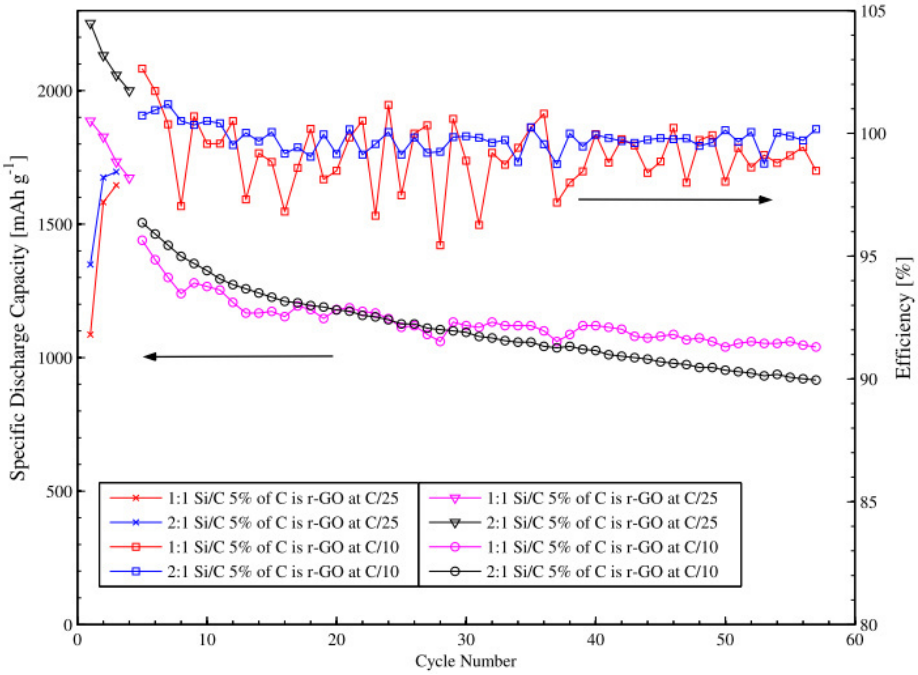

Figure 6-18 Comparison of the discharge capacity and Coulombic efficiency between 2:1, and 1:1 Si/C ratio batteries with r-GO

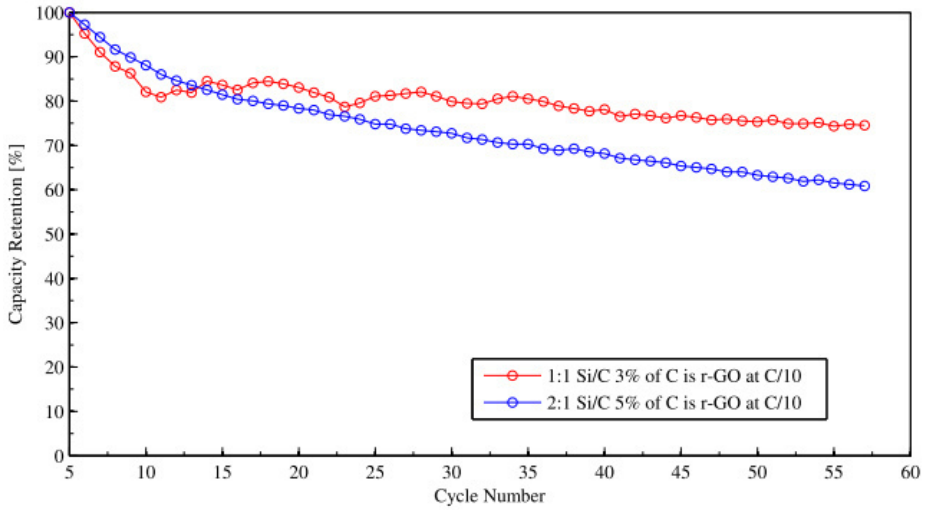

Figure 6-19. Comparison of the capacity retention between 2:1, and 1:1 Si/C ratio batteries with r-GO

CHAPTER 7 CONCLUSION

For the simple emulsion-templated directed assembly technique for forming silicon carbon composite anodes for lithium ion batteries, r-GO was introduced up to 2.25% of the total anode mass, and the Si/C ratio was increased to 2:1. The introduction of r-GO induced a better cycling stability for the 1:1 Si/C ratio. For the 2:1 Si/C ratio, also the capacity was increased significantly. However, for all the batteries the capacity was even worse than the ones with the 1:1 Si/C ratio or the previous work of Chen et al. (2014) [5]. The basic characteristics of the method are not changed, the Si nanoparticles are to regions that are surrounded by a porous CB cage and an interconnected conductive CB network. The excess volume available within the cage accommodates much of the volume changes associated with the Si particles during lithiation and delithiation, minimizing stress propagation into the conducting network. Any transmitted stresses are absorbed by the elasticity of the network. The percolation network was further identified in this study. It was shown, that the CB nanoparticles in aqueous suspension behave as a strongly flocculated gel, which cannot deform much without fracturing. Which lead to processing problems during the drying process.

However, the network maintained electronic contact with the current collector throughout the lithiation and delithiation cycles. A stable solid electrolyte interphase appears to form around the high surface area CB particles, which is indicated by a high Coulombic efficiency. The use of Si nanoparticles in a configuration that partially protects it from the electrolyte and the sustained electronic contact of the anode

material with the current collector allows all anode to have a high capacity and good cycling performance after 58 cycles.

Bibliography

[1] M. Armand and J.-M. Tarascon, “Building better batteries.,” *Nature*, vol. 451, no. 7179, pp. 652–7, Mar. 2008.

[2] P. G. Bruce, B. Scrosati, and J.-M. Tarascon, “Nanomaterials for rechargeable lithium batteries.,” *Angew. Chem. Int. Ed. Engl.*, vol. 47, no. 16, pp. 2930–46, Jan. 2008.

[3] L. Y. Beaulieu, K. W. Eberman, R. L. Turner, L. J. Krause, and J. R. Dahn, “Colossal Reversible Volume Changes in Lithium Alloys,” *Electrochem. Solid-State Lett.*, vol. 4, no. 9, p. A137, 2001.

[4] M. N. Obrovac and L. Christensen, “Structural Changes in Silicon Anodes during Lithium Insertion/Extraction,” *Electrochem. Solid-State Lett.*, vol. 7, no. 5, p. A93, 2004.

[5] Y. Chen, M. Nie, B. L. Lucht, A. Saha, P. R. Guduru, and A. Bose, “High capacity, stable silicon/carbon anodes for lithium-ion batteries prepared using emulsion-templated directed assembly.,” *ACS Appl. Mater. Interfaces*, vol. 6, no. 7, pp. 4678–83, Apr. 2014.

[6] K. Kang, Y. S. Meng, J. Bréger, C. P. Grey, and G. Ceder, “Electrodes with high power and high capacity for rechargeable lithium batteries.,” *Science*, vol. 311, no. 5763, pp. 977–80, Feb. 2006.

[7] B. Scrosati and J. Garche, “Lithium batteries: Status, prospects and future,” *J. Power Sources*, vol. 195, no. 9, pp. 2419–2430, May 2010.

[8] M. S. Whittingham, “Lithium batteries and cathode materials.,” *Chem. Rev.*, vol. 104, no. 10, pp. 4271–301, Oct. 2004.

[9] C.-X. Zu and H. Li, “Thermodynamic analysis on energy densities of batteries,” *Energy Environ. Sci.*, vol. 4, no. 8, p. 2614, 2011.

[10] J. M. Tarascon and M. Armand, “Issues and challenges facing rechargeable lithium batteries.,” *Nature*, vol. 414, no. 6861, pp. 359–67, Nov. 2001.

[11] M. L. Terranova, S. Orlanducci, E. Tamburri, V. Guglielmotti, and M. Rossi, “Si/C hybrid nanostructures for Li-ion anodes: An overview,” *J. Power Sources*, vol. 246, pp. 167–177, Jan. 2014.

[12] M. Yoshio, T. Tsumura, and N. Dimov, “Electrochemical behaviors of silicon based anode material,” *J. Power Sources*, vol. 146, no. 1–2, pp. 10–14, Aug. 2005.

[13] H. Wu and Y. Cui, “Designing nanostructured Si anodes for high energy lithium ion batteries,” *Nano Today*, vol. 7, no. 5, pp. 414–429, Oct. 2012.

[14] A. Yoshino, “The birth of the lithium-ion battery.,” *Angew. Chem. Int. Ed. Engl.*, vol. 51, no. 24, pp. 5798–800, Jun. 2012.

[15] B. Dunn, H. Kamath, and J.-M. Tarascon, “Electrical energy storage for the grid: a battery of choices.,” *Science*, vol. 334, no. 6058, pp. 928–35, Nov. 2011.

[16] O. Haas and E. J. Cairns, “Electrochemical energy storage.,” *Annu. Rep. Prog. Chem., Sect. C*, vol. 95, pp. 163–197, May 1999.

[17] A. J. Bard, R. Parsons, and J. Jordan, *Standard potentials in aqueous solution*. 1985.

[18] M. E. Wieser and T. B. Coplen, “Atomic weights of the elements 2009 (IUPAC Technical Report),” *Pure Appl. Chem.*, vol. 83, no. 2, pp. 359–396, Jan. 2010.

[19] V. Yartys, J. K. Solberg, and M. Kirkengen, “Porous Silicon as Anode Material for Li-ion Batteries Asbjørn Ulvestad,” 2013.

[20] P. Verma, P. Maire, and P. Novák, “A review of the features and analyses of the solid electrolyte interphase in Li-ion batteries,” *Electrochim. Acta*, vol. 55, no. 22, pp. 6332–6341, Sep. 2010.

[21] V. Etacheri, O. Haik, Y. Goffer, G. a Roberts, I. C. Stefan, R. Fasching, and D. Aurbach, “Effect of fluoroethylene carbonate (FEC) on the performance and surface chemistry of Si-nanowire Li-ion battery anodes.,” *Langmuir*, vol. 28, no. 1, pp. 965–76, Jan. 2012.

[22] A. Lewandowski and A. Świderska-Mocek, “Ionic liquids as electrolytes for Li-ion batteries—An overview of electrochemical studies,” *J. Power Sources*, vol. 194, no. 2, pp. 601–609, Dec. 2009.

[23] a. Manuel Stephan, “Review on gel polymer electrolytes for lithium batteries,” *Eur. Polym. J.*, vol. 42, no. 1, pp. 21–42, Jan. 2006.

[24] W. A. van Schalkwijk and B. Scrosati, *Advances in Lithium-Ion Batteries*. New York: Kluwer Academic/Plenum Publishers, 2002, p. 513.

[25] V. Etacheri, R. Marom, R. Elazari, G. Salitra, and D. Aurbach, “Challenges in the development of advanced Li-ion batteries: a review,” *Energy Environ. Sci.*, vol. 4, no. 9, p. 3243, 2011.

[26] D. Aurbach, Y. Talyosef, B. Markovsky, E. Markevich, E. Zinigrad, L. Asraf, J. S. Gnanaraj, and H.-J. Kim, “Design of electrolyte solutions for Li and Li-ion

batteries: a review," *Electrochim. Acta*, vol. 50, no. 2–3, pp. 247–254, Nov. 2004.

[27] J. S. Gnanaraj, M. D. Levi, Y. Gofer, D. Aurbach, and M. Schmidt, "LiPF[sub 3](CF[sub 2]CF[sub 3])[sub 3]: A Salt for Rechargeable Lithium Ion Batteries," *J. Electrochem. Soc.*, vol. 150, no. 4, p. A445, 2003.

[28] K. Xu, S. Zhang, T. R. Jow, W. Xu, and C. A. Angell, "LiBOB as Salt for Lithium-Ion Batteries:A Possible Solution for High Temperature Operation," *Electrochem. Solid-State Lett.*, vol. 5, no. 1, p. A26, 2002.

[29] J. W. Fergus, "Recent developments in cathode materials for lithium ion batteries," *J. Power Sources*, vol. 195, no. 4, pp. 939–954, Feb. 2010.

[30] M. Thackeray, C. T. Division, and E. T. Program, "Manganese oxides for lithium batteries," vol. 25, no. 97, pp. 3–4, 1997.

[31] M. Gaberscek, R. Dominko, and J. Jamnik, "Is small particle size more important than carbon coating? An example study on LiFePO4 cathodes," *Electrochem. commun.*, vol. 9, no. 12, pp. 2778–2783, Dec. 2007.

[32] B. C. Melot and J.-M. Tarascon, "Design and preparation of materials for advanced electrochemical storage.," *Acc. Chem. Res.*, vol. 46, no. 5, pp. 1226–38, May 2013.

[33] A. Yoshino, K. Sanechika, and T. Nakajima, "Secondary battery." Google Patents, 1987.

[34] B. Scrosati, L. Sapienza, and P. A. Moro, "Recent advances in lithium ion battery materials," vol. 45, pp. 2461–2466, 2000.

[35] A. K. Shukla and T. Prem Kumar, "Materials for next-generation lithium batteries," *Curr. Sci.*, vol. 94, no. 3, pp. 314–331, 2008.

[36] W.-J. Zhang, "A review of the electrochemical performance of alloy anodes for lithium-ion batteries," *J. Power Sources*, vol. 196, no. 1, pp. 13–24, Jan. 2011.

[37] Y. . Lee, K. . Pan, Y. . Lin, T. Prem Kumar, and G. T. . Fey, "Lithium intercalation in graphites precipitated from pig iron melts," *Mater. Chem. Phys.*, vol. 82, no. 3, pp. 750–757, Dec. 2003.

[38] U. Kasavajjula, C. Wang, and a. J. Appleby, "Nano- and bulk-silicon-based insertion anodes for lithium-ion secondary cells," *J. Power Sources*, vol. 163, no. 2, pp. 1003–1039, Jan. 2007.

[39] A. N. Dey, “Electrochemical Alloying of Lithium in Organic Electrolytes,” *J. Electrochem. Soc.*, vol. 118, no. 10, pp. 1547–1549, 1971.

[40] M. Winter and J. O. Besenhard, “Electrochemical lithiation of tin and tin-based intermetallics and composites,” *Electrochim. Acta*, vol. 45, no. 1–2, pp. 31–50, Sep. 1999.

[41] a. . Jansen, a. . Kahaian, K. . Kepler, P. . Nelson, K. Amine, D. . Dees, D. . Vissers, and M. . Thackeray, “Development of a high-power lithium-ion battery,” *J. Power Sources*, vol. 81–82, pp. 902–905, Sep. 1999.

[42] S.-H. Ng, J. Wang, D. Wexler, K. Konstantinov, Z.-P. Guo, and H.-K. Liu, “Highly reversible lithium storage in spheroidal carbon-coated silicon nanocomposites as anodes for lithium-ion batteries.,” *Angew. Chem. Int. Ed. Engl.*, vol. 45, no. 41, pp. 6896–9, Oct. 2006.

[43] R. A. Sharma and R. N. Seefurth, “Thermodynamic Properties of the Lithium-Silicon System,” pp. 19–24, 1976.

[44] B. A. Boukamp, G. C. Lesh, and R. A. Huggins, “All-Solid Lithium Electrodes with Mixed-Conductor Matrix,” *J. Electrochem. Soc.*, vol. 128, no. 4, pp. 1–5, 1981.

[45] C. van der Marel, G. J. B. Vinke, and W. van der Lugt, “The Phase Diagram of the System Lithium-Silicon,” *Solid State Commun.*, vol. 54, no. 11, pp. 917–919, 1985.

[46] J. W. Kim, J. H. Ryu, K. T. Lee, and S. M. Oh, “Improvement of silicon powder negative electrodes by copper electroless deposition for lithium secondary batteries,” *J. Power Sources*, vol. 147, no. 1–2, pp. 227–233, Sep. 2005.

[47] W. . Weydanz, M. Wohlfahrt-Mehrens, and R. . Huggins, “A room temperature study of the binary lithium–silicon and the ternary lithium–chromium–silicon system for use in rechargeable lithium batteries,” *J. Power Sources*, vol. 81–82, pp. 237–242, Sep. 1999.

[48] B. Gao, S. Sinha, L. Fleming, and O. Zhou, “Alloy Formation in Nanostructured Silicon,” *Adv. Mater.*, vol. 13, no. 11, pp. 816–819, Jun. 2001.

[49] J. H. Ryu, J. W. Kim, Y.-E. Sung, and S. M. Oh, “Failure Modes of Silicon Powder Negative Electrode in Lithium Secondary Batteries,” *Electrochem. Solid-State Lett.*, vol. 7, no. 10, p. A306, 2004.

[50] R. a. Huggins, “Lithium alloy negative electrodes,” *J. Power Sources*, vol. 81–82, pp. 13–19, Sep. 1999.

[51] H. Wu and Y. Cui, “Designing nanostructured Si anodes for high energy lithium ion batteries,” *nanotoday*, vol. 7, pp. 414–429, 2012.

[52] T. D. Hatchard and J. R. Dahn, “In Situ XRD and Electrochemical Study of the Reaction of Lithium with Amorphous Silicon,” *J. Electrochem. Soc.*, vol. 151, no. 6, p. A838, 2004.

[53] M. T. McDowell and Y. Cui, “Single Nanostructure Electrochemical Devices for Studying Electronic Properties and Structural Changes in Lithiated Si Nanowires,” *Adv. Energy Mater.*, vol. 1, no. 5, pp. 894–900, Oct. 2011.

[54] I. Ryu, J. W. Choi, Y. Cui, and W. D. Nix, “Size-dependent fracture of Si nanowire battery anodes,” *J. Mech. Phys. Solids*, vol. 59, no. 9, pp. 1717–1730, Sep. 2011.

[55] M. T. McDowell, I. Ryu, S. W. Lee, C. Wang, W. D. Nix, and Y. Cui, “Studying the kinetics of crystalline silicon nanoparticle lithiation with in situ transmission electron microscopy.,” *Adv. Mater.*, vol. 24, no. 45, pp. 6034–41, Nov. 2012.

[56] U. Maver, A. Žnidaršič, and M. Gaberšček, “An attempt to use atomic force microscopy for determination of bond type in lithium battery electrodes,” *J. Mater. Chem.*, vol. 21, no. 12, p. 4071, 2011.

[57] S. K. Soni, B. W. Sheldon, X. Xiao, M. W. Verbrugge, D. Ahn, H. Haftbaradaran, and H. Gao, “Stress Mitigation during the Lithiation of Patterned Amorphous Si Islands,” *J. Electrochem. Soc.*, vol. 159, no. 1, p. A38, 2012.

[58] K.-L. Lee, J.-Y. Jung, S.-W. Lee, H.-S. Moon, and J.-W. Park, “Electrochemical characteristics of a-Si thin film anode for Li-ion rechargeable batteries,” *J. Power Sources*, vol. 129, no. 2, pp. 270–274, Apr. 2004.

[59] M. S. Park, G. X. Wang, H. K. Liu, and S. X. Dou, “Electrochemical properties of Si thin film prepared by pulsed laser deposition for lithium ion micro-batteries,” *Electrochim. Acta*, vol. 51, no. 25, pp. 5246–5249, Jul. 2006.

[60] P. R. Raimann, N. S. Hochgatterer, C. Korepp, K. C. Möller, M. Winter, H. Schröttner, F. Hofer, and J. O. Besenhard, “Monitoring dynamics of electrode reactions in Li-ion batteries by in situ ESEM,” *Ionics (Kiel).*, vol. 12, no. 4–5, pp. 253–255, Sep. 2006.

[61] R. Ruffo, S. S. Hong, C. K. Chan, R. a. Huggins, and Y. Cui, “Impedance Analysis of Silicon Nanowire Lithium Ion Battery Anodes,” *J. Phys. Chem. C*, vol. 113, no. 26, pp. 11390–11398, Jul. 2009.

[62] C. K. Chan, R. Ruffo, S. S. Hong, and Y. Cui, “Surface chemistry and morphology of the solid electrolyte interphase on silicon nanowire lithium-ion battery anodes,” *J. Power Sources*, vol. 189, no. 2, pp. 1132–1140, Apr. 2009.

[63] X. Wu, Z. Wang, L. Chen, and X. Huang, “Ag-enhanced SEI formation on Si particles for lithium batteries,” *Electrochem. commun.*, vol. 5, no. 11, pp. 935–939, Nov. 2003.

[64] J. Graetz, C. C. Ahn, R. Yazami, and B. Fultz, “Highly Reversible Lithium Storage in Nanostructured Silicon,” *Electrochem. Solid-State Lett.*, vol. 6, no. 9, p. A194, 2003.

[65] A. Magasinski, B. Zdyrko, I. Kovalenko, B. Hertzberg, R. Burtovyy, C. F. Huebner, T. F. Fuller, I. Luzinov, and G. Yushin, “Toward efficient binders for Li-ion battery Si-based anodes: polyacrylic acid.,” *ACS Appl. Mater. Interfaces*, vol. 2, no. 11, pp. 3004–10, Nov. 2010.

[66] M. Ge, J. Rong, X. Fang, and C. Zhou, “Porous doped silicon nanowires for lithium ion battery anode with long cycle life.,” *Nano Lett.*, vol. 12, no. 5, pp. 2318–23, May 2012.

[67] C. K. Chan, H. Peng, G. Liu, K. McIlwrath, X. F. Zhang, R. a Huggins, and Y. Cui, “High-performance lithium battery anodes using silicon nanowires.,” *Nat. Nanotechnol.*, vol. 3, no. 1, pp. 31–5, Jan. 2008.

[68] L.-F. Cui, Y. Yang, C.-M. Hsu, and Y. Cui, “Carbon - Silicon Core - Shell Nanowires as High Capacity Electrode for Lithium Ion Batteries 2009,” *Nano Lett.*, vol. 9, no. Lithium Ion Batteries, pp. 1–5, 2009.

[69] M.-H. Park, M. G. Kim, J. Joo, K. Kim, J. Kim, S. Ahn, Y. Cui, and J. Cho, “Silicon nanotube battery anodes.,” *Nano Lett.*, vol. 9, no. 11, pp. 3844–7, Nov. 2009.

[70] H. Wu, G. Chan, J. W. Choi, I. Ryu, Y. Yao, M. T. McDowell, S. W. Lee, A. Jackson, Y. Yang, L. Hu, and Y. Cui, “Stable cycling of double-walled silicon nanotube battery anodes through solid-electrolyte interphase control,” *Nat Nano*, vol. 7, no. 5, pp. 310–315, May 2012.

[71] T. Takamura, S. Ohara, M. Uehara, J. Suzuki, and K. Sekine, “A vacuum deposited Si film having a Li extraction capacity over 2000 mAh/g with a long cycle life,” *J. Power Sources*, vol. 129, no. 1, pp. 96–100, Apr. 2004.

[72] B. Liu, P. Soares, C. Checkles, Y. Zhao, and G. Yu, “Three-dimensional hierarchical ternary nanostructures for high-performance Li-ion battery anodes.,” *Nano Lett.*, vol. 13, no. 7, pp. 3414–9, Jul. 2013.

[73] Y.-S. He, P. Gao, J. Chen, X. Yang, X.-Z. Liao, J. Yang, and Z.-F. Ma, “A novel bath lily-like graphene sheet-wrapped nano-Si composite as a high performance anode material for Li-ion batteries,” *RSC Adv.*, vol. 1, no. 6, p. 958, 2011.

[74] N. Liu, Z. Lu, J. Zhao, M. T. McDowell, H.-W. Lee, W. Zhao, and Y. Cui, “A pomegranate-inspired nanoscale design for large-volume-change lithium battery anodes,” *Nat. Nanotechnol.*, no. February, pp. 2–7, Feb. 2014.

[75] T. H. Hwang, Y. M. Lee, B.-S. Kong, J.-S. Seo, and J. W. Choi, “Electrospun core-shell fibers for robust silicon nanoparticle-based lithium ion battery anodes.,” *Nano Lett.*, vol. 12, no. 2, pp. 802–7, Feb. 2012.

[76] A. Magasinski, B. Zdyrko, I. Kovalenko, B. Hertzberg, R. Burtovyy, C. F. Huebner, T. F. Fuller, I. Luzinov, and G. Yushin, “Toward efficient binders for Li-ion battery Si-based anodes: polyacrylic acid.,” *ACS Appl. Mater. Interfaces*, vol. 2, no. 11, pp. 3004–10, Nov. 2010.

[77] G. Liu, S. Xun, N. Vukmirovic, X. Song, P. Olalde-Velasco, H. Zheng, V. S. Battaglia, L. Wang, and W. Yang, “Polymers with tailored electronic structure for high capacity lithium battery electrodes.,” *Adv. Mater.*, vol. 23, no. 40, pp. 4679–83, Oct. 2011.

[78] Y. Oumellal, N. Delpuech, D. Mazouzi, N. Dupré, J. Gaubicher, P. Moreau, P. Soudan, B. Lestriez, and D. Guyomard, “The failure mechanism of nano-sized Si-based negative electrodes for lithium ion batteries,” *J. Mater. Chem.*, vol. 21, no. 17, p. 6201, 2011.

[79] R. Huang, X. Fan, W. Shen, and J. Zhu, “Carbon-coated silicon nanowire array films for high-performance lithium-ion battery anodes,” *Appl. Phys. Lett.*, vol. 95, no. 13, p. 133119, 2009.

[80] N.-S. Choi, K. H. Yew, W.-U. Choi, and S.-S. Kim, “Enhanced electrochemical properties of a Si-based anode using an electrochemically active polyamide imide binder,” *J. Power Sources*, vol. 177, no. 2, pp. 590–594, Mar. 2008.

[81] R. Aveyard, B. P. Binks, and J. H. Clint, “Emulsions stabilised solely by colloidal particles,” *Adv. Colloid Interface Sci.*, vol. 100–102, pp. 503–546, Feb. 2003.

[82] B. P. B. U, “Particles as surfactants ҂ similarities and differences,” 2002.

[83] B. P. Binks, *Colloidal Particles at Liquid Interfaces*. New York: Cambridge University Press, 2006, p. 503.

[84] Y. Chevalier and M.-A. Bolzinger, “Emulsions stabilized with solid nanoparticles: Pickering emulsions,” *Colloids Surfaces A Physicochem. Eng. Asp.*, vol. 439, pp. 23–34, Dec. 2013.

[85] A. Saha, A. Nikova, P. Venkataraman, V. T. John, and A. Bose, “Oil Emulsi fi cation Using Surface-Tunable Carbon Black Particles,” *Appl. Mater. Interfaces*, vol. 5, pp. 3094–3100, 2013.

[86] D. M. Kaz, R. McGorty, M. Mani, M. P. Brenner, and V. N. Manoharan, “Physical ageing of the contact line on colloidal particles at liquid interfaces,” *Nat Mater*, vol. 11, no. 2, pp. 138–142, Feb. 2012.

[87] B. P. Binks and S. O. Lumsdon, “Influence of Particle Wettability on the Type and Stability of Surfactant-Free Emulsions †,” *Langmuir*, vol. 16, no. 23, pp. 8622–8631, Nov. 2000.

[88] P. Wongkongkatep, K. Manopwisedjaroen, P. Tiposoth, S. Archakunakorn, T. Pongtharangkul, M. Suphantharika, K. Honda, I. Hamachi, and J. Wongkongkatep, “Bacteria interface pickering emulsions stabilized by self-assembled bacteria-chitosan network.,” *Langmuir*, vol. 28, no. 13, pp. 5729–36, Apr. 2012.

[89] T. Ngai, S. H. Behrens, and H. Auweter, “Novel emulsions stabilized by pH and temperature sensitive microgels.,” *Chem. Commun. (Camb).*, no. 3, pp. 331–3, Jan. 2005.

[90] B. Brugger and W. Richtering, “Magnetic, Thermosensitive Microgels as Stimuli-Responsive Emulsifiers Allowing for Remote Control of Separability and Stability of Oil in Water-Emulsions,” *Adv. Mater.*, vol. 19, no. 19, pp. 2973–2978, Oct. 2007.

[91] S. Tsuji and H. Kawaguchi, “Thermosensitive pickering emulsion stabilized by poly(N-isopropylacrylamide)-carrying particles.,” *Langmuir*, vol. 24, no. 7, pp. 3300–5, Apr. 2008.

[92] C. Monteux, C. Marlière, P. Paris, N. Pantoustier, N. Sanson, and P. Perrin, “Poly(N-isopropylacrylamide) microgels at the oil-water interface: interfacial properties as a function of temperature.,” *Langmuir*, vol. 26, no. 17, pp. 13839–46, Oct. 2010.

[93] M. Destribats, V. Lapeyre, E. Sellier, F. Leal-Calderon, V. Ravaine, and V. Schmitt, “Origin and control of adhesion between emulsion drops stabilized by thermally sensitive soft colloidal particles.,” *Langmuir*, vol. 28, no. 8, pp. 3744–55, Feb. 2012.

[94] S. Fujii, E. S. Read, B. P. Binks, and S. P. Armes, “Stimulus-Responsive Emulsifiers Based on Nanocomposite Microgel Particles,” *Adv. Mater.*, vol. 17, no. 8, pp. 1014–1018, Apr. 2005.

[95] F. Gautier, M. Destribats, R. Perrier-Cornet, J.-F. Dechézelles, J. Giermanska, V. Héroguez, S. Ravaine, F. Leal-Calderon, and V. Schmitt, “Stepwise interfacial self-assembly of nanoparticles via specific DNA pairing.,” *Pick. Emuls. with stimulable Part. from highly- to weakly-covered interfaces*, vol. 9, pp. 6455–62, Dec. 2007.

[96] S. Abend and G. Lagaly, “Bentonite and double hydroxides as emulsifying agents,” *Clay Miner.*, vol. 36, no. 4, pp. 557–570, Dec. 2001.

[97] S. Abend, N. Bonnke, U. Gutschner, and G. Lagaly, “Stabilization of emulsions by heterocoagulation of clay minerals and layered double hydroxides,” *Colloid Polym. Sci.*, vol. 276, no. 8, pp. 730–737, Sep. 1998.

[98] B. P. Binks and S. O. Lumsdon, “Catastrophic Phase Inversion of Water-in-Oil Emulsions Stabilized by Hydrophobic Silica,” *Langmuir*, vol. 16, no. 6, pp. 2539–2547, Mar. 2000.

[99] S. Abend, “Aggregation in Pickering emulsions,” vol. 260, no. 40, pp. 257–260, 1999.

[100] U. Neuhäusler, S. Abend, C. Jacobsen, and G. Lagaly, “Soft X-ray spectromicroscopy on solid-stabilized emulsions,” *Colloid Polym. Sci.*, vol. 277, no. 8, pp. 719–726, Aug. 1999.

[101] S. Arditty, C. P. Whitby, B. P. Binks, V. Schmitt, and F. Leal-Calderon, “Some general features of limited coalescence in solid-stabilized emulsions,” *Eur. Phys. J. E*, vol. 11, no. 3, pp. 273–281, 2003.

[102] X. Zhai, S. Efrima, B. Gurion, V. Uni, P. O. Box, and V. Beer-she, “Chemical and Physical Aspects of Macroemulsions Stabilized by Interfacial Colloids,” vol. 3654, no. 95, pp. 11019–11028, 1996.

[103] R. M. Wiley, “Limited coalescence of oil droplets in coarse oil-in-water emulsions,” *J. Colloid Sci.*, vol. 9, no. 5, pp. 427–437, Oct. 1954.

[104] J. A. Juárez and C. P. Whitby, “Oil-in-water Pickering emulsion destabilisation at low particle concentrations.,” *J. Colloid Interface Sci.*, vol. 368, no. 1, pp. 319–25, Feb. 2012.

[105] J. Frelichowska, M.-A. Bolzinger, and Y. Chevalier, “Effects of solid particle content on properties of o/w Pickering emulsions.,” *J. Colloid Interface Sci.*, vol. 351, no. 2, pp. 348–56, Nov. 2010.

[106] H. Barthel, “Surface interactions of dimethylsiloxy group-modified fumed silica,” *Colloids Surfaces A Physicochem. Eng. Asp.*, vol. 101, no. 2–3, pp. 217–226, Aug. 1995.

[107] M. N. Lee, H. K. Chan, and A. Mohraz, “Characteristics of pickering emulsion gels formed by droplet bridging.,” *Langmuir*, vol. 28, no. 6, pp. 3085–91, Feb. 2012.

[108] T. S. Horozov, B. P. Binks, and T. Gottschalk-Gaudig, “Effect of electrolyte in silicone oil-in-water emulsions stabilised by fumed silica particles,” *Phys. Chem. Chem. Phys.*, vol. 9, pp. 6398–6404, Dec. 2007.

[109] C. P. Whitby, F. E. Fischer, D. Fornasiero, and J. Ralston, “Shear-induced coalescence of oil-in-water Pickering emulsions.,” *J. Colloid Interface Sci.*, vol. 361, no. 1, pp. 170–7, Sep. 2011.

[110] R. G. Larson, *The structure and rheology of complex fluids*, vol. 4. Oxfort University Press, 1999.

[111] C. J. Brinker and G. W. Scherer, *Sol-Gel Science - The Physics and Chemistry of Sol-Gel Processing*. London: ACADEMIC PRESS, INC., 1990, p. 462.

[112] R. Buscall, P. D. A. Mills, and G. E. Yates, “Viscoelastic properties of strongly flocculated polystyrene latex dispersions,” *Colloids and Surfaces*, vol. 18, no. 2–4, pp. 341–358, Jun. 1986.

[113] R. Buscall and J. I. Mcgowan, “The rheology of concentrated dispersions of weakly attracting colloidal particles with and without wall slip,” vol. 37, no. August, 1993.

[114] C. J. Rueb and C. F. Zukoski, “Viscoelastic properties of colloidal gels,” *J. Rheol.*, vol. 41, no. 2, 1997.

[115] N. Q. Dzuy and D. V Boger, “Direct Yield Stress Measurement with the Vane Method,” *J. Rheol.*, vol. 29, no. 3, 1985.

[116] Y. K. Leong, P. J. Scales, T. W. Healy, D. V Boger, and R. Buscall, “Rheological Evidence of Adsorbate-mediated Short-range Steric Forces in Concentrated Dispersions,” vol. 89, no. 14, pp. 2473–2478, 1993.

[117] P. G. de Gennes, P. Pincus, and R. M. Velasco, “REMARKS ON POLYELECTROLYTE CONFORMATION,” *Le J. Phys.*, vol. 37, pp. 1461–1473, 1976.

[118] S. Feng and P. N. Sen, “Percolation on Elastic Networks: New Exponent and Threshold,” *Phys. Rev. Lett.*, vol. 52, no. 3, pp. 216–219, 1984.

[119] D. Stauffer and A. Aharony, *Introduction to Percolation Theory*. Taylor & Francis, 1992.

[120] R. Buscall, P. D. A. Mills, R. F. Stewart, D. Sutton, L. R. White, and G. E. Yates, "The rheology of strongly-flocculated suspensions," *J. Nonnewton. Fluid Mech.*, vol. 24, no. 2, pp. 183–202, Jan. 1987.

[121] R. Buscall, P. D. A. Mills, T. Heath, and C. Wa, "Scaling Behaviour of the Rheology of Aggregate Networks formed from Colloidal Particles," vol. 84, no. 12, 1988.

[122] W. Shih, Y. Shih, S. Kim, J. Liu, and I. A. Aksay, "= 1.95," vol. 42, no. 8, 1990.

[123] a. a. Potanin, R. De Rooij, D. Van den Ende, and J. Mellema, "Microrheological modeling of weakly aggregated dispersions," *J. Chem. Phys.*, vol. 102, no. 14, p. 5845, 1995.

[124] B. V Velamakanni, J. C. Chang, F. F. Lange, and D. S. Pearson, "New Method for Efficient Colloidal Particle Packing via Modulation," no. 6, pp. 1323–1325, 1990.

[125] W. B. Russel, D. A. Saville, and W. R. Schowalter, *Colloidal Dispersions*. Cambridge University Press, 1989.

[126] R. B. Larson, "No Title," vol. 102, no. July, pp. 709–722, 1990.

[127] J. W. Goodwin, R. W. Hughes, S. J. Partridge, and C. F. Zukoski, "The elasticity of weakly flocculated suspensions," *J. Chem. Phys.*, vol. 85, no. 1, p. 559, 1986.

[128] P. J. Flory, *Principles of Polymer Chemistry*. Cornell University Press, 1953.

[129] P. J. Flory, *Statistical mechanics of chain molecules*. Interscience Publishers, 1969.

[130] F. Tanaka and F. Tanaka, *Classical theory of gelation*. publisherNameCambridge University Press, 2011.

[131] A. A. Griffith, "The Phenomena of Rupture and Flow in Solids," *Philos. Trans. R. Soc. London*, vol. 221, pp. 163–198, 1920.

[132] G. P. Cherepanov, "Mechanics of brittle fracture," 1979.

[133] J. Zarzycki, M. Prassas, and J. Phalippou, “Synthesis of glasses from gels: the problem of monolithic gels,” *J. Mater. Sci.*, vol. 17, no. 11, pp. 3371–3379, Nov. 1982.

[134] L. L. Hench, *Science of ceramic chemical processing. Herausgegeben von L. L. Hench und D. R. Ulrich. John Wiley, New York 1986. 594 S., geb. 90.30. — ISBN 0-471-82645-6.*, vol. 99, no. 9. New York: WILEY-VCH Verlag GmbH, 1987, pp. 52–64.

[135] Z. P. Guo, D. Z. Jia, L. Yuan, and H. K. Liu, “Optimizing synthesis of silicon/disordered carbon composites for use as anode materials in lithium-ion batteries,” *J. Power Sources*, vol. 159, no. 1, pp. 332–335, Sep. 2006.

[136] H. Feng, J. Sprakel, D. Ershov, T. Krebs, M. a. Cohen Stuart, and J. van der Gucht, “Two modes of phase inversion in a drying emulsion,” *Soft Matter*, vol. 9, no. 10, p. 2810, 2013.

[137] M. D. Abràmoff, I. Hospitals, P. J. Magalhães, and M. Abràmoff, “Image Processing with ImageJ.”

[138] A. P. Sullivan and P. K. Kilpatrick, “The Effects of Inorganic Solid Particles on Water and Crude Oil Emulsion Stability,” *Ind. Eng. Chem. Res.*, vol. 41, no. 14, pp. 3389–3404, Jul. 2002.

[139] B. Dai, L. Fu, L. Liao, N. Liu, K. Yan, Y. Chen, and Z. Liu, “High-quality single-layer graphene via reparative reduction of graphene oxide,” *Nano Res.*, vol. 4, no. 5, pp. 434–439, Feb. 2011.

[140] S. Pei and H.-M. Cheng, “The reduction of graphene oxide,” *Carbon N. Y.*, vol. 50, no. 9, pp. 3210–3228, Aug. 2012.

[141] Y.-M. Kang, J.-Y. Go, S.-M. Lee, and W.-U. Choi, “Impedance study on the correlation between phase transition and electrochemical degradation of Si-based materials,” *Electrochem. commun.*, vol. 9, no. 6, pp. 1276–1281, Jun. 2007.

[142] I. Kim, P. N. Kumta, and G. E. Blomgren, “Si / TiN Nanocomposites Novel Anode Materials for Li-Ion Batteries,” vol. 3, no. 11, pp. 493–496, 2000.

[143] I.-S. Kim and P. N. Kumta, “High capacity Si/C nanocomposite anodes for Li-ion batteries,” *J. Power Sources*, vol. 136, no. 1, pp. 145–149, Sep. 2004.

[144] W.-R. Liu, M.-H. Yang, H.-C. Wu, S. M. Chiao, and N.-L. Wu, “Enhanced Cycle Life of Si Anode for Li-Ion Batteries by Using Modified Elastomeric Binder,” *Electrochem. Solid-State Lett.*, vol. 8, no. 2, p. A100, 2005.

[145] D. Mazouzi, B. Lestriez, L. Roué, and D. Guyomard, “Silicon Composite Electrode with High Capacity and Long Cycle Life,” *Electrochem. Solid-State Lett.*, vol. 12, no. 11, p. A215, 2009.

[146] P. Xueman, X. Mingxia, L. Hui, L. Xiaolei, and J. Huiming, “Rheological properties and thixotropy model of concentrated aqueous silicon slurry for gel casting,” *Colloids Surfaces A Physicochem. Eng. Asp.*, vol. 317, no. 1–3, pp. 136–145, Mar. 2008.

[147] L. T. Cuba-Chiem, L. Huynh, J. Ralston, and D. a Beattie, “In situ particle film ATR FTIR spectroscopy of carboxymethyl cellulose adsorption on talc: binding mechanism, pH effects, and adsorption kinetics.,” *Langmuir*, vol. 24, no. 15, pp. 8036–44, Aug. 2008.

[148] Y. Chen, M. Nie, B. L. Lucht, A. Saha, and R. Pradeep, “High capacity and stable silicon / carbon anodes for lithium-ion batteries prepared using emulsion-templated directed assembly.”

[149] W. Zhou, R. P. Apkarian, and Z. L. Wang, “Fundamentals of Scanning Electron Microscopy.”

[150] J. C. Burns, L. J. Krause, D.-B. Le, L. D. Jensen, a. J. Smith, D. Xiong, and J. R. Dahn, “Introducing Symmetric Li-Ion Cells as a Tool to Study Cell Degradation Mechanisms,” *J. Electrochem. Soc.*, vol. 158, no. 12, p. A1417, 2011.

[151] T. Instruments, “Understanding Rheology of Structured Fluids,” pp. 1–11.

[152] W. Xing and J. R. Dahn, “Study of Irreversible Capacities for Li Insertion in Hard and Graphitic Carbons,” vol. 144, no. 4, pp. 1195–1201, 1997.

[153] S. R. Mukai, T. Hasegawa, M. Takagi, and H. Tamon, “Reduction of irreversible capacities of amorphous carbon materials for lithium ion battery anodes by Li2CO3 addition,” *Carbon N. Y.*, vol. 42, no. 4, pp. 837–842, 2004.